A Study of C_{60} via Scanning Probe Microscopy, Hückel and Monte Carlo Methods

Jeremy M. Leaf

School of Physics and Astronomy, University of Nottingham,

Nottingham NG7 2RD, U.K.

August 18, 2017

Abstract

The C_{60} molecule, in a number of different environments and configurations, was studied via a range of theoretical and experimental techniques. Experimentally, scanning tunnelling microscopy (STM) and atomic force microscopy (AFM) techniques were employed to firstly study orientational ordering in C_{60} monolayers and multilayers, and subsequently, potassium doping of isolated C_{60} molecules, and C_{60} monolayers. A single C_{60} molecule was manipulated over successive K atoms, such that it is progressively doped, it was then studied via STM and AFM, where molecular charging was seen to influence both electronic structure and force characteristics.

Two Monte Carlo simulations were written to investigate different aspects of C_{60} molecular kinetics on surfaces. The first is a novel simulation into the orientational ordering of C_{60} monolayers and multilayers, with the inclusion of a surface interaction. By pre-calculating a repulsive pairwise intermolecular interaction, using Hückel theory, hundreds of molecules in a molecular assembly could be efficiently simulated. Numerous complex monolayer and multilayer long-range rotational configurations, as observed via STM from literature and our own experiments, were successfully modelled.

A second Monte Carlo simulation was written to study the kinetics of a diffusing C_{60} on a hydrogen passivated silicon surface. This to estimate the feasibility of a future SPM recreation of the famous Maxwell's Demon thought experiment. A Girifalco potential was applied from a number of static molecules to a sinusoidal surface potential. A Monte Carlo simulation was applied to this surface potential to fully explore the dynamics of the system. As a result, a number of optimal chamber configurations were suggested from outcomes observed in simulation.

Acknowledgements

The work presented in this thesis has been a long journey, and a labour of love. I'd like to thank all the people who made it possible. First and foremost my supervisors Philip Moriarty and Janette Dunn, whose input and guidance has been invaluable. A special mention goes to Samuel Jarvis, for the many hours in the lab he gave. Also, my gratitude goes to other members of the group for the many helpful discussions - Adam Sweetman, Philipp Rahe, and Alex Seywell.

On a personal note, I would like to thank my parents for their support over the years, but most of all, my wife Zanel. For her love and encouragement, for tolerating the late nights in the lab, and weekend trips to nurse the Createc with liquid nitrogen.

Though I walk through the valley of the shadow of the Createc,

I will fear no noise

For thou art with me, thy rod and thy staff they comfort me.

Contents

Chapter 1

Introduction

Over the past 30 years, a range of science fiction authors, Hollywood, and some over-enthusiastic scientists, have engaged the public on the subject area of nanotechnology and nanoscience. As a result, these fields have been vastly misrepresented in terms of both purpose and capabilities. An army of self-replicating 'nano-bots', consuming the world and its resources, is a spectacle that makes a good story, not good science. That said, the field of nanoscience should not also be undersold. Achievements on studying and manipulating materials on the nanoscale show a remarkable journey towards utilising nanoscopic effects to enhance humanity's technological capabilities. Be it by enhancing a surface's properties, constructing a nanoscopic transistor, or controlling liquid phase chemistry for new medical treatments, such as drug delivery. A number of nanoscience milestones and concepts are shown in Figure 1.1. Nanoscience and nanotechnology are a 21st century approach to pushing the boundaries met in the 20th.

The observation, manipulation, and study of individual atoms and molecules would seem a far-fetched ambition. An ever improving set of precision instruments have made that impossible dream a reality.

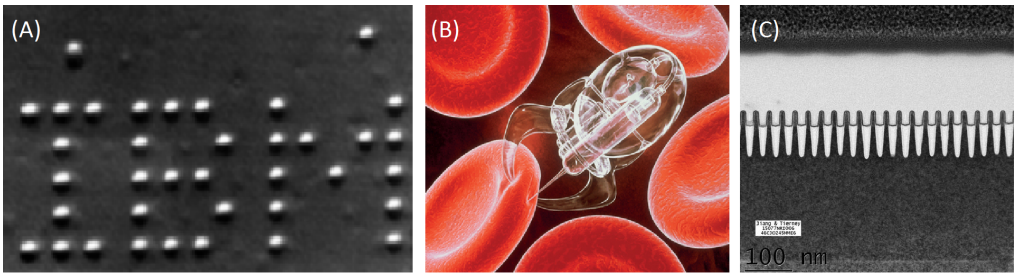

Figure 1.1: (A) 35 xenon atoms on a nickel surface, arranged to spell IBM using an STM instrument. (B) A science-fiction view of the future capabilities of nanotechnology (C) Transmission electron microscope (TEM) image of IBM's 7-nanometer finned field effect transistors.

The field of nanoscience is characterised by the study and manipulation of atoms, molecules, and surfaces on the nanoscale. This length-scale is characterised by dimensions and sizes from the Ångstrom to the 10s of

nanometres range. Atoms and molecules occupy the smaller end of that scale, and so imaging them directly, and manipulating them is a challenging prospect. An answer to this problem was the development of two important instruments — the scanning tunnelling microscope (STM)[1], and later the atomic force microscope (AFM). The AFM and STM have similar modes of operation, and are members of the scanning probe microscopy (SPM) family of instruments. These allow the user to not only observe surfaces and objects at the nanoscale, but also manipulate them directly. The AFM and STM have made available many previously impossible options for the study of materials, and this has led to many high profile achievements and publications.[2][3][4][5] Along with the potential technological benefits of nanotechnology, there is considerable excitement in nanoscience due to its simple goal to understand the mechanisms and characteristics behind some of the lowest level building blocks in nature.

'What I cannot create, I do not understand.'
- Richard Feynman's Blackboard

A vital step in the journey to fully understand the various processes and interactions that occur between atoms and molecules, is that of simulation. By creating a computational model of a physical system, and comparing the output of that model to reality, it is possible to test our understanding of that system. Well-established models may be used as predictive agents to both guide the direction, and explore the outcome of future experiments. Finally, computational models may use observed system configurations as starting points to then further investigate the detail of these systems.
Various different computational methods have been applied to nanoscale systems. These include density functional theory (DFT)[6], Monte Carlo methods[7], molecular dynamics simulations[8], Hückel theory[9], and others. These techniques rely on some fundamental understanding of the electronic and bonding structure of the species being studied, and the energetic

interactions between them.

As species on the nanoscale interact with one another, complex order will often be the result. Subtle forces and interactions between different atomic and molecular geometries will often lead to remarkably complex and interesting reconstructions and orderings. The focus of this body of work is the employment of a full range of theoretical and experimental techniques to explore and manipulate these subtle interactions on the nanoscale.

1.0.1 The C_{60} Molecule

A focal point of this work is the C_{60} molecule. Of all molecules, C_{60} carries a unique place in physics and chemistry. This is partly due to its striking shape and symmetry as seen in Fig. 1.2. The C_{60} molecule is the most spherical-like molecule ever observed and has many degrees of symmetry, it is made up of sixty carbon atoms bonded in alternating double and single bonds. It has a truncated icosahedron geometric shape and thus its surface is comprised of twelve pentagons and twenty hexagons. Since its first synthesis in 1985[10] and associated Nobel Prize in Chemistry, it has since been the subject of significant investigation and interest. Electronically, it exhibits intrinsic semiconducting properties.

Important aspects of the study of C_{60} of particular relevance to this thesis include how they interact with each other on a surface, how they respond to the external stimuli of an SPM instrument, and how their electronic structure can be controlled. Sub-monolayer and larger coverages of C_{60} can produce fascinating patterns as a result of interactions with the surface and neighbouring fullerene molecules. Fullerenes can also be picked up [11], charged [12], rotated and moved around [13] using an SPM tip.

Numerous aspects of the C_{60} molecule will be explored throughout this thesis, using a variety of experimental and theoretical techniques.

In the second chapter of this thesis, the experimental background of

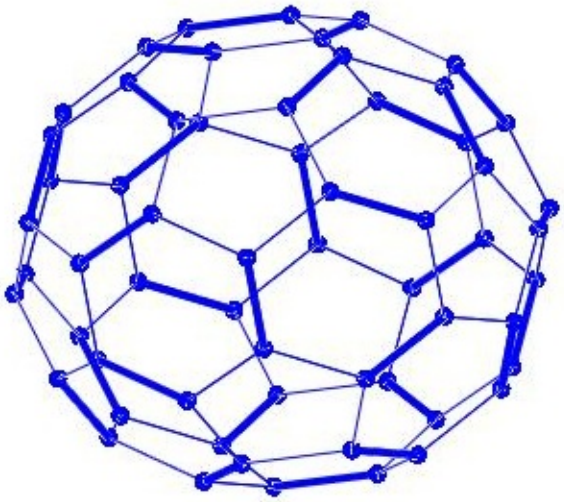

Figure 1.2: The C_{60} molecule. Thick and thin lines represent double and single bonds respectively.

the work carried out in this thesis will be examined, primarily looking at the operation of STM and AFM. The third chapter will focus on the background and theory of the theoretical methods employed within this thesis. These are Hückel Theory, Extended Hückel theory, and Monte Carlo techniques. The fourth chapter will discuss the background and subsequent development of a Monte Carlo simulation to study C_{60} rotational order in C_{60} assemblies. Here, repulsive intermolecular interactions are modelled via Hückel theory. Following this, the fifth chapter will go into detail about this simulations results with relation to STM data. The sixth chapter will discuss an AFM and STM study of K doped C_{60}, where our interest is in observing force characteristics and changes in electronic structure of doped C_{60}. Both isolated molecules and monolayers are doped and examined. Finally, the seventh chapter will discuss a Monte Carlo study of C_{60} molecular dynamics within the confines of an enclosed 2D chamber, and a tip influence. This to examine the kinetics of a possible future experiment aiming to reproduce the famous 'Maxwell's Demon' thought experiment, as mediated via an STM tip.

Chapter 2

Experimental Background

2.0.1 Chapter Overview

This chapter introduces the tools and techniques used in the experimental portion of this body of work. It discusses the different forms of scanning probe microscope and their theory of operation, the environment that they operate in, and the processes for preparing samples to be imaged.

2.1 The Scanning Probe Microscope

2.1.1 Achieving Atomic Resolution

The study of surface features on the atomic scale required the development of a new class of instrument, the scanning probe microscope (SPM). These operate by having a sharp probe (or needle) raster over a surface. Interactions between the tip of the probe and the surface can be measured. The strength of these interactions is typically a function of the tip-surface separation. As the tip is rastered, changes measured in the tip-surface interaction correspond to changes in the surface topography or electronic properties. The type of interaction that is measured depends on the specific type of SPM being used. STMs measure a current, while AFMs directly measure forces. Four aspects primarily determine the resolution of the instrument. These are the resolution at which the tip can be precisely scanned, the sharpness of the tip, and the magnitude of electrical and mechanical noise. Under optimal conditions, SPM instruments can achieve spatial measurements with better than Ångstrom precision.

The fine motion of the tip is achieved by attaching it to a set of piezoelectric transducers controlling its XYZ position. Piezoelectric materials distort when an electric field is applied across them. A tip attached to one of these transducers can be moved on nanoscopic length scales by applying tiny fields across the transducer. Typically, multiple piezoelectric trans-

ducers are used for full control in 3D. A coarse and fine resolution set of piezos are employed to enhance the range over which the microscope can scan, and assist in approaching the tip towards the surface. The coarse transducer is designed to position the tip in the general correct location over the sample in XYZ, enabling the operator to avoid any damaged areas of the surface visually. The tip can then be advanced towards the surface so that the surface-tip separation is within the movement range of the fine piezos. The fine piezoelectric transducers advance the tip the final distance until an interaction is measured with the surface. XY rastering can then be performed to image the surface.

Due to the extreme short-range nature of the interactions measured via SPM, an atomically sharp, or highly conical, tip is not always necessary. Even a relatively 'blunt' tip can resolve features with atomic resolution. Just a single atom protruding from the end of the tip will dominate any interactions more than its higher neighbours. A blunt tip, however, will also have a large tip radius of curvature and convolve the images produced with long-range interactions. Therefore, even though respectable images can be produced with blunt tips, sharp tips are almost always preferable. The tip can be made microscopically sharp by using chemical etching or other methods on an already sharp probe. These techniques can produce SPM tips with very small radii of curvature.

Electrical noise can be limited with low noise electronics, excellent grounding, and shielded cables. Particular care must be taken when amplifying the tiny signals from the SPM to not introduce noise. Low noise signal preamplifiers are often placed in close proximity to the tip to reduce radiated interference. Mechanical vibrations are eliminated via a number of combined vibration isolation apparatus, each calibrated to eliminate different frequencies of mechanical noise. Vibrations as small as 0.1Åamplitude must

be isolated to produce images with suitable resolution. Air legs can be used for the entire microscope apparatus to isolate high magnitude and low frequency vibrations. Another platform holding the actual SPM instrument can then be suspended by low tension springs on the air-legs apparatus to isolate any higher frequency vibrations. A vibration-free environment is also important. Often, SPM instruments are located in basements and ground floors to minimise the influence of structural vibrations from the building.

Thermal drift, due to slow temperature shifts, can make accurate imaging problematic. To mitigate this, the sample and SPM instrument can be cooled to liquid nitrogen or helium temperatures to stabilise the temperature. Room temperature SPM instruments are common but suffer from excess drift, which is particularly noticeable when scanning small areas. Atom tracking technology can also mitigate this, by estimating the drift and compensating for it.

2.1.2 SPM Sample Environment

For the best images to be acquired, the imaged surface must be free of contaminants - undesired atoms/molecules. Keeping the sample clean can be achieved by placing the SPM instrument inside a vacuum chamber. An ultra-high vacuum (UHV) environment will ensure that no atmospheric contaminants are present to affect the surface. The UHV environment will also remove any interactions induced by an atmosphere in the tip-surface interactions. A differential pumping apparatus is employed to initially achieve the vacuum environment, with a scroll pump backing a turbo pump to initially achieve a rough vacuum. An ion-pumping, or cryo-pumping apparatus, is then employed to enhance the vacuum further. Ion pumping

works by applying a strong electric field across two plates. Atoms between these plates are ionised and so attracted to the pump's cathode. The cathode typically has a large surface area, and is constructed from highly reactive materials, such as titanium. Cryo-pumping involves cooling a surface within the vacuum chamber to cryogenic temperatures. Any atoms in the vacuum will condense onto the surface.

2.1.3 SPM Sample Preparation Procedures

Samples are prepared for imaging via a multi-step process that is carried out under UHV conditions. This process involves the initial cleaning and conditioning of the substrate, then depositing any atoms or molecules of interest onto the sample, normally via thermal evaporation. The substrate is initially cleaned via sputtering. This is where high-energy neon or argon ions are accelerated towards the substrate via a high electric field. These ions ballistically etch the surface to remove any contaminants; they also damage the surface itself. Once cleaned, the damaged and cratered surface must be conditioned. This is done by annealing the substrate. Annealing gives surface atoms sufficient energy to diffuse across the substrate, and reform a pristine surface. Large, crystalline, atomically flat regions are necessary for scanning the substrate. This also provides an area for deposited species to reconstruct and self organise.

Atoms and molecules are then deposited onto the substrate via a series of different apparatus. NaCl for example can be deposited by electrically heating a crucible filled with macroscopic levels of the material. The quantity of the material deposited onto the substrate can be controlled by adjusting the time of deposition, the temperature of the crucible, and finally the temperature of the substrate. A cold substrate will have a higher sticking coefficient than a warm one. Finally, the sample can then be further an-

nealed to give the deposited species energy to reconstruct or undergo some desired chemical process.

2.1.4 Control Loop Feedback Systems in SPM

Control loop feedback systems are widely used in practically all branches of industry and science. Their purpose it to take an input measurement from the system being controlled, then as a result of that input, apply some control output. The controller will do this continuously to quickly bring the system to a desired state.

PID Controllers

A proportional-integral-derivative (PID) controller is a commonly used control loop feedback system. The control output from the controller is dependent on the difference between the measured input of the current system state, and a desired state, or set point. This difference is know as the system error. The PID controller has three elements that work in conjunction to bring the system to its desired state: proportional, integral, and derivative.

1. A proportional element acts directly on the difference between the state and setpoint. This is the current system error.

2. An integral element acts on the time integral of the difference between the state and setpoint. This is the history of the system error.

3. A derivative element acts on the time derivative of the difference between the state and setpoint. This is the rate of change of the system error.

The output of each element is weighted by a gain and summed, before

being outputted to drive the controlled system. As follows:

$$u(t) = K_p e(t) + K_i \int_0^t e(t)dt + K_d \frac{de(t)}{dt} \tag{2.1}$$

Where $u(t)$ is the time dependent controller output, $e(t)$ is the system error, and K_p, K_i, K_d are the proportional, integral and derivative gains. By carefully adjusting the gains of each element, the controller will be able to drive the system in a stable, damped configuration, with the ability to respond quickly to fast changes in the set point or measured system state. Mis-calibrated gains will lead to system instability or other undesirable behaviour.

1. A high P gain will lead to a fast reduction in the error term; however can induce high frequency oscillations as the controller overshoots its target.

2. While I gain removes any steady state errors, it reduces the settling time of the system and can lead to lower frequency oscillations.

3. The D term will reduce overshoot and improve damping; however, it is extremely vulnerable to system noise.

SPMs typically only use the proportional and integral controller elements, due to noise in their signal channels.

2.2 The Scanning Tunnelling Microscope

The scanning tunnelling microscope, developed in 1981 by Gerd Binnig and Heinrich Rohrer[1] at IBM, was the first SPM instrument to be developed. Its inventors were awarded the Nobel prize in Physics just five years later in 1986. The STM is capable of probing the spatial and electronic structure of a surface at the atomic level, and performing direct manipulation of

species on the substrate. It represented a step change in site-specific surface science.

This instrument operates on the principle of quantum mechanical tunneling of electrons, between the tip and surface, due to an applied bias. To operate, the tip-surface separation is reduced to the 1nm range, maintaining an insulating barrier between them. A small voltage (normally between 1mV and 2V) is applied between a conducting surface and tip. Due to the small tip-surface separation, quantum mechanical tunnelling of electrons will occur [14] across the gap. Electrons tunnel from the surface through the potential barrier into the tip, or vice versa depending on the sign of the potential. This leads to a measurable tunnelling current between the surface and tip that is highly dependent on the tip-surface separation and applied bias.

2.2.1 The Tunnelling Current

The measured tunnel current is a critical part of the STMs operation. The tunnelling current can be estimated by considering the solution to the Schrodinger's equation, for an electron tunnelling through a barrier:

$$I_t(z) = I_0 e^{-2\kappa_t z} \tag{2.2}$$

where I_t is the tunnel current, I_0 is a prefactor relating to the tip and sample density of states and the applied voltage, z is the tip-sample separation and

$$\kappa_t = \sqrt{2m\Phi}/\hbar \tag{2.3}$$

where m is the mass of an electron and Φ is the work function of the tunnelling barrier. From this it is clear that the tunnel current is exponentially dependent to the surface-sample separation, and the ease by which elec-

trons can tunnel across that barrier.

Another widely used model is the Tersoff-Hamann model [15], which is based on Bardeen's theory[14]. The tip and sample can be seen as independent systems with a weak coupling. The tunnel current is then said to be proportional to the convolution of their electronic states. In other words, the tunnel current is proportional to the local density of states (LDOS) of the sample at the centre of the tip's radii of curvature [16]. With the tip approximated as an s-wave, the tunnel current can be equated to

$$I \propto \sum_{s} |\Psi_s(r_t)|^2 \delta(E_s - E_f) = D \tag{2.4}$$

where $\Psi_s(r_t)$ is the wavefunction of the sample at the tip for the state s, E_f is the Fermi level, D is the LDOS, and E_s is the energy eigenvalue of the sample at state s.

This shows that the tunnel current is a function of the available states for tunnelling. Empty states can be probed by tunnelling into the surface, whereas with a reverse bias full states of the surface can be probed by tunnelling into the tip. By scanning at different bias voltages and polarities, it is possible to thoroughly examine the surface's electronic structure.

Many surfaces and adsorbed species exhibit complex electronic structure and effects. This means that interpreting the magnitude of a tunnel current, at a given bias and tunnel gap, is not a simple task.

2.2.2 STM Operation

To generate an image of the surface, the tip is rastered across the surface while keeping the tip bias constant. The STM has two typical modes of operation for taking images, constant current or constant height mode. Constant height mode keeps the tip height constant and so allows the tunnel

current to vary. The tunnelling current is measured as the tip is rastered. Constant height mode does not work well with large topographic changes on the surface, or thermo-mechanical instabilities, as these can cause the tip to crash into the surface. Additionally, if the surface drops significantly away from the tip, a loss in tunnel current and, so, resolution will occur.

Constant current mode (Fig. 2.1) mitigates these problems with the added complexity of a PI or PID feedback loop. This control loop considers the tunnelling current as a process variable, and outputs to the Z piezo controller according to a desired current set point. This leads to the sample-tip separation being kept constant. The tip height is tracked as the tip is rastered to generate an image of the surface. While safer, this mode can be problematic if the feedback loop is not properly tuned and can lead to instability or introduce image artefacts [17].

2.2.3 Interpreting STM images

On larger scales, the electronic states of the surface often roughly correspond to the general topography of the surface, as such, images produced via STM can be generally interpreted as corresponding to the height topography of the surface. When considering defects, molecules, and other oddities, careful consideration of the expected LDOS must be made to properly interpret images. An apparent depression in a surface may actually be a protrusion with a reduced LDOS and so conductivity. An example of the effects of a complex LDOS on resultant STM images is shown in Figure 3.2. When scanning molecules and other complex structures, further information about molecular orbitals etc. can be captured by carefully adjusting the scanning bias, tip height and current.

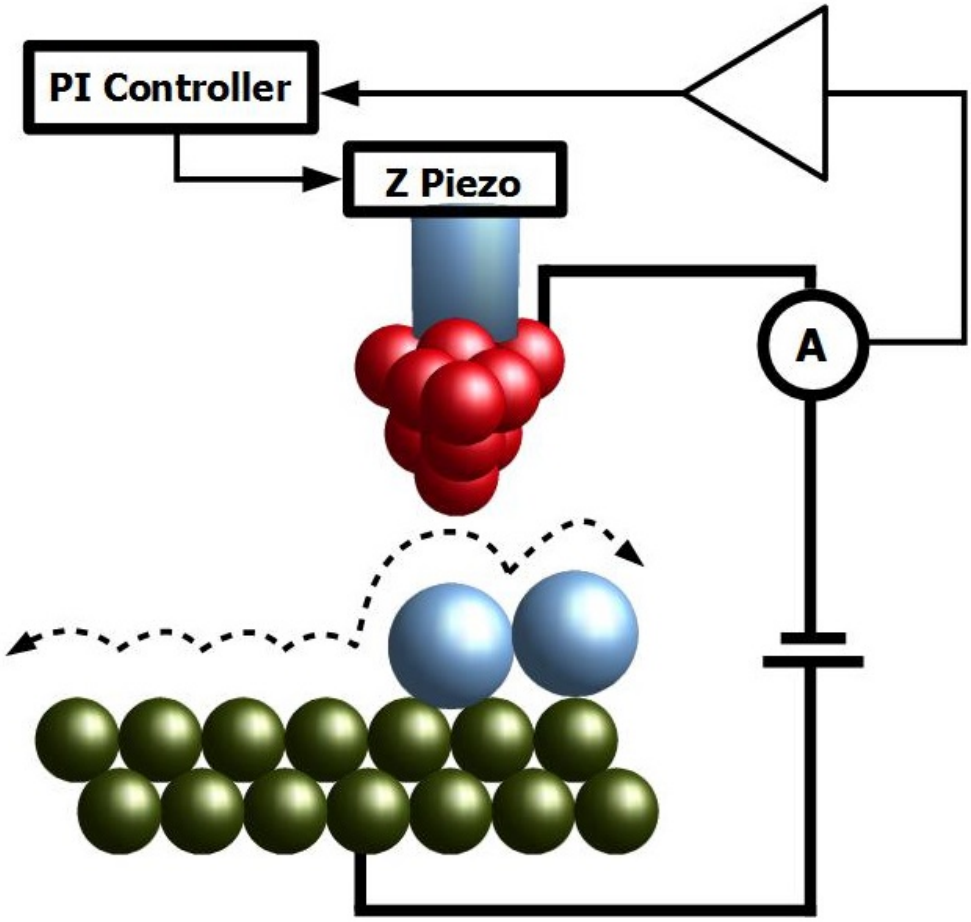

Figure 2.1: A diagram of STM operation in current feedback mode. A bias is applied between a tip and sample, and a tunnel current is measured. The tunnelling current is amplified and fed to a PI controller. This responds to the current and adjusts the Z piezo to maintain a constant measured current as the tip rasters over the surface.

2.2.4 Differential Conductance Measurements

An important aspect of STM operation is the practice of taking differential conductance measurements. This is where the tip height is fixed, and the bias is swept through a range of voltages. The output current is measured, and then differentiated with respect to voltage. The result of this differentiation is a map of the surface electronic states. An intuitive I/V curve for a metal would be a linear function, whose gradient solely depended on the conductivity of the sample. The differential of this would be a flat line. Though this is in fact an insufficient explanation in the context of STM, due to energy-dependent conductance effects through tip-sample

tunnelling. Once materials with distinct energy bands are observed, this becomes more complicated. As the bias increases through regions where there are no electronic states, no increase in tunnelling current is measured. As the bias reaches a level where a new, as yet unreached, state becomes available for tunnelling, a rise in the tunnelling current is observed. As the bias increases beyond this state into a level with no available states, the tunnelling current again ceases to rise. By differentiating this I/V curve, a map of the LDOS is returned.

2.3 The AFM

The atomic force microscope was developed after the STM and operates by indirectly measuring van der Waals forces, Pauli repulsion forces, and electrostatic forces between the tip and sample [18]. This by observing the response of the tip to applied forces. As a result, structural properties of the material being imaged can be inferred.

2.3.1 Forces in AFM

The van der Waals force is an electrostatic force that originates from instantaneous dipoles (charge fluctuations) in two nearby objects/atoms inducing a short-range columbic attraction. It is ubiquitous in nature and is fundamental to many physical, chemical, and biological processes. Pauli exclusion forces decay even more rapidly, making them very short-ranged. Pauli forces become relevant when two atoms are brought into close proximity such that their respective electron orbitals start to overlap. This leads to a strong but very short-ranged repulsive force. Electrostatic forces from interactions between like, or opposite, charges lead to long-range force interactions. A combination of these long and short-ranged forces leads to

a Lennard-Jones type potential between the tip and sample, as shown in Fig. 2.2. As the tip approaches the surface, the attractive van der Waals forces initially dominate, until the tip-sample separation is small enough for repulsive Pauli forces to dominate.

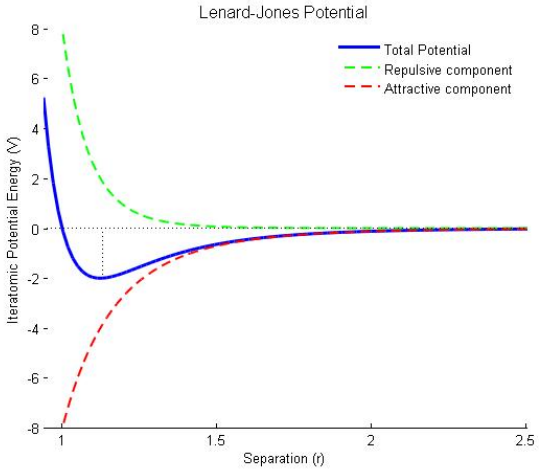

Figure 2.2: The Lennard-Jones Potential shows attractive and repulsive regime. To the left of the potential minimum is the repulsive regime, to the right the attractive

2.3.2 AFM - Modes of Operation

Pauli and van der Waals forces act between the tip and surface; however they are extremely small and thus very hard to measure. This problem can be overcome by constructing a silicon cantilever with a machined tip on the end of it. If the properties of the cantilever are well known and its deflection can be measured accurately, it is possible to measure the forces applied to the tip by the surface. Unfortunately, for the tip to be deflected, a relatively large force must be applied to it. This essentially necessitates the tip to be pressed into contact with the surface as it is rastered across it. This is known as contact-AFM, a drawback to this approach is that it will lead to uncontrolled damage to the surface being imaged. For imaging soft or lightly adsorbed molecules, a different technique is required.

A more refined method known as non-contact AFM (NC-AFM) keeps the tip away from contact with the surface and drives an oscillation in the cantilever. Forces on the cantilever affect its resonant frequency, which can be measured. There are two kinds of NC-AFM: frequency modulation AFM (FM-AFM) and amplitude modulation AFM (AM-AFM). AM-AFM, also known as tapping mode, is more commonly used in ambient conditions AFM systems. It requires relatively large amplitude cantilever oscillations, which can be problematic for high-resolution imaging. Large amplitudes are required to stop local attractive van der Waals forces overwhelming the restoring force of the cantilever, and so disrupting the oscillation by snapping it into contact with the surface. Quartz tuning forks can replace silicon cantilevers in FM-AFM and have a number of favourable properties. These crystal oscillators are commonly used in electronics as timing devices and have high oscillation frequencies, high Q factors. Most importantly, their stiffness is such that they can be used safely at very low oscillation amplitudes close to the surface. FM-AFM is normally used in a UHV environment and is the AFM imaging method employed in this thesis.

2.3.3 Frequency Modulation AFM

In FM-AFM, force gradients applied to the sensor modify its resonant frequency. A combination of a phase-locked loop (PLL), and feedback control for the oscillation amplitude, control the amplitude, phase, and frequency of the oscillation driving signal. This is arranged such that the driving frequency matches the sensor resonant frequency, the sensor has a constant oscillation amplitude, and the driving signal is out of phase by 90 degrees with the oscillation of the sensor, as required for driving a damped driven oscillator. By tracking the changes in the sensor resonant frequency via a PLL, force gradients experienced by the sensor can be detected.

The free resonant frequency of the cantilever can be accurately measured while the cantilever is away from the surface. This is achieved by monitoring the oscillation amplitude and phase difference between the drive signal and sensor oscillation, whilst sweeping the driving frequency. Once the free resonance frequency is known, the oscillating tip can be approached towards the surface. Attractive forces acting on the tip can be seen as a decrease in the cantilevers resonant frequency, repulsive forces increase the resonant frequency.

Phase Locked Loop

A phase locked loop is a feedback loop whose outputs relate to the phase, frequency and amplitude of an input signal. A PLL is constructed from two components in feedback.

- A voltage controlled oscillator (VCO) produces a signal whose frequency relates to an input voltage
- A lock-in amplifier inputs a reference signal and a measured signal. The output is a DC voltage derived from the time average of the multiplication of the reference and measured signals. If the reference and measured signal are in phase, and the same frequency, a high DC voltage is returned. As the phase of the measured signal drifts away from the reference, the output DC voltage is reduced. Slight changes in frequency will lead to phase shifts between the source and reference signal.

2.3.4 AFM Theory

For a damped driven oscillator, the phase relationship between the driving signal and the resultant oscillation is given by Equation (2.5),

$$\phi = \arctan\left(\frac{-\omega}{Q\omega_0(1-\frac{\omega^2}{\omega_0^2})}\right) \tag{2.5}$$

where ω is the driving frequency, Q is the Q-factor, and ω_0 is the resonant frequency. This resonant frequency is related to the spring constant k of the sensor, as follows:

$$\omega_0 = \sqrt{\frac{k}{m_{eff}}} \tag{2.6}$$

where m_{eff} is the resonator's effective mass. The phase, ϕ, is seen to be $\pi/2$ when on resonance.

Force gradients experienced by the sensor modify the effective stiffness of the resonator, and as such a change in resonant frequency is induced. For very small amplitude oscillations, this change is related to the force gradient impinging on the sensor:

$$\Delta\omega = \frac{-\omega_0}{2k}\frac{\delta F}{\delta z} \tag{2.7}$$

Because the forces applied to the sensor are comprised of both attractive and repulsive components, according to Figure 2.2, the sensor frequency shift will be pushed negative, and then positive, as a result of reducing tip-sample separation. As a result of this complicated relation between force and tip-sample separation, feedback of the tip height is often switched off so that constant height images can be acquired.

Force Spectroscopy

A key tool available to the AFM user is that of force spectroscopy, though the term spectroscopy is poorly applied. True spectroscopy generally in-

volves a measurement with relation to energy. Here, whilst keeping the horizontal, XY, position of the sensor fixed, and varying the tip-sample separation, the frequency shift is tracked. A profile of the forces impinging on the sensor can be calculated. Unfortunately, this is a non-trivial operation. Two key problems exist. Firstly, force spectroscopy measurements are often performed over molecules of interest. As such, only forces from the molecule are of interest. Attractive van der Waals forces from the substrate, as well as any electrostatic forces from charges or static dipoles on the tip, will also have an impact on the tip. This can be compensated for by performing two identical force spectroscopy measurements, one over the feature of interest, and the other over the clean substrate. These are termed the On and Off spectra. By subtracting the resultant frequency shifts, a spectral measurement can be generated that only consists of force contributions from that surface feature, as illustrated in Figure 2.3.

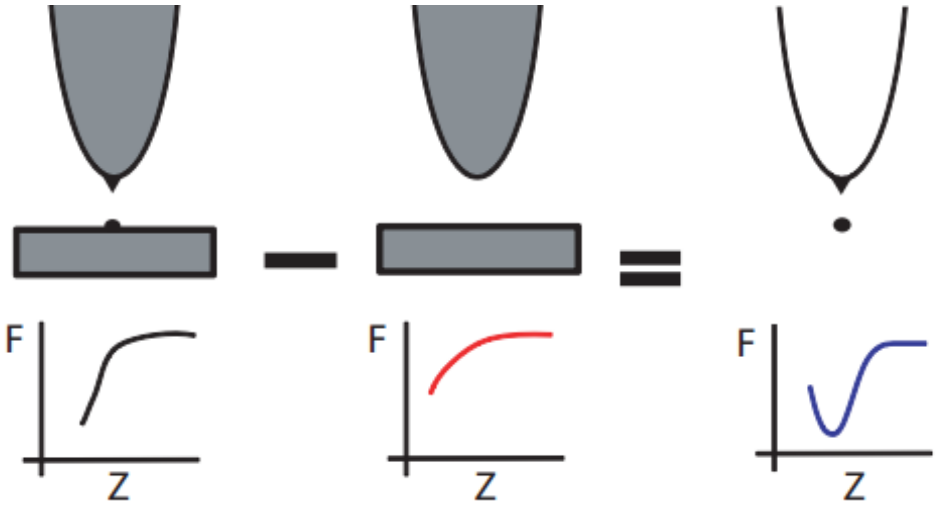

Figure 2.3: The subtraction of substrate and object of interest force contributions.

The second key difficulty is in extracting the actual force contributions onto the tip from the measured cantilever frequency shifts ($df(z)$). Equation (2.7) is insufficient as it only holds for very small oscillation amplitudes $<$1Å. Normal oscillation amplitudes are often much larger, so this equation

though is in general correct, is insufficient to accurately extract force data from frequency shifts.

A series of equations of significant complexity have been derived that properly relate the frequency shift to the force and energy of the tip-sample interaction. These are described in detail by their authors [19, 20]. Although a detailed derivation is not necessary in the context of the work in this thesis, it is, of course, useful to note their functional form:

The more general formula for relating force to frequency shift was derived by Giessibl [19]:

$$\frac{\Delta\omega}{\omega_0} = \Omega(z) = -\frac{1}{\pi a k}\int_{-1}^{1} F(z + a(1+u))\frac{u}{\sqrt{1-u^2}}du \tag{2.8}$$

where a is the amplitude of oscillation, z is the minimum tip sample separation during the oscillation, $u = \cos\phi$, and F is the force between the tip and sample.

From this, the formula for the force and energy, as a function of z, was be derived by Sader and Jarvis [20]. Where the force is:

$$F(z) = 2k\int_{z}^{\infty}\left(1 + \frac{a^{\frac{1}{2}}}{8\sqrt{\pi(t-z)}}\right)\Omega(t) - \frac{a^{\frac{3}{2}}}{\sqrt{2(t-z)}}\frac{d\Omega(t)}{dt}dt \tag{2.9}$$

And the energy is:

$$E(z) = 2k\int_{z}^{\infty}\Omega(t)\left((t-z) + \frac{a^{\frac{1}{2}}}{4}\sqrt{\frac{t-z}{\pi}} + \frac{a^{\frac{3}{2}}}{\sqrt{2(t-z)}}\right)dt \tag{2.10}$$

where t is a dummy variable included that represents the tip-sample separation, like z. This is such that z is not both the lower bound of the integral and the integration variable.

By applying these equations numerically to $\Delta\omega(z)$ data, accurate force and energy values can be returned. This provides a powerful tool in

analysing tip-sample forces. This, combined with grid spectroscopy techniques, where grids of $\Delta\omega(z)$ spectra are collected over a molecule of interest, provides detailed force information.

A notable parameter is the so called 'turn-around force'. This is the calculated force at a tip-sample separation where the force gradient is zero. Here the Pauli repulsive forces have 'turned the tide' and start to become relevant. This value can give the AFM user an idea of the relative magnitudes of the forces impinging on the AFM sensor.

2.4 The Qplus Sensor and the Createc System

The commercial Q-plus sensor replaces a cantilever with a quartz tuning fork where one arm of the fork is glued to a mount to position the sensor. The other arm has a tungsten wire glued to its end perpendicularly to act as an SPM tip. This sensor has very well understood dynamics, it not only can perform AFM measurements but due to a conducting tip can perform STM too. Due to its high spring constant and Q factor, it performs excellently as a probe for AFM/STM measurements.

All experimental results described in this thesis were collected via a Qplus sensor in a Createc UHV, low temperature (77K, 4K) scanning probe microscopy system. This includes separate sample preparation and measurement chambers and an advanced vibration isolation system for the scan head. A large dual cryostat provides cryogenic cooling of the scan head via an inner liquid nitrogen or liquid helium cryostat, and an outer, sacrificial, liquid nitrogen cryostat. The entire system sits atop four air legs, for dampening low frequency vibrations. Control electronics and software for the STM/AFM were provided by Nanonis. A photograph of the Createc system is provided in Figure 2.4.

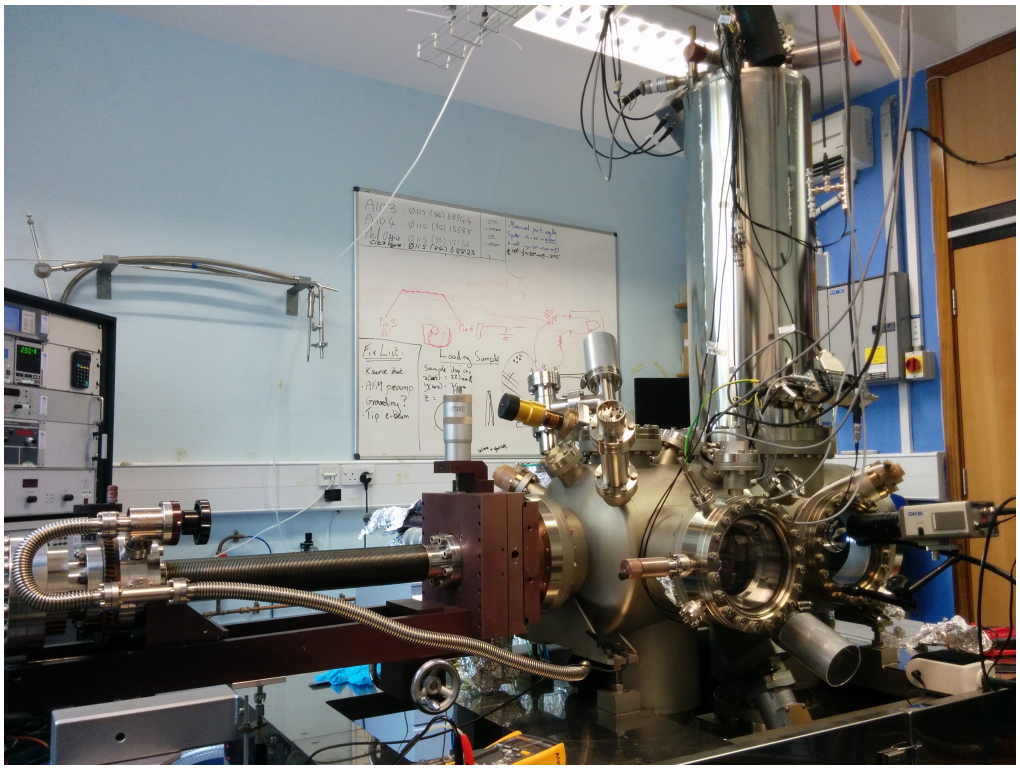

Figure 2.4: The Createc low temperature STM/AFM UHV system.

Chapter 3

Theoretical Methods Background

3.0.1 Chapter Overview

In this chapter, the techniques and concepts used to model and interpret molecular systems, imaged via STM/AFM, are introduced. As Hückel theory and Monte Carlo simulations make up the vast majority of theoretical content in this thesis, these will be examined.

3.1 Hückel Theory

Hückel theory is primarily used to simulate the wavefunctions of planar molecules, though it can be used with other molecules that meet certain conditions. It is relatively simplistic in its formalism and makes assumptions that limit its scope. However, where it is applicable, it can accurately reproduce experimental results. An advantage it holds over competing techniques such as DFT is that it is many order of magnitudes faster. It is not an iterative procedure and does not need to compute any integrals. Due to its limitations and speed the method makes an excellent investigatory tool. Within the context of this thesis, Hückel theory has been used exclusively to model C_{60} molecular orbitals (MO).

Background

Hückel theory was originally formulated by Erich Hückel in 1931 [21]. It has since been used extensively in chemistry and physics to investigate the electronic properties of molecules. Hückel theory is primarily used to model molecular electronic wavefunctions. It has some limitations with respect to other methods, such as DFT, however it remains a powerful contender. For Hückel theory to investigate a molecule, the molecule must hold a certain set of properties. Firstly, molecular orbital (MO) structure must be dominated by π bonding orbitals. This is because Hückel theory does not take into consideration σ or other bonding orbitals. The molecule should

be a planar molecule, though exceptions do apply and are particularly important in the case of the work described in this thesis. Finally, the molecule must exhibit conjugated bonding, that is, it has alternating double and single bonds between its atoms.

Hückel theory can be applied to C_{60} as the molecules radially protruding p_z bonding orbitals do not significantly overlap or interact. This is to say that p_z orbitals of neighbouring atoms are effectively parallel. As such even though the molecule is a spherical cage, it can be approximated as a planar surface.

Within these sets of limitations, Hückel theory has been demonstrated to produce remarkably accurate representations of physical systems. It can do so with very little computational power/time as compared to DFT. Hückel theory's speed, and also drawback, is partially due to the fact that it does not directly calculate physical energies for MOs – only the MO shapes are returned.

Formulation

Hückel theory is based on the principle of the linear combination of atomic orbitals (LCAO) and that each atom within the molecule will contribute a single electron to the π bonding network [9]. Each atom has a π atomic orbital associated with it. When they are linearly summed together, a basis molecular orbital is formed. Atomic orbitals (AO) are summed to form a MO:

$$\Psi = c_1\psi_1 + c_2\psi_2 ... + c_n\psi_n \tag{3.1}$$

where Ψ is the molecule's MOs constructed from p_z atomic orbitals ψ_i, for n atoms in the molecule. The c_i are dimensionless prefactors that must be calculated to get the full form of the MO. Hückel theory returns

these dimensionless prefactors, c_i. Thus with the addition of a function to model the atomic orbital, ψ_i, the full molecular orbital can be constructed. Hückel theory works by initially inputting this molecular orbital basis into the Schrodinger's equation:

$$H\Psi = \epsilon\Psi \implies (H - \epsilon)\Psi = 0 \tag{3.2}$$

To find the form of the MOs and energy levels ϵ, this equation must be solved by making a few assumptions and generating a suitable Hamiltonian H. As there will be n different energy levels a matrix formulation is used for convenience. The Hamiltonian can then be seen as an $n \times n$ adjacency matrix. To construct the Hamiltonian a number of different assumptions are made. Considering three atoms i, j and k. Where i is adjacent to j but not k,

$$H_{ii} = \langle\psi_i|H|\psi_i\rangle = \alpha \tag{3.3}$$

$$H_{ij} = \langle\psi_i|H|\psi_j\rangle = \beta \tag{3.4}$$

$$H_{ik} = \langle\psi_i|H|\psi_k\rangle = 0 \tag{3.5}$$

It is assumed that the atomic orbitals of non-adjacent atoms do not interact (Eqn. 3.5). This is represented by a zero in the corresponding location in the Hamiltonian adjacency matrix. For atoms that are adjacent the interaction is given an energy β (Eqn. 3.4), an arbitrary assignment that is known as the resonance integral. The interaction energy of an atom with itself, denoted α, is also an arbitrary assignment and is known as the Coulomb integral (Eqn. 3.3). Using these assumptions to construct the Hamiltonian matrix, and substituting it into Equation 3.2 yields:

$$\begin{array}{c} \text{1st atom} \\ \text{2nd atom} \\ \vdots \\ \text{nth atom} \end{array} \begin{pmatrix} \alpha-\epsilon & \beta & \cdots & \beta \\ \beta & \alpha-\epsilon & \cdots & \vdots \\ \vdots & \vdots & \ddots & \vdots \\ \beta & \cdots & \cdots & \alpha-\epsilon \end{pmatrix} \begin{pmatrix} c_1 \\ c_2 \\ \vdots \\ c_n \end{pmatrix} = 0$$

By dividing this Hamiltonian through by β, the Hamiltonian becomes solely comprised of 1's, 0's and the constant $(\alpha - \epsilon)/\beta$, — purely numerical matrix. Using this Hamiltonian, the molecular orbitals n energy levels can be found by calculating the eigenvalues which are independent of α and β. This assumption is the reason the energy levels cannot be exactly known – only the degeneracies and the relative levels are computed. The eigenvectors of the equation become $[c_1, c_2, c_3, \cdots, c_n]$ and provide the necessary information to construct theoretical molecular orbitals at each degenerate molecular energy level, according to Equation 3.1.

Because the only serious calculation is to diagonalise an $n \times n$ matrix, this process is extremely fast. Once this has been calculated the only computationally intense procedure is to calculate the molecular wavefunction at a desired point. This involves summing the contributions from all n atomic p_z orbitals at that point according to the pre-calculated prefactor c_n. This process is relatively computationally cheap.

Modelling C_{60} with Hückel theory

Simulated STM images

An STM will sample the electron density of a surface. As the electron density is the modulus squared of the MO wavefunction it is possible to model what an STM would measure over a C_{60} molecule using Hückel theory. This is done by creating a grid of points over the molecule where the desired image is to be taken. The relative vector from each point to

each atom is then calculated (Fig. 3.1). The wavefunction of a $2p$ orbital

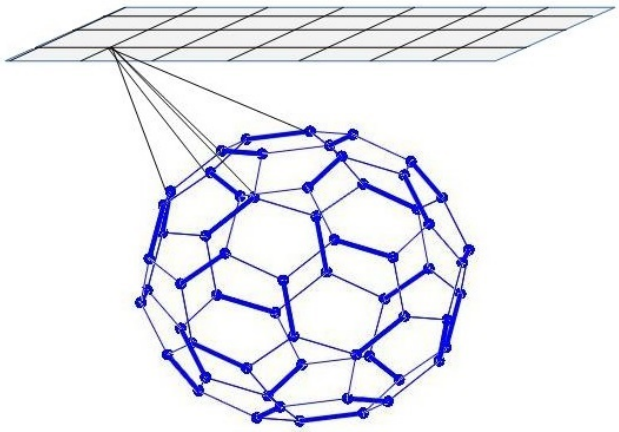

Figure 3.1: The grid above the molecule represents the points calculated for a simulated constant height scan. For each point on the grid the molecular orbital, as calculated by Equation 3.1, is squared to get the electron density. In this figure only a small number of lines are drawn to represent the vector calculated between the atoms and the pixel.

is a function of this vector and can approximated by a Slater type orbital (STO):

$$\psi(x,y,z) = \left(\frac{\zeta^5}{\pi}\right)^{\frac{1}{2}} z e^{\zeta\sqrt{x^2+y^2+z^2}} \tag{3.6}$$

where x, y and z are Cartesian coordinates, and z is orientated radially outwards from the C_{60} molecule. ζ is the Slater exponent defined as:

$$\zeta = \frac{Z_{\text{eff}}}{na_0} \tag{3.7}$$

where Z_{eff} is the effective nuclear charge, and a_0 is the Bohr radius. For the p_z orbital of carbon, ζ has been determined to be 1.568 [22].

The set of p_z wavefunctions for all 60 atoms are subsequently summed and a total wavefunction for that point calculated. The wavefunction squared gives the electron density (which is related to the LDOS) and so is equivalent to a point measurement for an STM.

Constant current images can also be generated by adjusting the height above a molecule of a pixel until its electron density value is at a pre-

determined value. This same predetermined value is used for all other pixels so that a constant electron density (current) image is generated. As this process involves calculating the wavefunction multiple times per pixel to calculate to correct height, this process is much slower. Simulated STM images of isolated C_{60} molecules using the MOs from Hückel theory [23, 24, 25] accurately reproduce experimentally-observed features, as shown in Figure 3.2 for molecules in three common orientations. These models are highly useful for interpreting and modelling C_{60} molecules. By comparing STM images to simulated STM images it is possible to interpret what orientation the actual molecule is in.

Splitting Degeneracies

A number of effects can cause energy levels within a C_{60} molecule to split. These can include interactions with the surface or a nearby object, as well as charging. Splitting due to charging could be caused by the Jahn-Teller effect. A direct implication of splitting levels is that when imaging the molecule via STM, a different set of MOs are sampled when scanning, leading to a different image. One method of modelling the surface interaction interprets it as a van der Waals force acting vertically on each of the atoms in the molecule. These van der Waals forces are incorporated into the Hückel Hamiltonian, and can induce a splitting in the molecular orbitals.

As well as modelling a vertical surface interaction, an angled interaction resulting from an adjacent step edge to the molecule can be modelled too. The effect of these perturbations not only cause a splitting in the energy levels but also slightly change the MO form.

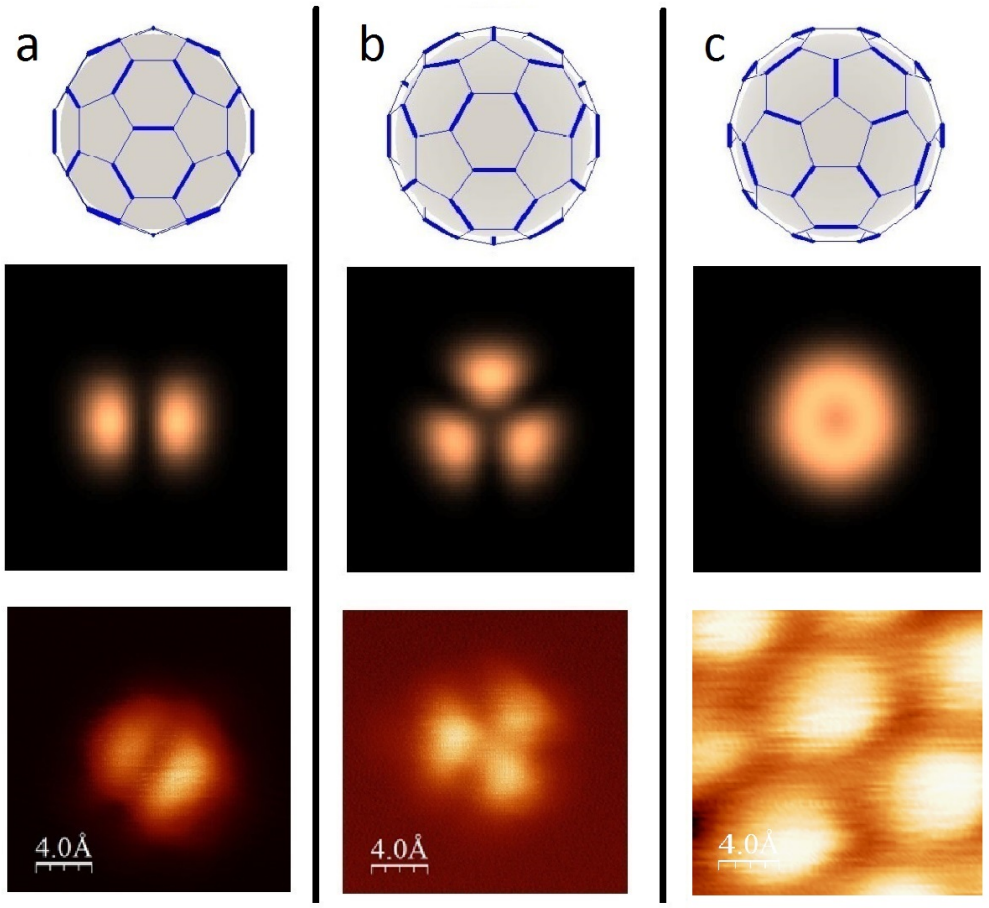

Figure 3.2: Three common molecular orientations as seen when looking down at the surface (top row). Their resultant simulated constant height STM scan (middle row). An experimental STM scan of a C_{60} molecule or molecules in that orientation (bottom row). a) The LUMO of a C_{60} oriented double-bond-down. b) The LUMO of a C_{60} oriented hexagon-down. c) The LUMO of a C_{60} oriented pentagon-down. In a) and b) the experimental images show isolated C_{60} molecules pinned to an NaCl step edge, imaged at in constant-height STM at 4K. c) shows a monolayer cluster of pentagon-down C_{60} molecules on Cu(111). Images by STM at 77K. Note that if a hexagon/pentagon/double-bond etc. faces the surface, a hexagon/pentagon/double-bond etc. will also be facing up away from the surface, due to the icosahedral symmetry of the C_{60} molecule.

3.1.1 Extended Hückel Theory

A drawback of Hückel theory is that it cannot predict energy values, and only considers π orbitals. To expand the versatility of Hückel theory, it must be reworked to what is known as extended Hückel theory. In basic Hückel theory, each atom is only assigned a single p_z orbital and non-adjacent atomic orbitals are considered to be non-interacting. Orbitals that are considered to interact are assigned an energy denoted by an un-

known variable α or β. These correspond to the diagonal and off-diagonal elements on the Hamiltonian respectively. This is not the case in Extended Hückel Theory. Here we consider in detail interactions between two frontier orbitals, the π and σ orbitals. These are constructed from p_x, p_y, p_z, and s orbital functions. Interactions between these are considered between every atom in the molecule, not just adjacent atoms. Values for α are determined empirically as the negative of the molecular ionisation potential. The β terms are calculated by considering the overlap integral between the different orbitals considered. Thus the technique becomes semi-empirical in nature.

To construct the Hückel Hamiltonian two functions are required for the diagonal and off-diagonal elements.

$$H_{ii} = -E_{ion} \tag{3.8}$$

$$H_{ij} = KS_{ij}\frac{H_{ii} + H_{jj}}{2} \tag{3.9}$$

where E_{ion} is the ionisation potential, S_{ij} is the overlap integral between the ith and jth atomic orbitals, K is the Wolfsberg-Helmholtz constant (estimated at 1.75 for hydrocarbons [26])

Once the Hamiltonian has been calculated, it may be diagonalised as before to provide coefficients for a LCAO, in the same way as before. For a C_{60} molecule a 240×240 Hamiltonian must be constructed, as there are four orbitals per sixty carbon atoms to consider. An example of the EHMO Hamiltonian for C_{60} is shown in Fig. 3.3.

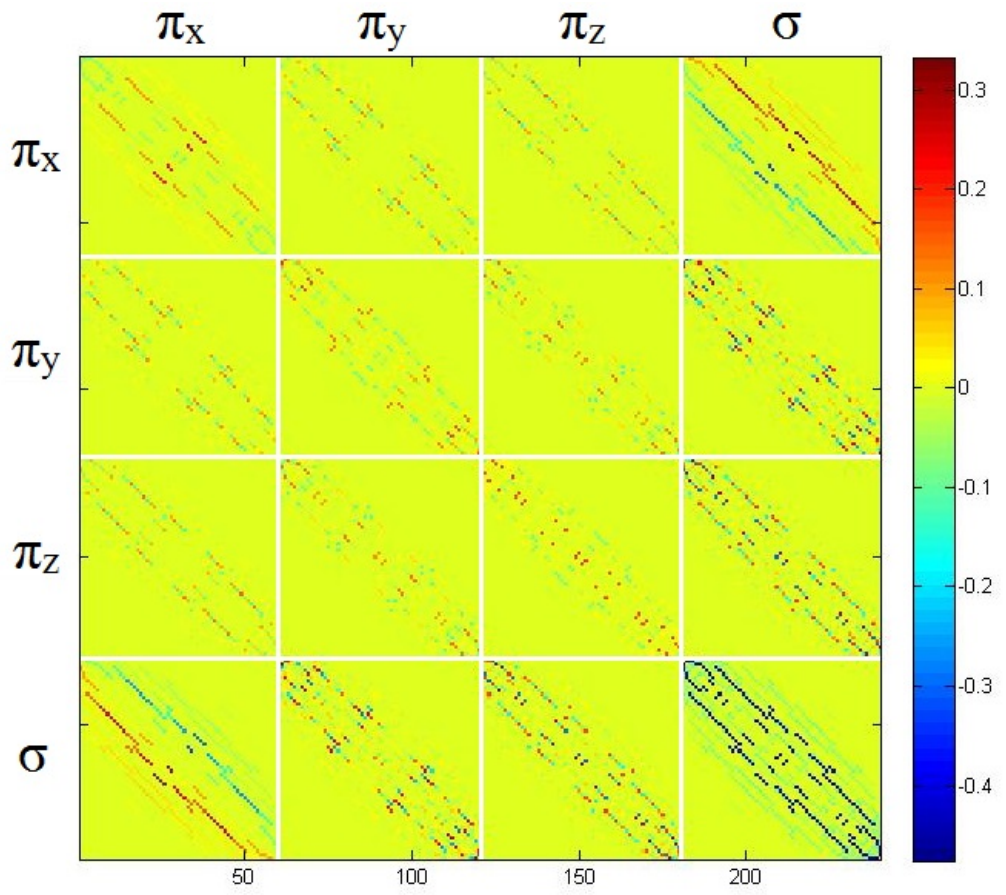

Figure 3.3: A graphical representation of the Extended Hückel Hamiltonian for C_{60}. The Hamiltonian is split into a 4×4 grid. Each section corresponds to an overlap between two atomic orbitals, for each of the 60 atoms in the molecule.

3.2 Monte Carlo Methods

Monte Carlo methods are a series of computational techniques that rely on the use of random numbers to solve complex problems. Time-dependent problems will often incorporate recursive methods. The applications of this set of techniques are wide-ranging across multiple technical fields, from plasma particle simulations and surface adsorbate motion, to financial market analysis and digital signal processing. Monte Carlo techniques and strategies are used to find optimal solutions to complex problems, be it a computationally expensive integral, or a physical system with many interacting degrees of freedom.

3.2.1 Example uses of Monte Carlo methods

The following two examples of Monte Carlo simulations serve to demonstrate the technique's versatility and power.

Calculating π

A common example for Monte Carlo methods is in the calculation of π, 3.14159... To do this, a set of random points are generated spatially within a square. A circle is considered to sit within the square, such that its diameter is the width of the square. A random point that is generated within the square will have a probability to land inside the circle of $P = \frac{\pi}{4}$. The value of π is determined by observing the fraction of points that lie inside the circle by the total number of samples, as seen in Figure 3.4. As more points are used in the calculation, the accuracy of the estimate increases.

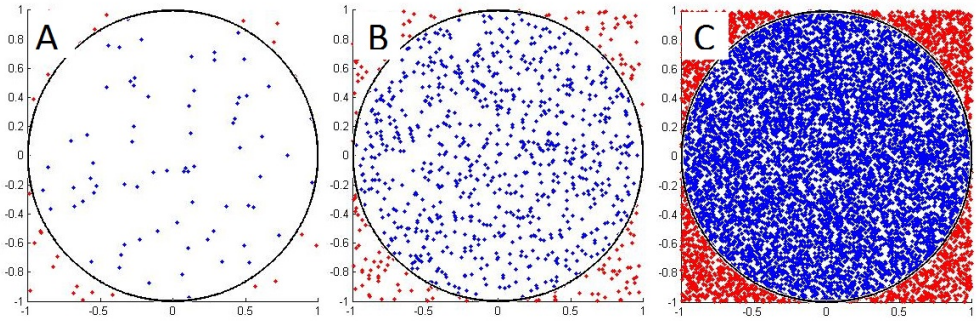

Figure 3.4: A Monte Carlo simulation to estimate the value of π. (A- C) 100, 1,000, and 10,000 randomly generated points are used with an estimated value for π of 2.8800, 3.2520 and 3.1512 respectively. Note these values are approximate results as a result of the stochastic nature of the simulation. Subsequent runs would return different results, but with similar accuracy.

System State Estimation - Particle Filtering

A more advanced example is that of a particle filter in digital signal processing. This is used to estimate the state of a system given a series of measurements. Here a sample of randomly generated particles are used to

iteratively estimate the time-dependent state of an observed system. Significant measurement noise makes this a non-trivial task. In this example a system has an initial estimate of its state. Sequential measurements of the system will provide information for the filter to estimate the system state.

Firstly, a sample of normally distributed particles are distributed around an estimate of the state at time $t = 0$. An estimate must be generated of the new state of the system at time $t = t + 1$. Each particle is spatially advanced according to a model of the system dynamics such that each particle is sampling a possible state of the system at $t = t+1$. A measurement of the system is performed. Each particle is then designated a probability that it is the new system state, given the system measurement. A new state estimate is ultimately selected from the distribution of particles, as weighted by their assigned probabilities. This process is then iterated to continue tracking the system state through time. Increasing the number of particles increases the accuracy of the state estimation. Even if the system model is inaccurate or incomplete, the stochastic nature of the filter will enable accurate state estimation. An example of a particle filter is shown in Fig. 3.5.

3.2.2 Monte Carlo Techniques in Surface Science

In surface science, Monte Carlo methods are often utilized to model complex processes involving the motion and interactions of surface adsorbates. The motion of these can be modelled in multiple different ways, depending on the exact physical configuration of the system. For example, an adsorbate might be modelled to exhibit a random walk, where the probability of stepping in one direction or another is influenced by its specific adsorbtion site within the simulation.

A particular technique of interest is the kinetic Monte Carlo method. Here an element, or system of elements, is to be simulated in time. The

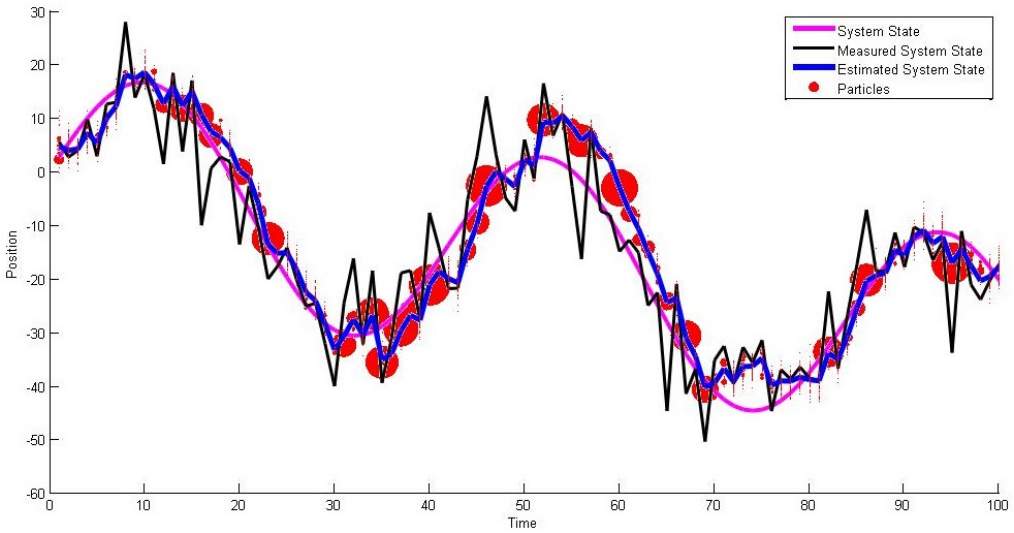

Figure 3.5: A particle filter tracking a noisy signal. The clean signal is a sinusoidal signal with a negative gradient. One hundred particles are generated at each time step. Prior knowledge of the sinusoidal element within the signal assists in the tracking. The circles indicate the filter particles. The size of the particle relates to its likelihood of being accurate, relative to the other points in the random distribution.

local environment or other elements in the system influence the state of the system through time. The basic kinetic Monte Carlo algorithm is as follows.

1. Consider an initial system state at $t = 0$

2. Select an initial state k to initialise the simulation. This initial state can be the system in an initial random configuration, or k can be crafted to influence the progression of the system.

3. Consider all possible states i, the system could transition to. Where the total number of available states to the system is N_k. Consider the energies of those states, and the energy of the current system state.

4. For thermally activated systems, using a Boltzmann factor, calculate the rates $r_{k\to i}$ at which the system would transition to those N_k states.

5. Compute the cumulative sum, R_{ki}, of the transition rates, $r_{k\to i}$. where $Q_k = R_{kN_k}$ is the total sum of the transition rates. R_{ki}/Q_k is the normalised cumulative sum. Here, each transition rate now occupies a

space on a number line between 0 and 1. The size of the space occupied by each state on the number line is proportional to its transition rate, $r_{k\to i}$.

6. Transition the system to the next state of the system at $t = t+\Delta t$ by using a random number to select a new state. Here a random number between 0 and 1 selects an element from R_{ki}, such that the likelihood of choosing a particular state is proportional to its transition rate $r_{k\to i}$.

7. Advance the time step as a function the transition rate from the old to new state. Where $\Delta t = Q_k^{-1} ln(1/u)$, where u is a random number between 0 and 1. Note that over a large number of iterations, the average value of $ln(1/u)$ is 1, such that the average value of $\Delta t = Q_k^{-1}$. As such the advance in time step is related to the total rate Q_k, not just the transition rate $r_{k\to i}$ of the chosen state i.

8. Return to Step 3.

For example, a system at initial state k has four possible states to transition to:

Possible States, i	a	b	c	d
Transition Rates, $r_{k\to i}$	1	14	4	54
Cumulative Sum, R_{ki}	1	15	19	73
Normalised, R_{ki}/Q_k	0.0137	0.2054	0.2603	1.0000

A random number is then chosen between 0 and 1, for example 0.1024. This is seen to fall between a and b on the normalised cumulative sum, thus b is chosen to be the next system state. The higher the transition rate to a state, the higher chance that state has to be chosen for the next system state. A new set of possible states and transition rates are then considered to continue the Monte Carlo algorithm.

Chapter 4

Monte Carlo and Hückel Theory Study of C_{60} Assemblies - Background, Simulation Design and Validation

4.0.1 Chapter Overview

In this chapter a combined Monte Carlo and Hückel theory simulation is developed. It contains a detailed description of its workings, and its validation against other models.

4.1 Introduction and Background

When deposited onto substrates such as close-packed planes of fcc metals or NaCl multilayers, and given sufficient thermal energy, C_{60} molecules aggregate into islands. These islands assume a close-packed structure [27] for both monolayer and multilayer samples. At ambient temperature, molecules in multilayers will rotate freely around their centres [28]. Upon cooling below a transition temperature, free molecular rotations are frozen out [28]. In this state, C_{60} molecules reduce their respective interaction energies by rotating to a configuration whereby the total energy of the island is reduced [29, 30, 31, 32, 33, 34, 35, 36]. In monolayers, the molecules will also rotate, but rotations are not free due to surface interactions. When imaged using scanning tunnelling microscopy (STM), it is possible to distinguish between different molecular orientations by interpreting the shape of individual molecules [37]. Complex rotational order has been observed in both mono- and multilayered islands. Specific rotational structures typically depend on the substrate and on the layer thickness [29, 30, 31, 32, 33, 34, 35, 36].

In multilayered islands, and on a number of different substrates including NaCl, Au(111), and Cu(111), a variety of (2×2) 'pinwheel' superstructures have been observed [29, 38]. This is where a hexagon-down molecule, observed as a three-lobed feature in STM, is surrounded by double or single bond-down molecules, observed as two-lobed or single lobed features respectively, in a pinwheel formation. These (2×2) superstructures are of-

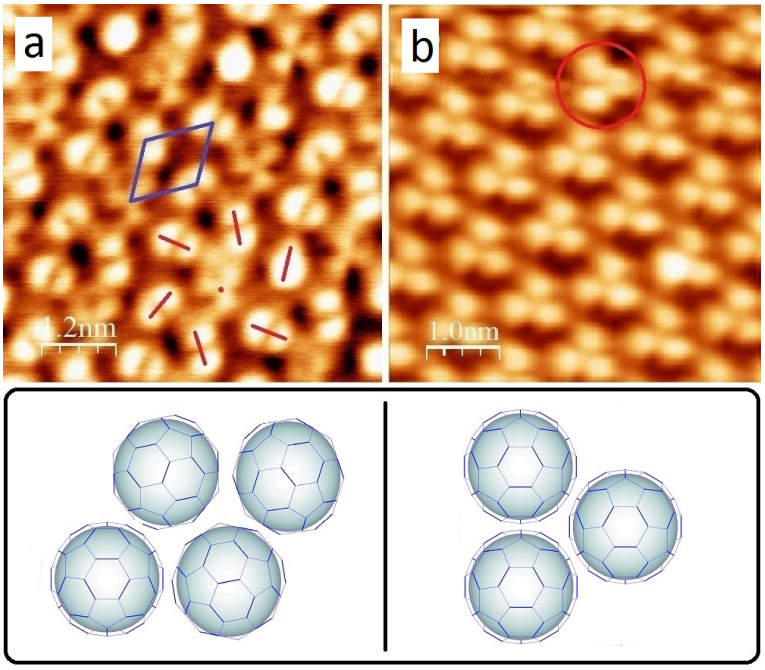

Figure 4.1: Two experimental STM images of C_{60} islands. Below are wire-frame representations of the molecular orientations. a)A C_{60} multilayer on NaCl. An orientational 'pinwheel' structure is observed where a hexagon-up molecule, indicated by a dot, is surrounded by six double-bond-up molecules, indicated by straight lines. The resultant (2×2) unit cell of the superstructure is indicated by a rhombus. These structures have previously been observed in other C_{60} layers [29]. b)A commonly observed (4×4) superstructure on Cu(111), where C_{60} molecules in a monolayer all sit hexagon-up and align. Here one molecule has adopted the second, less favourable, orientation and is circled. Molecules in this hexagon-up configuration are also commonly seen on the Au(111) substrate.

ten similar to those observed in bulk C_{60} [39, 28]. An example of adsorption on NaCl is shown in Figure 4.1a.

On Cu(111), isolated C_{60} molecules chemisorb and are seen to sit with a hexagon face directed towards the surface (hexagon-down). The hexagon face of the C_{60} will align with the (111) layer below. Two principal binding configurations at 180° to each other are available, as described by Larsson et. al. [40]. In an island, intermolecular interactions are sufficient to make one of the two configurations more favourable; the other is rarely seen, leading to the ordered (4×4) structure. Figure 4.1b shows an experimental STM image in which all except one molecule adopt the same most favourable configuration, with the remaining molecule adopting the least favourable orientation. Other molecular orientations are possible but are

observed less frequently, such as pentagon-down molecules. On Au(111), the C_{60} molecules adopt a superficially similar hexagon-down orientation, but with a different adsorbtion to the gold, exhibiting a C_{60}/Au(111) - $(2\sqrt{3} \times 2\sqrt{3})R30°$ structure. On Au(111), C_{60} molecules are less-strongly bound than on Cu(111). This results in a higher proportion of pentagon-down molecules. A table summarising these molecular configurations of interest is provided:

Configuration	Structure	Details
C_{60}/Cu(111)	(4×4)	Molecules strongly bonded to substrate, primarily hexagon-down orientation.
C_{60}/Au(111)	$(2\sqrt{3} \times 2\sqrt{3})R30°$	Molecules somewhat bonded to substrate. Primarily hexagon-down orientation, but with notable pentagon-up defects.
C_{60}/NaCl	(2×2)	Molecules very weakly bound to substrate. Bilayers formed with complex long-range pinwheel orientational structure.

In this, and the next, chapter we seek to understand why this variety of orientational orderings arises.

Most approaches to simulating C_{60} islands focus on monolayers. These typically involve fixing the molecules in a limited number of relative orientations and examining the system via density functional theory (DFT) [41, 42, 43]. This, however, has the disadvantage that it is impossible to simulate a multilayer as the orientations of the molecules below are unknown. Moreover, only a few specific orientations are sampled. The dynamics of the molecular orientations are clearly a highly complex system due to the complexity of the observed rotational structures. Therefore, to gain a better understanding of the system it is necessary to simulate very many more molecular configurations. A way to do this is via a Monte Carlo simulation. Unfortunately, it is impractical to use DFT to calculate the intermolecular interaction energies within a Monte Carlo study due to computing time

limitations.

Laforge et. al. [44] used a Monte Carlo simulation to model a bulk C_{60} system. A (2×2) pinwheel structure with molecular orientations similar to those seen in bulk C_{60} was generated. However the size of their Monte Carlo simulation was only 2×2 molecules across, as shown by the unit cell in Figure 4.1, totalling only 12 molecules across 3 layers. This is not ideal due to edge effects and the inability to simulate non-uniform effects or defects. Significant differences in methodology described below have allowed us to simulate systems on a much larger scale, including monolayer and multilayer assemblies.

As the size of the simulated assembly increases, computation time increases dramatically. This is not only because there are more molecules to consider, but also because increased degrees of freedom in the system lead to complex structures taking longer to appear in simulations. In Laforge et. al's methodology [44], intermolecular energies were calculated at every timestep. This, however, limits the simulation size again due to computation time constraints. In this chapter we demonstrate a methodology whereby a large number of intermolecular interactions are pre-calculated leading to dramatic simulation speed increases.

As there is no chemical bonding between the molecules in the C_{60} islands, we theorise that the molecules rotate to simply reduce the energy of the island due to intermolecular and surface interactions [35]. To simulate an island, we initially took two isolated molecules and examined the variation of the intermolecular energy. A unitless measure of the repulsive interaction energy was calculated for different molecular orientations via a novel application of the Hückel method. This process was completed for a high number of discrete relative orientations of the two molecules. Interactions with the surface substrate were also calculated. An island of molecules was then constructed. In this case, every molecule is allowed to

rotate independently to an orientation chosen via a Monte Carlo simulation. We will show that the results of our model accurately reproduce the orientational order and defects observed experimentally [29, 32, 45].

4.2 Simulation and Experimental Methods

4.2.1 Intermolecular Interactions

In C_{60} islands and multilayers, molecular spacing is fractionally reduced at low temperature [39, 28]. Below a threshold temperature, repulsive interactions will impede the molecules' free rotation and fix their orientations. Intermolecular repulsive interactions are primarily responsible for the resultant molecular orientations [46]. Here, attractive van der Waals forces provide a strong, but relatively uniform field [46], which means that their omission does not alter our overall results. Coulombic interactions, due to variations in charge density, have a similarly small effect on C_{60} molecular orientation [46], and accurate predictions of rotational order have previously been obtained in Monte-Carlo simulations excluding Coulombic interactions [44]. It should nevertheless be noted that this will not generally be true for other systems. Therefore, because our interest is solely in molecular rotation, only repulsive interactions will be considered.

Repulsive forces originate from a short-range Pauli exclusion regime, where overlapping orbitals from adjacent molecules distort at a very high-energy cost. For this simulation, we choose not to use an analytical potential for intermolecular interactions. The commonly used Lennard-Jones potential ignores the complex orbital structure of the molecule. The potential developed by Lamoen and Michel [46] attempts to approximate the potential by placing repulsive Born-Mayer interaction centers along the bonds, but this is somewhat artificial. We therefore incorporate Hückel Theory to model the true molecular orbital(MO) structure. Hückel Theory

models molecular orbitals via linear combination of atomic orbitals. It is ideally suited for molecules dominated by π bonding orbitals, such as C_{60}. As we only consider repulsive interactions, it makes sense to limit the simulation to solely pair-wise interactions. Thus by considering two adjacent molecules and integrating over the multiplicative overlap of their molecular orbitals, we can extrapolate a repulsive interaction potential. We do not incorporate density functional theory (DFT) due to the extreme computation time cost involved. Hückel Theory calculations are many orders of magnitude faster.

4.2.2 Comparison to DFT and a Lennard-Jones Potential

A comparison of our model against van der Waals-corrected DFT, and a Lennard-Jones approach, was performed for a selected set of relative molecular orientations. This was to ensure that our model did not deviate significantly from other established methods. Our model correlated remarkably well with the Lennard-Jones results, and demonstrates a qualitative match to the DFT results. Due to the similarity to the Lennard-Jones result, and subsequent results that closely match numerous experimental results, we believe that the Hückel model is accurate.

For all three models, we consider a pair of C_{60} molecules placed adjacent to one another. One of the molecules is then rotated, as shown in Figure 4.2, and the change in energy is tracked across the motion.

The normalised energy variation for the three different methods of calculating the intermolecular potential is shown in Figure 4.3. Normalisation is used to easily compare the shapes of the graphs. It was noted that in the Lennard-Jones approach, the attractive forces did not significantly contribute to the variations in potential. The Lennard-Jones parameters used were for a C-C interaction - $\epsilon_{cc} = 0.4396 kJmol^{-1}$ and $\sigma_{cc} = 0.3851$Å from

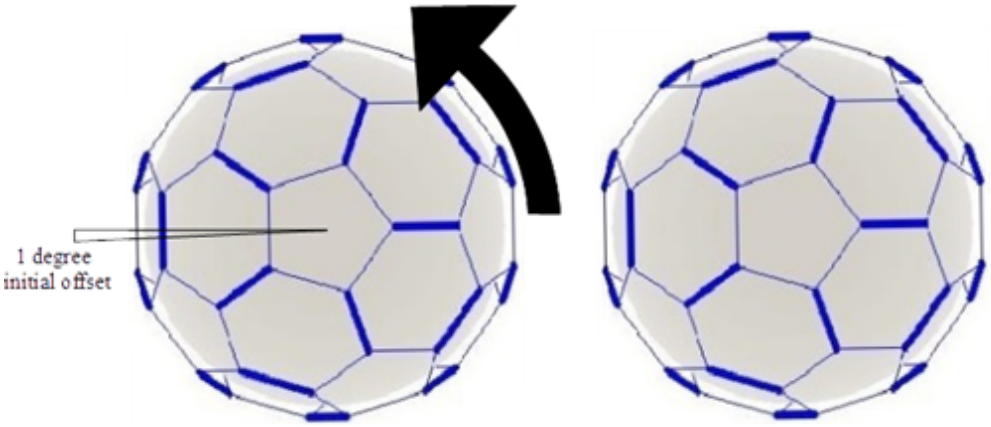

Figure 4.2: Two C_{60} molecules with a centre-to-centre spacing of 10.2 angstroms are employed. This separation corresponds to observed experimental data, and roughly corresponds to the C_{60} van der Waals radius. Both molecules are oriented pentagon-down and are oriented identically. There is an initial rotation of one degree around the Z-axis (vertical down through the page) on both molecules to break the symmetry of the operation. One of the molecules is then incrementally rotated 72 degrees about a vertical axis.

[47].

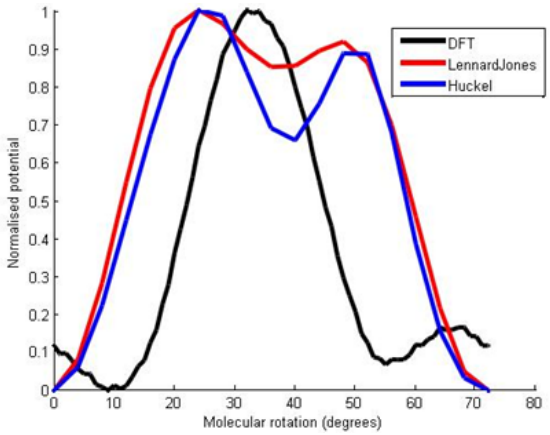

Figure 4.3: The Lennard-Jones and Hückel model is calculated in four degree steps. The DFT is calculated in 1-degree steps.

DFT calculations were carried out using the open source CP2K/Quickstep code, employing a hybrid Gaussian and plane-wave method. Goedecker, Teter and Hutter pseudopotentials and the Perdew Burke Ernzerhof generalized gradient approximation method were used with a 300 Ry plane-wave energy cutoff. We utilized the Grimme DFT-D3 method to account for dispersion interactions, and a double-zeta Gaussian basis set plus polarization (DZVP-MOLOPT). There was no relaxation in the model, all atom

coordinates were fixed. The DFT shows a qualitative correlation to the Hückel calculation with a high-energy region in the centre of the rotations and lower energy regions across the edges. The Hückel and Lennard-Jones methods correlate extremely well. The Hückel method based model was additionally compared to a model that instead utilised the Extended Hückel method. It was noted that there were no significant differences between the two.

4.2.3 Surface Interactions

A significant surface interaction is also inherently present between C_{60} molecules and a Cu(111) or Au(111) substrate. To incorporate an interaction with these surfaces, we make it unfavourable for molecular orbitals to project into the surface. Atom-down and single-bond-down orientations then unfavourably project significant electron density into the surface, favouring the hexagon-down orientations observed experimentally. While this does not directly model the actual physics of the C_{60}–surface chemisorption, the resultant outputs are in very good agreement with experimental observations. Using this model, the surface interaction has no influence on molecular rotations around the axis perpendicular to the substrate; only intermolecular interactions influence that degree of freedom.

4.2.4 Simulated STM images and Intermolecular Interaction Calculation

As shown earlier in Figure 3.2, Hückel theory can be used to estimate C_{60} MOs to generate simulated STM scans.

The MOs can also be used to estimate an interaction between two adjacent molecules. This is determined by integrating the multiplicative overlap of the two molecular orbitals, the area integrated being the bisecting plane between the two molecules. A grid of points is initially generated in the

plane perpendicularly bisecting the line connecting both molecules. The electron density from each molecule is then calculated at these grid-points (Figure 4.4) taking account of all 30 filled states of each molecule. Note that if interactions with the surface split the Hückel molecular orbitals, the results will be unaffected as the set of filled orbitals remains the same.

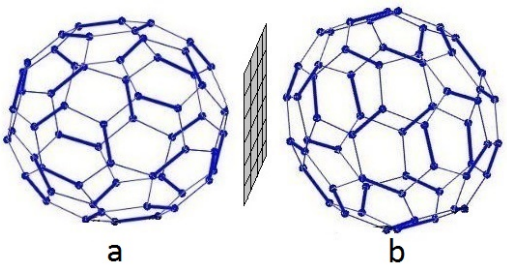

Figure 4.4: The grid between molecules (a) and (b) shows the locations where the electron density interactions are calculated.

The calculated planes of electron densities from each C_{60} are then multiplied together. In regions where there is a large overlap of the two electron densities, the multiplication returns large values for that region; conversely, in areas where there is little overlap a set of small values is returned. The resultant grid is then summed to complete the integration and return the total interaction 'energy' for that pair of molecules in that particular geometry, where

$$E = \sum_i \sum_j A(i,j)B(i,j) \tag{4.1}$$

A and B represent the grid of electron densities calculated from the molecule A and its adjacent molecule B, and i and j represent indices of the horizontal and vertical grid references respectively.

The surface interaction was calculated by taking a grid directly below the molecule. This was then squared and summed to give

$$E_{SI} = \sum_i \sum_j A(i,j)^2 \tag{4.2}$$

which makes any orbitals projecting into the surface 'high-energy' configurations. The exact form of this surface interaction is not highly important; other similar forms that penalise projecting orbitals produce very similar results. The two molecules are then rotated to a second set of orientations and the energies between them recalculated. This process is repeated until all significant relative orientations between the two molecules have had an energy calculated and stored in a table. The angular increment between orientations was set to approximately 3°, so as to capture all orientations of interest and get good resolution of intermediate orientations. The energy values for the surface interaction and the intermolecular interaction were normalised, resulting in a table of energies ranging from 0 to 1. This negates the adverse effect of the resolution of the grid affecting the magnitude of the resultant energy spectrum.

A major issue for this method is the physical size of the table, in terms of both its initial calculation and its subsequent storage. If all possible molecular orientational configurations for the molecule and each of its 12 neighbours (in a multilayer) were to be considered, the lookup table would have approximately 1×10^{12} elements. This would be impossible to hold in the memory of a computer and would take months to calculate. It is therefore necessary to consider the symmetry of the molecule to cut down on the number of possible orientations that need to be calculated.

Molecular orientations are defined by an axis-angle representation. Here a point on the surface of the molecule defines an axis passing through itself and the centre of the molecule. A rotation around that axis is then applied to achieve the final orientation. Figure 4.5 shows the smallest 'unit cell' of the molecule that contains all of the points that must be calculated. The mesh of points was generated such that the points were evenly spaced across the unit cell. The number of molecular orientations available to the simulation is thus the number of points multiplied by the number of

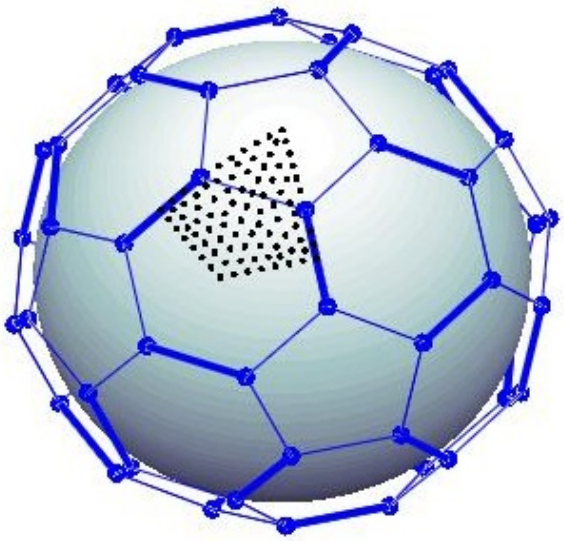

Figure 4.5: A net of points is superimposed on a C_{60} molecule. These define points on axes through the molecular center, from which molecular orientations can be defined. The area covered by these points represents the smallest possible area to capture all the information about the intermolecular interactions.

rotation segments to rotate about that point. In our simulation 94 points and 90 rotation segments leads to 8460 unique molecular orientations.

4.2.5 Generating the Mesh

A mesh of points over the C_{60} must fulfil a number of criteria. Firstly, every point must be at the same distance from the molecular centre, such that the mesh of points properly tracks the spherical surface of the molecule. Secondly, high symmetry points and axes of the C_{60} must be directly considered by points, or lines of points on the mesh. Finally, the points must be evenly spread across the surface so as not to bias one particular orientation with more detail.

To achieve this set of criteria, a meshing software (Gmsh) was employed. Initially, a geometric shape defining the high symmetry points and axes, and the curvature of the molecule was created. A mesh was then generated from this geometric shape with particular care given to the density of points and proper curvature of the mesh over the geometric shape. This is shown

in Figure 4.6.

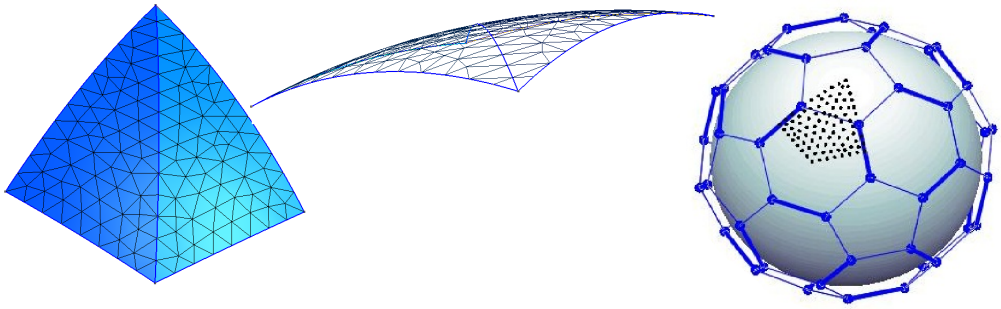

Figure 4.6: A mesh of points is generated to cover all high symmetry points, and a spread of points in between. The mesh geometry is a polygon mapped to the curvature of a sphere. It is shaped such that its four corners lie on the centre of a pentagon, the centre of a hexagon, and the centre of two double bonds. The polygon is additionally configured such that each edge lies along a molecular line of symmetry, the polygon has a spline down the middle to include a line of points along the central symmetric axis. The density of the points is tuned to make the total number of point approximately 100, which was seen as computationally feasible. The density of points was additionally tuned such that the mesh would sample across the single bond, the final high symmetry point.

4.2.6 Calculating Vectors to Points of Interest

For every unique molecular orientation, 14 vectors are generated that point towards adjacent molecules and features of interest, as seen in Figure 4.7. These are generated by initially considering the 94 orientational vectors, and not the axial rotation. A random axis is chosen for an initial set of 14 vectors originating from the initial vector. Once these vectors have been generated, they are rotated in 90 rotation segments around the original vector to give the full set of 8460 orientations and their respective 14 vectors.

4.2.7 Generating and Comparing Grids of Electron Density to Calculate Intermolecular Interactions

For each surrounding vector, a perpendicular grid of coordinates is calculated and the molecular electron density calculated at each grid coordinate.

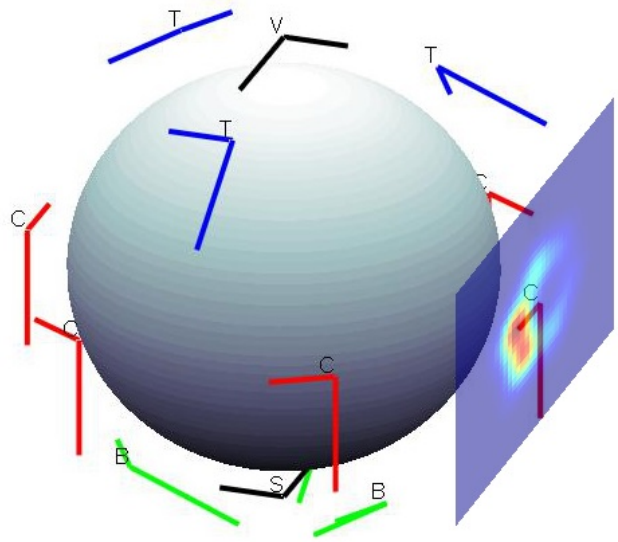

Figure 4.7: This image represents 14 surrounding vectors (generated from a single unique molecular orientation) from which electron density grids are calculated. Each L shaped line represents three components necessary to generate the grid at which the electron density is calculated. These are: (i) the distance between the centre of the molecule and the L defining the distance from the molecule the grid is calculated; (ii) the long arm of the L pointing towards the bottom of the grid; (iii) the short arm pointing towards the right side of the grid. It is critical that the grid orientations and locations are correctly defined. If not they will not line up with the grid for an adjacent molecule.
The lines labelled C point towards the six adjacent molecules in the same layer as the current C_{60}. The lines labelled B and T point towards molecules in the bottom and top layer around the molecule respectively. The line labelled S directly below the molecule points towards the surface to calculate the surface interaction. Finally, the line labelled V above the molecule points up from the island and is used to generate an image so the viewer can know what orientation the molecule is in. A grid of points directed towards an adjacent molecule and the respective calculated electron density is shown to illustrate its position/orientation.

This is the only time the electron density needs to be calculated, which contributes to the overall speed of the procedure. The location of a grid of electron density is demonstrated in Figure 4.7. The electron densities can be calculated using Hückel theory, although extended Hückel theory can be used as well. This is much more time consuming, however, short-range σ orbitals are then considered which could be important at the close ranges between the molecules. These grids of electron density are then used in Equation 4.1 according to their relative positions. That is to say, for a single orientation of the centre molecule, it will compare its 12 grids (via Equation 4.1) with its neighbour's grids pointing towards itself. As an ex-

ample, consider the comparison of a molecule with its top right neighbour in the same molecular layer. The molecule would submit its top-right grid points as defined by its current orientation, and its neighbour would submit its bottom-left grid point as defined by its molecular orientation. For every unique molecular orientation of the center molecule A, the adjacent molecule must be rotated and compared for all of its molecular orientations. This must be completed for all 12 neighbours.

Finally, the grid for the adjacent molecule B must be flipped horizontally before being compared to the grid from molecule A, as a grid observed from an adjacent molecule will have its i coordinates reversed. This can be seen in Figure 4.7 where two opposite points, labelled c, will have their horizontal components reversed.

This procedure returns an energy lookup table for every molecular orientation on every side of the molecule, and every adjacent molecular orientation. For 8460 unique molecular orientations and considering the 12 adjacent molecules, there are $\approx 10^9$ unique intermolecular interactions that must be calculated. The table generation was single-threaded and written in MATLAB. It took only 6 hours to generate on a desktop computer using a single 3.2Ghz processor core and 12GB of RAM. A large (60GB on an SSD) page file was used during the table generation which significantly slowed down the procedure. The final intermolecular interaction table was 7GB, which easily fits in RAM.

4.3 Monte Carlo simulations

A kinetic Monte Carlo simulation was written to consider a cubic island of hexagonally packed C_{60} molecules with periodic boundary conditions (Figure 4.9). A molecule is chosen at random and rotated to a new orientation. All pre-calculated orientations are available for molecular rotation, where

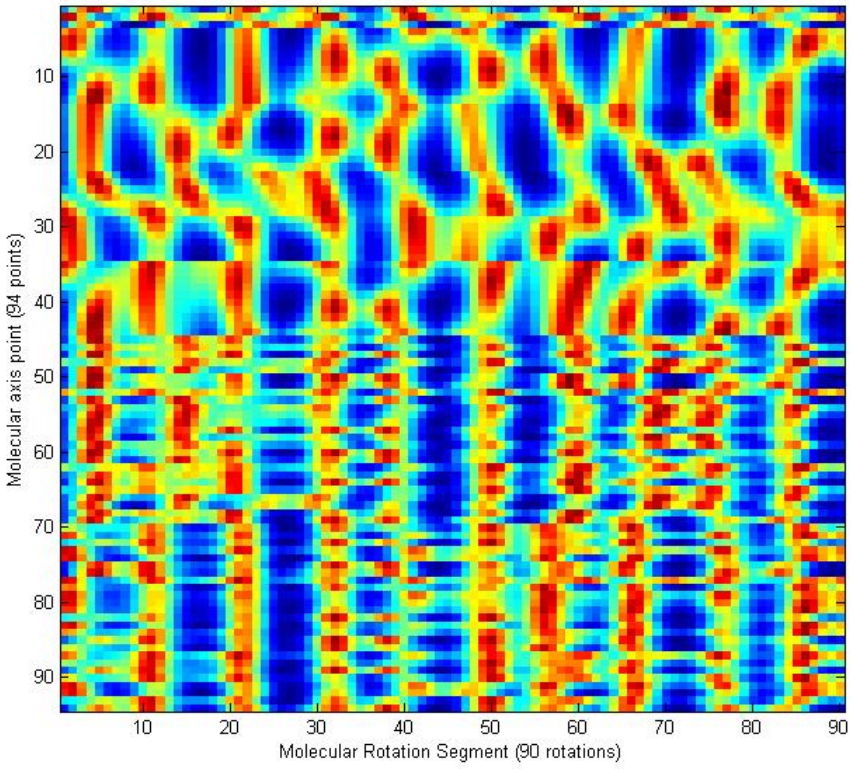

Figure 4.8: A graphical representation of an output from the table generation process. This considers an adjacent molecule in a particular orientation. The heat map shows what energy the molecule would be at if it rotated to one of the 8460 orientations available to it. This represents a minute fraction of the total data produced from the table generation process. A total of 101520 of these data sets are generated for the complete data set. Note the ordered nature of the heat map in the top third of the image. This is due to the order the points are displayed in as determined by the meshing software. The first set of points are consecutively adjacent to one another as the mesh first outputs points along the vertices of the geometric shape. After this, points are randomly sampled from within the mesh, leading to the disordered appearance of the lower two thirds of the image.

the probability of a molecule attaining a particular orientation is weighted according to its energy landscape. Additionally, the molecules centre positions are fixed. This is an approximation as molecules could undergo small local shifts in position as a result of orientational order, and surface vacancy formation could additionally lead small changes in molecular height, but these changes are likely to be small. The island must have an even side length but can otherwise be arbitrarily scaled up in size. For multilayers,

an FCC, or 'ABC' packing arrangement is employed.

4.3.1 Configuring Island Hexagonal Packing

Each molecule within the island must know the index of its 12 neighbours, in the context of a multilayer. The size of the island must also be able to be changed at will. Finally, molecules must be able to be removed to create vacancies, or shape islands.

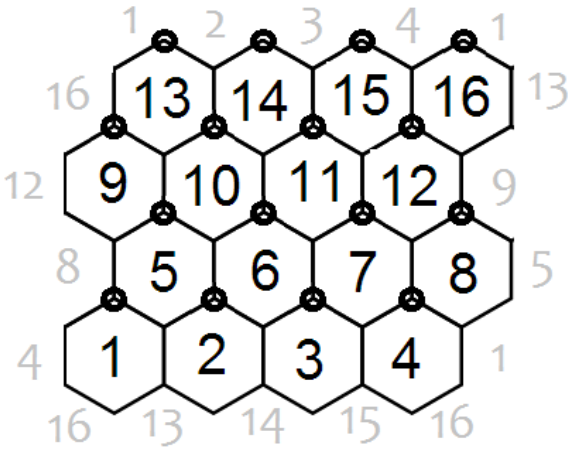

Figure 4.9: A 4×4 island is shown with corresponding periodic boundary neighbours labelled. The small circles represent the location of molecules in the case of a 2nd layer above. A 3rd layer has the same relation to the 2nd layer as the 2nd has to the 1st.

Each molecule is configured with information needed to run the simulation. Indices of molecule position within the island are used to select and consider a particular molecule within the island. An index for the island layer, and an index for the position within that layer as seen in Figure 4.9. Two quantities need to be considered to execute the simulation.

- A physical coordinate of the molecule in X and Y to generate a visual plot of the molecule at the simulation output.
- The indices of the twelve nearest neighbours of the molecule.

To calculate these quantities, the number of molecules across the side of the island is initially defined by the user, as well as the number of layers. The

island is generated as a square, and must be an even number of molecules across. The number of layers does not have to be an even number unless it is a bulk simulation and periodic boundary conditions are applied in 3D and not just in 2D.

Finding the nearest neighbours is made more complicated by the periodic boundary conditions as well as the hexagonal nature of the island. However, by iterating through the molecule indices, and tracking where the molecule is in the island as a function of its index, it is possible to use a complex series of logic statements to find the molecules nearest neighbours. Each molecule is assigned an X and Y coordinate during this logical process by considering its 2D position within island. The Y coordinate is trivial to find as it is simply assigned as the row number within the island, however the X is slightly more complicated due to the alternating nature of the row positions as seen in Figure 4.9.

4.3.2 Configuring the Monte Carlo Simulation

The starting state of the island is with all molecules orientated randomly. The Monte Carlo algorithm uses the energy landscape for a molecule defined by the orientations of its surrounding molecules and a surface interaction. This landscape is a table of all the possible orientations the molecule could take, and the energy it would be at if it took that orientation. The energy E_i, for each molecular configuration i is calculated by summing all the pairwise interactions with adjacent molecules, and a surface interaction, E_{SI}. A constant, α, is used to vary the strength of the surface interaction relative to the intermolecular interactions. As the surface interaction is artificial in form, it is necessary to manually calibrate it against intermolecular interactions. A low value of α means intermolecular interactions dominate the simulation dynamics, whereas a high value reverses this. Each intermolecular interaction is prefaced by a vacancy multiplier.

If an adjacent molecule has been assigned as a vacancy, the energy of that interaction is set to zero.

For the simpler case of a monolayer, the energy landscape for the current molecule being observed is calculated as follows:

$$E_i = V_{TL}E_{TL}(O_{BR}) + V_{TR}E_{TR}(O_{BL}) + V_R E_R(O_L) + V_{BR}E_{BR}(O_{TL}) + V_{BL}E_{BL}(O_{TR}) + V_L E_L(O_R) + \alpha E_{SI} \quad (4.3)$$

An adjacent molecule to the current molecules top left(TL), bottom right (BR) etc. will have an orientation O. The $E_{TL,TR,R...}(O_{BR,BL,L...})$ element is a table of the energy states presented to a side of the current molecule by the opposite side of an adjacent molecule. Each cell of the table contains the energy value of interaction for a unique orientation of the current molecule being observed. The vacancy multiplier ($V_{TL,TR..}$) will either be 1 or 0 depending on the vacancy status of the adjacent molecule.

A simple kinetic Monte Carlo algorithm is then implemented to choose the next orientation for the molecule. The C_{60} island is considered as a canonical ensemble, using a Boltzmann distribution to model the final state probability, so that:

$$P_i = Z^{-1} \exp\left(\frac{-E_i}{T}\right) \quad (4.4)$$

Here P_i is the probability of the molecule taking the i^{th} orientation, E_i is the energy of that orientation, T is the temperature in energy units and Z is defined as:

$$Z = \sum_i \exp\left(\frac{-E_i}{T}\right) \quad (4.5)$$

Due to the method of its calculation, the magnitude of E_i is arbitrary. It is a relative energy that is self-consistent. Thus the temperature, T, is set at an arbitrary magnitude to display the dynamics of the system. Once a

new molecular orientation for the molecule has been chosen, it is rotated to that orientation, a new molecule is randomly chosen and the process is repeated. As the simulation progresses, the average energy of the island will fall until it equilibrates.

4.3.3 Simulation Metrics and Parameters

A number of simulation metrics and parameters can be observed and set to control and observe the ordering in the island. As E_i is generated using Hückel Theory, the actual value for the interaction energy is not known. Thus the temperature T is set at an arbitrary magnitude to display the dynamics of the system. As such, no Boltzmann constant is included in Equations 4.4 and 4.5 as its inclusion would still not result in T representing the real temperature of the system. This is to say, a low temperature is set such that a molecule will almost certainly go to its lowest energy state. A medium temperature is such that a molecule has a range of discrete orientations available that it could move to. A high temperature is seen as the molecules having no bias towards any particular orientation. This is shown in Figure 5.2.

Island equilibrium is defined by the island energy minimising and remaining static for a period of time equivalent to 10× the timesteps taken to reach that minimum. The average energy of the island is defined as the sum of all the intermolecular and surface interaction energies, divided by the total number of intermolecular interactions and surface interactions.

The Shannon entropy

$$S = -\sum_i n_i \log_2(n_i) \tag{4.6}$$

where n_i is the fraction of molecules in a particular orientation i, is used as a measure of the number of molecules in different orientations.

Even though the lookup table is 7GB, the simulation only needs to process small segments of it at a time and so the speed at which the energy equilibrates is very fast. When considering a monolayer of 100 molecules, the system will equilibrate in a simulation time of less than 15 seconds on a desktop PC.

4.3.4 Island Visualisation

An important part of the simulation is how the molecular orientation output is visualised, especially when it must be compared to STM data. As such, instead of visualising molecules as wire-frame models, a series of simulated STM images from each of the molecules are stitched together to generate a simulated island STM image. The simulated STM images are generated during the table generation process. The physical X and Y coordinate of each molecule facilitates the stitching together of the simulated STM images during the output stage of the simulation. This process can be completed during the simulation to get time-dependent information about how the simulation is progressing.

4.4 Conclusion

A large-scale Monte Carlo simulation of orientational ordering in C_{60} assemblies has been developed, which incorporated a number of new computational approaches. These included a novel use of the Hückel Method to calculate an intermolecular repulsive term, in addition to utilizing the C_{60} molecular symmetry to reduce computation time. Using these tools, a lookup table of pairwise intermolecular interactions was generated for a high number of relative molecular orientations. A surface interaction was also included to mimic a Cu(111)/C_{60} and Au(111)/C_{60} interaction. This table of interactions was then applied to a Monte Carlo simulation to model

C_{60} assemblies. The intermolecular potential was validated by comparison against other theoretical methods, DFT and a Lennard-Jones potential. In the following chapter, outputs from the simulation described in this chapter are compared extensively to experimentally observed molecular systems.

Chapter 5

Applications of Monte Carlo C_{60} Simulation

5.1 Introduction

In this chapter, the simulation developed in the previous chapter is applied to a variety of different molecular configuration. Some of these have been examined by ourselves directly via STM, other simulations relate to studies of C_{60} in the literature, and yet other applications examine as of yet unstudied aspects of C_{60} islands. This chapter is broken up into a number of sections relating to the different molecular configurations studied. These start off with further validating the model on simple molecular monolayers a surface interaction, on a number of substrates. Secondly, molecular multilayers on surfaces will be studied where complex, long-range order is observed. Thirdly, bulk C_{60} is studied with a focus on a temperature and intermolecular separation dependent phase transition. Finally, vacancies are applied to these molecular configurations to observe the effects of island structure to order, and the effects of vacancies in bulk.

5.2 Experimental Methods

We have investigated two key systems, C_{60}/Cu(111) and C_{60}/NaCl/Cu(111) as examples of strong and weak molecule-substrate interactions respectively. To acquire high quality images of C_{60} islands, we used a commercial (Createc) UHV, low-temperature STM/atomic force microscope(AFM) system as described in Chapter 2. This provides images with sub-molecular resolution, which is a prerequisite for the analysis of the orientation of the adsorbed C_{60} molecules. The Cu(111) substrate was prepared via cycles of sputtering and annealing. C_{60} was also deposited onto a NaCl film prepared by depositing salt via a Knudsen cell onto a clean Cu(111) substrate (while the NaCl/Cu(111) sample was at room temperature). For both substrates, molecules were then deposited with the substrate cooled to 77K. For isolated molecules to be observed on NaCl, the substrate was cooled

to 4K while depositing molecules. For imaging, the substrate was kept at either 4K or 77K. At both of these temperatures, all molecular rotations are frozen out.

5.3 Monolayer Simulations

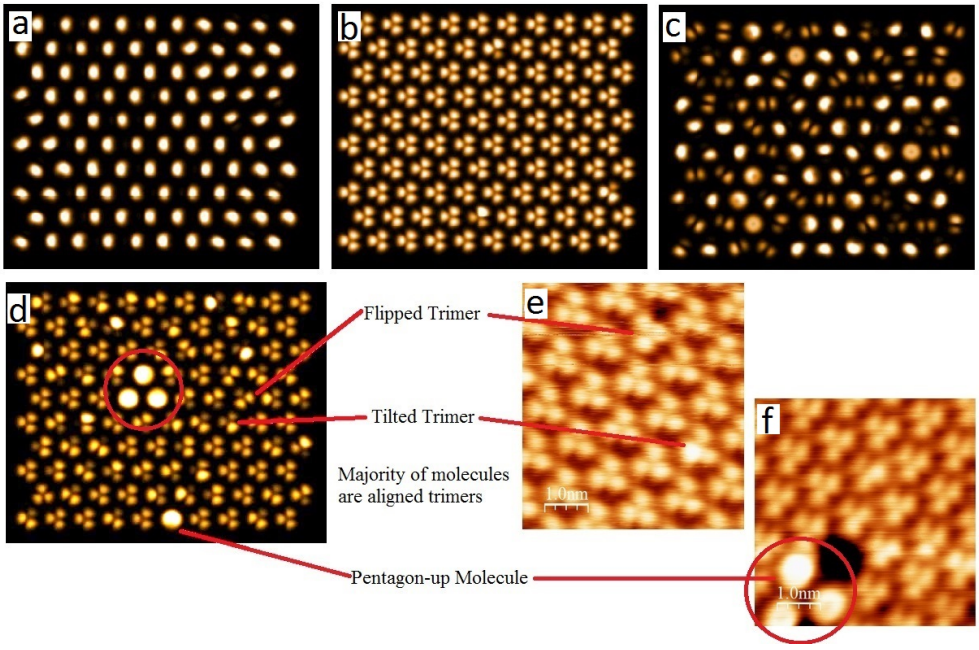

Figure 5.1: A series of 10×10 monolayer simulations. a)No surface interaction has been included here and the molecules are aligned single bond up. b-d) Varying simulation temperature with a strong Cu(111) surface interaction included, where (b) is a low temperature simulation where all molecules align perfectly. c) A high temperature simulation showing a fully disordered layer. d, e, f) A mid temperature simulation is compared to two experimental STM images and similar features identified. An experimental and simulated cluster of pentagon-down molecules are circled in d) and f). STM images taken at 4K.

Simulations were initially targeted at monolayer islands. The intermolecular separation (centre to centre) was set at 1.02nm to match experimental images. Modifying this intermolecular distance, however, did not affect simulation outcomes. Interaction tables were generated for sixteen intermolecular separations between 0.985nm and 1.055nm, and no significant changes in ordering were observed. Due to the speed at which monolayers equilibrated, a large 10×10 simulation size was selected. When no

surface interaction is included, the resultant molecules align single bond up, with hexagons aligning between neighbouring molecules. This is not realistic behaviour for adsorption on Cu(111) or Au(111), and thus shows that the surface interaction needs to be included (Figure 5.1a). When a surface interaction is included as discussed previously in Section 4.2.3, the resulting simulated order correlates well with STM data for both Cu(111) and Au(111). This confirms that the observed hexagon-prone orientation of the molecules is driven by the substrate bonding, and shows that intermolecular interactions assist in determining orientation with respect to rotation around an axis perpendicular to the substrate.

Additionally, as seen in Figure 5.1, an increase in temperature leads to increased island disorder. This was studied in more detail by examining the energy landscape of the island molecules in Figure 5.2. Higher temperatures produced previously unfavourable molecular configurations.

5.3.1 Cu(111) monolayers

By including a strong surface interaction, we simulate a Cu(111) substrate. The simulated islands display many features observed in STM images of actual islands. Similar features are compared in Figure 5.1 and include a long-range ordered structure (aligned hexagon-down molecules - seen as trimers), isolated or clustered pentagon-down molecules (seen as disk shaped molecules), flipped hexagon-down molecules that are reversed to the normal orientation, and finally tilted hexagons/pentagons which can be seen as molecules where one side is notably brighter than the other.

It is important to note in Figure 5.1 that for medium temperatures a molecule observed in a pentagon-down or flipped-trimer configuration is in a local minimum (see Figure 5.2(b)). This means that the next time the molecule is considered by the Monte Carlo algorithm, it may move to a different energy minimum. Experimentally, pentagon-down and tilted

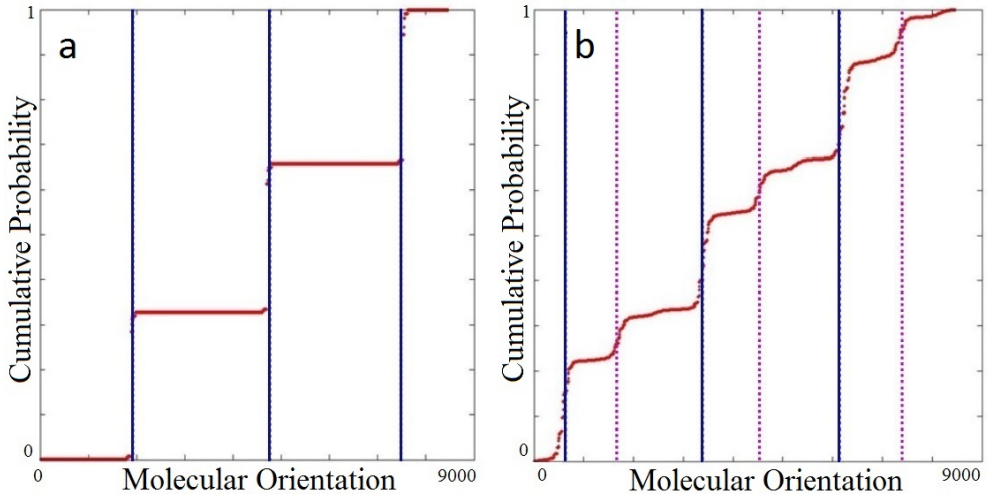

Figure 5.2: Cumulative probability distribution for a single molecule generated from the energy landscape it experiences. Its energy landscape is defined by its surrounding molecules. The x axis relates to all 8460 unique orientations the molecule can hold.
a)At low temperatures, three orientations are likely relating to three equivalent 120° rotations around a hexagon-down configuration in a C_{60}/Cu(111) island. These orientations are highlighted by the vertical lines in the figure. b) At high temperatures other orientations become more likely and can be seen as additional features in the graph. Here a molecule sits at the interface between two phases of hexagon-down C_{60} molecules. Each phase contains molecules in one of the preferential binding orientations for C_{60} on Cu(111) (at 180° from each other). This can be seen in b) as it is favourable for the molecule to be in either threefold symmetry orientation designated by the solid and dashed lines.

pentagon-down molecules are rarely seen. When they are observed, they will either be isolated or form small clusters, as seen by the three pentagon-down molecules in Figure 5.1f and Figure 3.2c. This clustering of pentagon-down and tilted pentagon-down molecules is routinely seen in simulation whereby these molecular orientations are observed as more stable when clustered (Figure 5.1(d)). For a simulation where the effective temperature is in the middle of the range we have investigated, these pentagon-down molecules etc. fluctuate around the surface. These time-dependent fluctuations are not observed in the STM images as they show molecules which have been rapidly cooled and had these fluctuations frozen in.

5.3.2 Au(111) monolayers

C_{60} molecules are not so strongly bound to an Au(111) substrate as compared to a Cu(111) substrate. This typically manifests as a higher proportion of molecules showing a pentagon-up, or similar non-uniform, orientation. It is easier for the molecules to rotate away from the low-energy, hexagon-up, orientation. The resultant surface can be a short-range ordered $(2\sqrt{3} \times 2\sqrt{3})R30°$ superstructure. A characteristic of C_{60}/Au(111) substrates involves boundary molecules separating two domains of hexagon-up molecules, each domain in one of the two C_{60} principal binding configurations. Here the two domains are separated by a boundary of pentagon-up molecules [36, 45].

In the simulations, by reducing the surface interaction compared to Cu(111), pentagon-up molecules are more commonly seen. As observed in experiment, the interface between two domains of C_{60} molecules is populated by tilted pentagon-up molecules (Figure 5.3). Initially, in simulation, most molecules adopt a tilted pentagon-up orientation. Then, as the energy minimises, domains of hexagon-up molecules start to nucleate, grow, and merge. As the simulation progresses, one of the domains will dominate. The other domain, surrounded by a barrier of pentagon-up molecules, will slowly be eroded and eventually disappear.

Higher temperatures led to an increased number of bright molecules within the final single domain of hexagon-prone molecules. Further increases in temperatures led to a series of smaller and unstable domains that would progressively nucleate and disperse. This inhibits the growth and domination of any one domain, resulting in a mosaic of the two domains. This is similar to observations by Paßens and Karthäuser [36], and is shown in Figure 5.4. In Figure 5.4A, it is unclear what exact orientation the bright molecules are adopting, or if another mechanism is contribut-

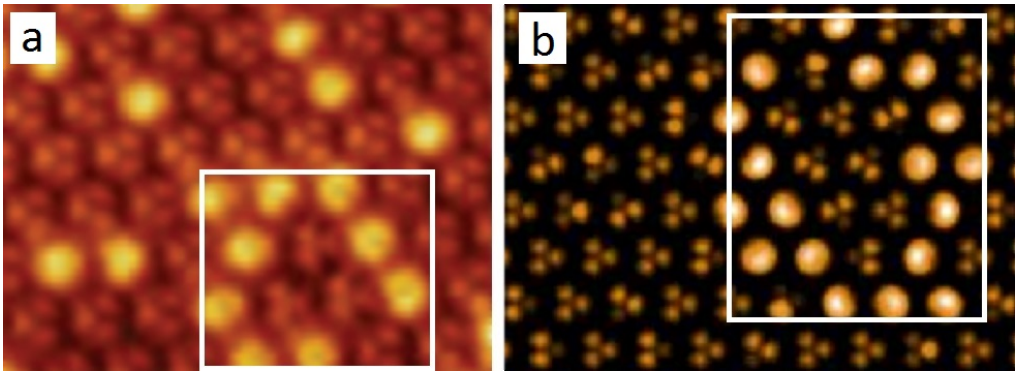

Figure 5.3: a) An STM image of a C_{60} monolayer on Au(111), reprinted with permission from Tang, L. et al. *J. Chem. Phys.* **2011**, *135*, 114702. Copyright 2011, AIP Publishing LLC. Circled is a cluster of molecules in the second principal binding configuration, surrounded by a wall of pentagon up molecules. b) A simulation with a reduced surface interaction showing two phases of C_{60} molecules and the boundary layer between them.

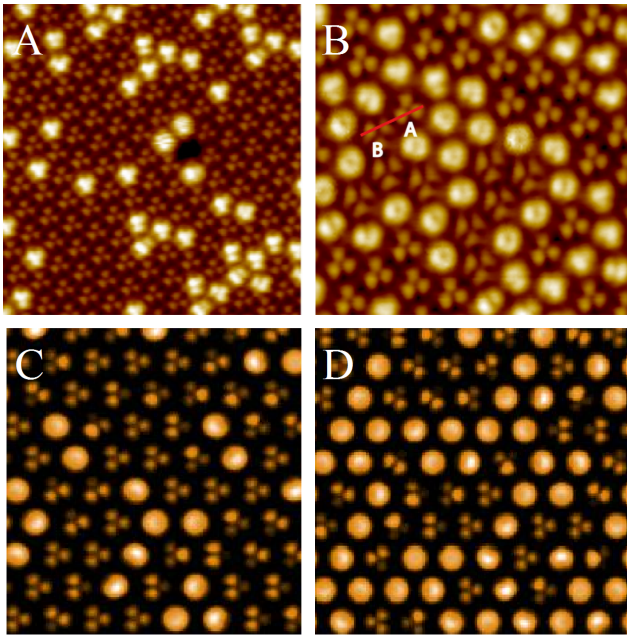

Figure 5.4: a-b) STM images reproduced from [36]. C_{60}/Au(111) surface. For a) molecules deposited on room temperature surface, for b), molecules deposited on surface at 170 ° C, then subsequently annealed to 210°C for 80 minutes. c-d) Monolayer simulation with surface interaction configured to model the Au(111) surface. At moderate temperatures (as in (c)), bright, tilted pentagon-down molecules develop within a single domain of hexagon-down molecules. d) At high temperature, an unstable set of domains fluctuate across the surface.

ing towards their brightness beyond their simple orientation. Nonetheless, there is a striking resemblance to the simulation output in Figure 5.4C. For higher temperatures, in Figure 5.4D, the unstable nature of the simulated structures indicates that rapid cooling must occur to freeze the structures

in place.

This simulation shows excellent agreement with monolayer C_{60} islands on multiple substrates. Different temperature levels mirror what is observed in actual STM images, and different surface interactions lead to expected rotational structures.

5.4 Multilayer Simulations

The simulation size for multilayers was kept at 8×8, with periodic boundary conditions, which was considered to be a reasonable size to mitigate edge effects whilst keeping simulation time down. In an 8×8 simulation, a central molecule will have either 3 or 4 molecules between it and an edge.

A multi-layered simulation will not minimise its energy as easily as a monolayer due to the energy landscape being significantly more complex. As a multilayer simulation progresses, the molecules will go through a number of intermediate phases or reconstructions before equilibrating (Figure 5.5). These can act as local minima in which the simulation may get trapped. Because local minima are often long-range structures within the island, it can be difficult for the Monte Carlo algorithm to escape them. This is because only one molecule is considered at a time; its surrounding energy landscape remains static and so the local minima structure would remain. In real islands, all the molecules rotate simultaneously until a minimum is reached. Nevertheless, (2×2) superstructures have been simulated that closely resemble the C_{60} rotational reconstructions observed in [29], where a bilayer of C_{60} molecules on NaCl exhibited rotational order (Figure 5.6). Here no surface interaction is included due to molecular decoupling at the C_{60}/NaCl interface [48, 49]. Experimentally and in simulation, there are dissimilarities to the more common (2×2) configuration observed in Figure 4.1a and bulk C_{60}. Here, double-bond-up molecules are

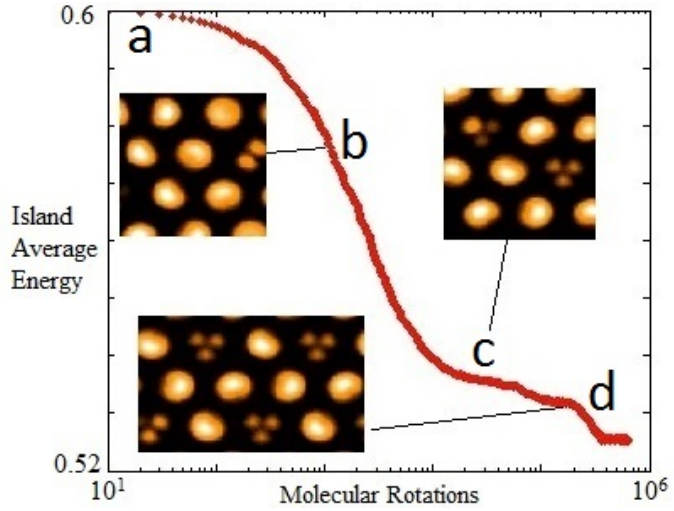

Figure 5.5: The average island energy as a function of the number of molecular rotations (i.e. time). a) The starting, high-energy configuration. Molecular orientations are random at the start of the simulation. b) Molecules quickly align themselves approximately pentagon-down, single-bond-down and atom-down. c) Different (2×2) domains form, these are separated by antiphase boundaries and 'compete' in terms of the expansion of a given phase. d) One (2×2) domain dominates. Once a sufficient number of molecules are in that domain, a critical point is reached which triggers the conversion of all molecules to that (2×2) domain.

replaced by tilted pentagon-up molecules.

A quad layer has also been simulated atop a Cu(111) substrate. This has demonstrated how a (2×2) superstructure similar to bulk C_{60} can develop from a layer of molecules that are influenced by a surface interaction. If intermolecular interactions between the bottom layer and second layer in the island are left as normal, the molecules in the bottom layer will reconstruct to a (2×2) superstructure. Here all the molecules remain hexagon-prone due to the surface interaction, but 25% of molecules have a 60° rotation around an axis perpendicular to the surface. In this case, the bulk-like reconstruction will develop immediately from the second layer upwards. Due to the binding configurations of C_{60} on Cu(111), however, this might not be physical. Thus, the interaction of the second layer affecting the bottom layer is reduced so as to maintain the (1×1) structure seen in monolayers. This is the case seen in Figure 5.7. Here a bulk-like reconstruction was achieved in simulation via a boundary layer between bottom layer

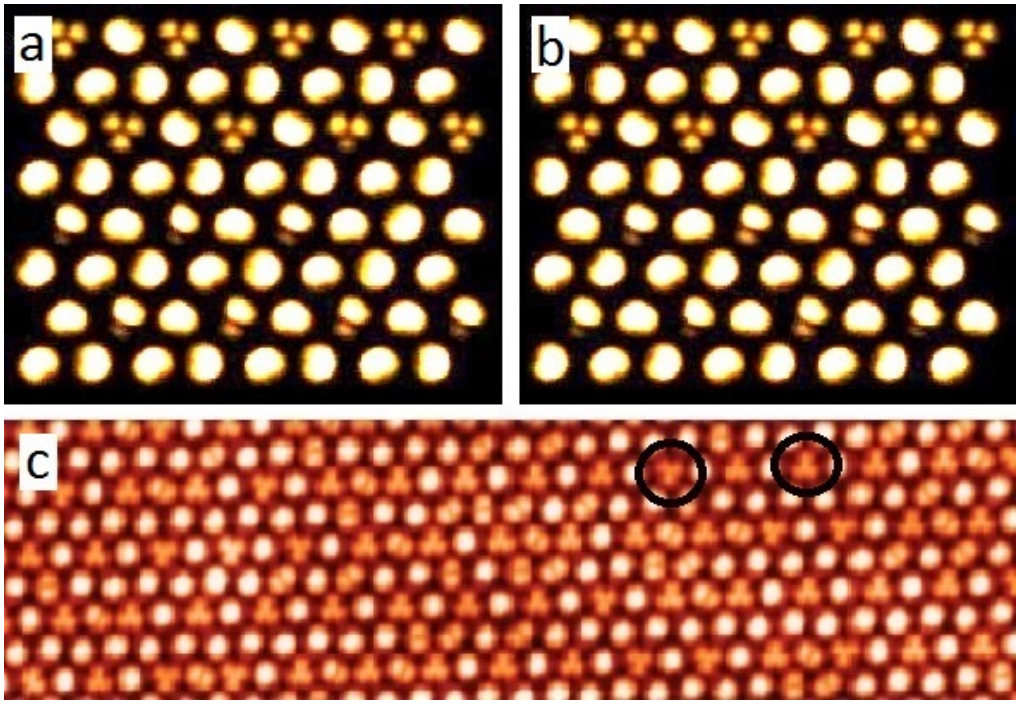

Figure 5.6: A bilayer island simulation with an intermolecular separation of 1.05nm, where a) is the bottom and b) top layer in the island. The bottom layer a) has no surface interaction included. In a) and b) the top half of the simulation is similar to c), whereby hexagon-up molecules are surrounded by tilted pentagon-up molecules. The bottom half demonstrates a non-physical local minima that the simulation has been trapped in. c) STM image of bilayer C_{60} on NaCl/Au(111), reprinted with permission from Rossel, F. et al. *Phys. Rev. B* **2011**, *84*, 075426. Copyright 2011 by the American Physical Society. Intermolecular separation is measured at 1.05±0.05nm. A (2×2) superstructure has developed which is similar to that seen in (a-b). Note circled C_{60} molecules are oriented 180° to each other. This behaviour can sometimes be observed in simulations before the system energy has been minimised.

(hexagon-down (1×1) reconstruction) and third layer ((2×2) reconstruction). This boundary layer exhibits a tilted double bond (or atom-down) configuration in a (2×1) superstructure.

It was noted that the (2×2) structure shown in Figure 5.7c-d develops much more readily if the island is three or more layers thick. For the structure to develop, it will initially nucleate in the central layers and then spread throughout the rest of the island. Thus this structure will only occasionally appear in simulated bilayer islands, but will almost always appear in islands having three or more layers. Additionally, the (2×2) structure is observed to be more stable in the central layers. Layers that have a sur-

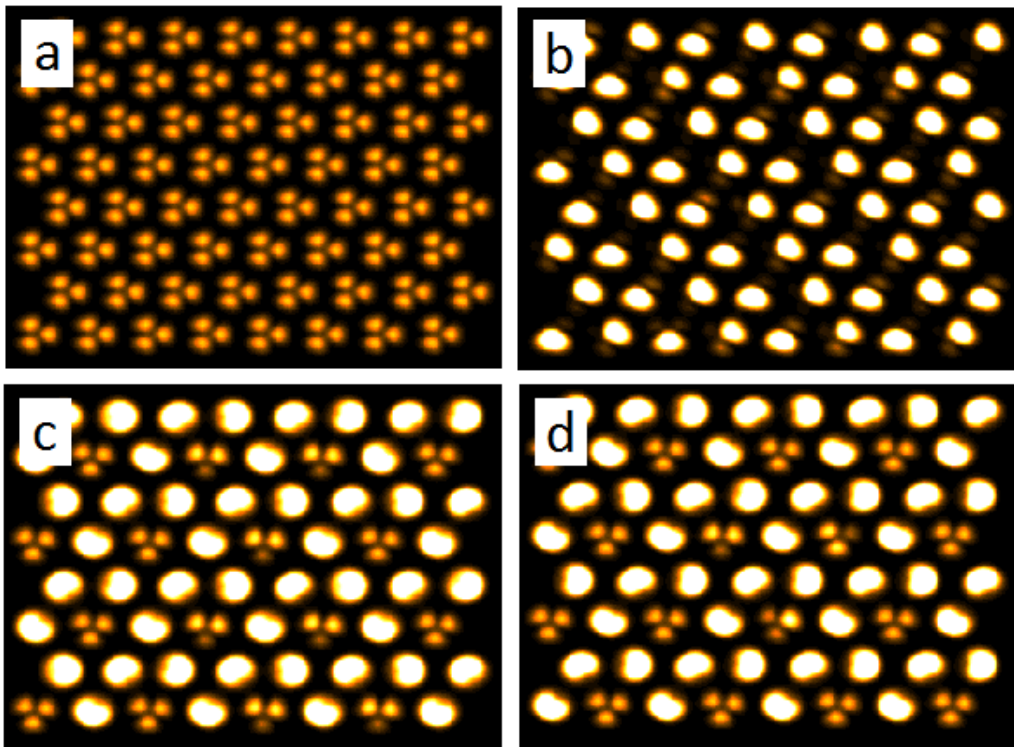

Figure 5.7: A four-layer island where (a) – (d) represent the lowest to highest layers respectively. The first layer a) has a surface interaction included and a reduced interaction with the layer above to simulate a Cu(111) substrate. By the third layer c), a (2×2) superstructure has developed. An intermediate reconstruction has developed in b) to bridge the rigid (1×1) structure forced by the surface and the more favourable (2×2) phase. The intermediate reconstruction exhibits tilted double-bond-prone molecules.

face exposed are less stable. This is especially the case for hexagon-down molecules. This corroborates experimental results where surface molecular rotational disorder is enhanced on the surface of the molecular layer [50]. Additionally, this supports Laforge et. al's prediction that the surface hexagon-down molecule is in a shallower energy well than the other three molecules in the unit cell.

5.5 Bulk Simulations

A well-known feature of bulk C_{60} crystals is the variation in rotational order that occurs as a function of temperature. A strong phase transition has been observed [51] where at a particular transition temperature, molecular rotations are frozen out. This coincides with the cage of the bulk C_{60} having

its lattice constant reduced significantly. This is shown in Figure 5.8.

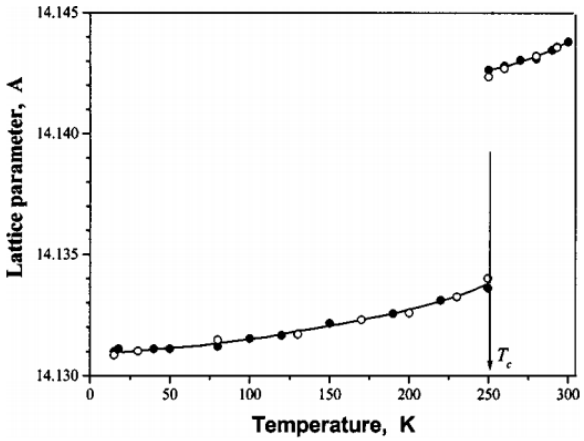

Figure 5.8: Reproduced from [51], XRD data of C_{60} lattice parameter modification via temperature. Note large jump at 250K indicating the critical temperature.

A number of smaller phase transitions were additionally observed that related to surface molecular disorder. These have not been considered. Here we consider a series of bulk simulations with 3D periodic boundary conditions, where we observe the effects of sweeping the temperature and intermolecular spacing. In this set of simulations, extended Hückel theory was used to generate the interaction tables. Even though this resulted in significantly longer table generation times, it was deemed necessary so as to include short ranged σ orbitals. This to more precisely model the pairwise intermolecular interactions when the intermolecular separation was significantly reduced.

5.5.1 Varying Temperature

As the temperature was swept, for a single intermolecular spacing, a critical point was observed where the orientational order of the bulk assembly would rapidly drop. This can be observed in Figures 5.9 and 5.10.

This clearly mirrors what is observed in by Katz et. al. [51] and Laforge et. al. [44], and shows that the model follows the expected convention. As

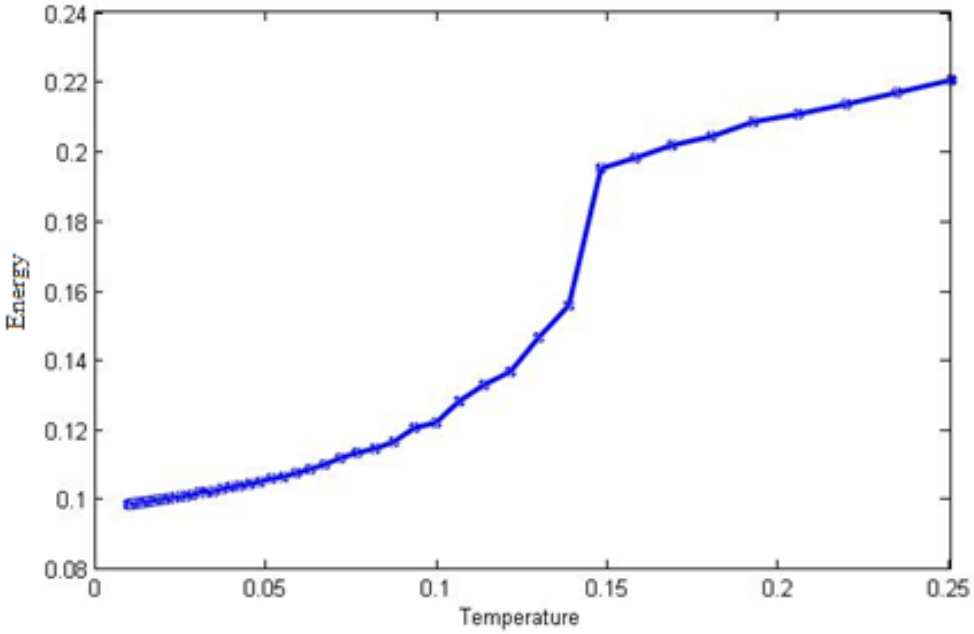

Figure 5.9: A plot of the energy against temperature of an $8 \times 8 \times 8$ simulation. The simulation clearly reaches a critical point at which the energy jumps as a result of temperature. The energy jump indicates a large drop in molecular order.

the temperature increases, the molecules have more energy to overcome limiting energy barriers. At some critical temperature, these barriers become insufficient and the molecules quickly are able to rotate freely and break the (2×2) ordering. Note that after the critical temperature is reached, the energy continues to rise. This is because even though the low-energy (2×2) order is lost, there still exist energetic configurations that are more unfavourable. As the temperature continues to increase beyond the critical point, these become available.

5.5.2 Varying Temperature and Intermolecular Separation

Simulation Configuration

Our key aim in this component of the research was to explore the parameter space between temperature and intermolecular spacing. As such, a range of temperatures and intermolecular spacings were chosen. For each

simulation configuration of temperature and intermolecular spacing, the simulation was run for a very large number of time steps until it had equilibrated. The energy and entropy of the simulation were then recorded and a new simulation configuration initialised by resetting the molecules to their original position. The simulation was started with all molecules in an ordered (2×2) configuration. This to prevent the simulation becoming stuck in a local minima configuration that would skew results. The molecular positions were reset after each change in temperature to ensure that no fortuitous event at one temperature, leading to long-range order or disorder, could affect future temperature measurements.

The process of varying intermolecular spacing is relatively time consum-

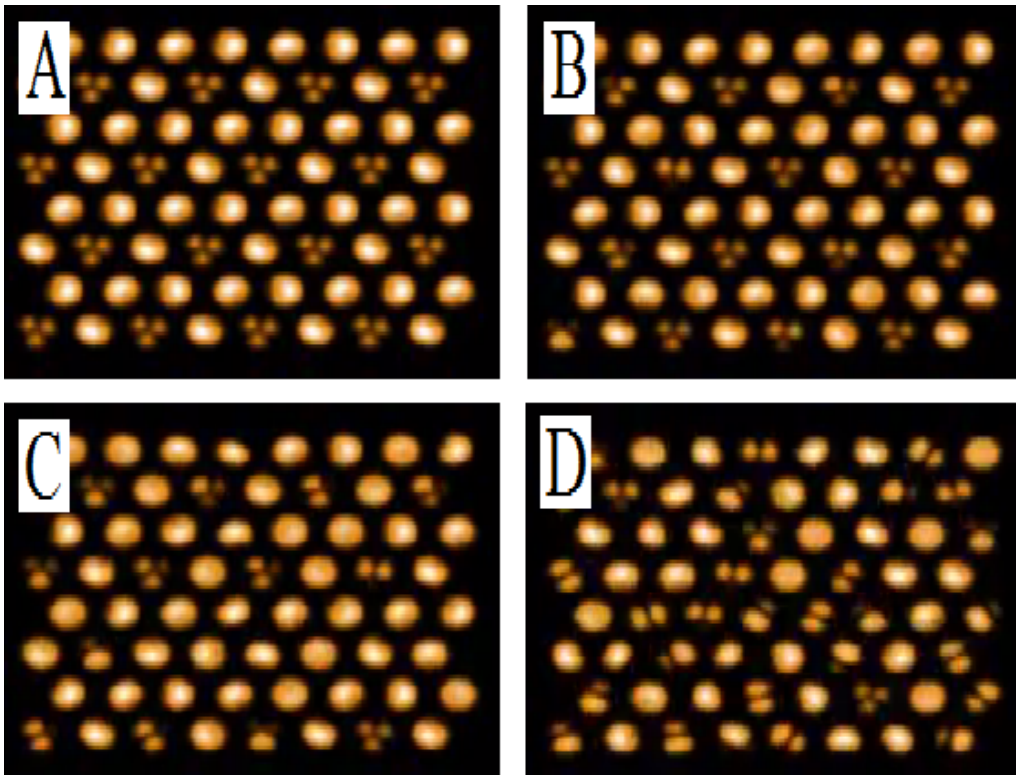

Figure 5.10: The fourth layer of an $8 \times 8 \times 8$ simulation as a function of effective temperature in the Monte Carlo simulation. A) A low temperature configuration where all the molecules are well ordered. B) As the temperature rises, all molecules remain in the (2×2) orientational order. Hexagon-up molecules, however, are observed to be slightly disordered and occasionally tilted. C) The critical temperature is reached. Many molecules are still in the (2×2) configuration, but disorder is rapidly taking hold in the island. D) Beyond the critical temperature, high levels of disorder are observed.

ing. A new interaction table must be generated for each intermolecular-spacing configuration. Additionally, consideration must be given to how the interaction tables are normalised. Smaller intermolecular spacings will exhibit higher energies due to the higher overlaps between the molecular orbitals. If all the varied intermolecular spacings are normalised as usual, this aspect is lost. Therefore, it is important to ensure normalisation between all the different interaction tables are consistent. We do this by normalising them by the normalisation factor generated from the interaction table with the closest intermolecular spacing. This table is chosen as it exhibits the highest energy configuration. The shapes of the orbitals at different intermolecular spacings, not just the strengths, affect the temperature-dependent order. As such, a normalisation strategy in which each interaction table was self-normalised was additionally implemented.

Results

Figures 5.11 and 5.12 show the energy and entropy respectively of a large-scale simulation as a function of intermolecular spacing and temperature. Here the interaction tables for the different intermolecular spacings have been normalised to the interaction table with the minimum intermolecular spacing.

A number of features become immediately apparent. Firstly, there is seen to be a dramatic difference in graph shape between the energy and entropy in Figures 5.11 and 5.12. This is readily explained by considering the kinetics and dynamics of molecular motion. As the temperature increases, the molecules start to vibrationally fluctuate away from their lowest temperature state, whilst still remaining in their energy well (Figure 5.10B). Due to the high number of available molecular orientations in the simulation, there are a large number of ways a molecule could do this. As the entropy is calculated by considering the states of all the molecules,

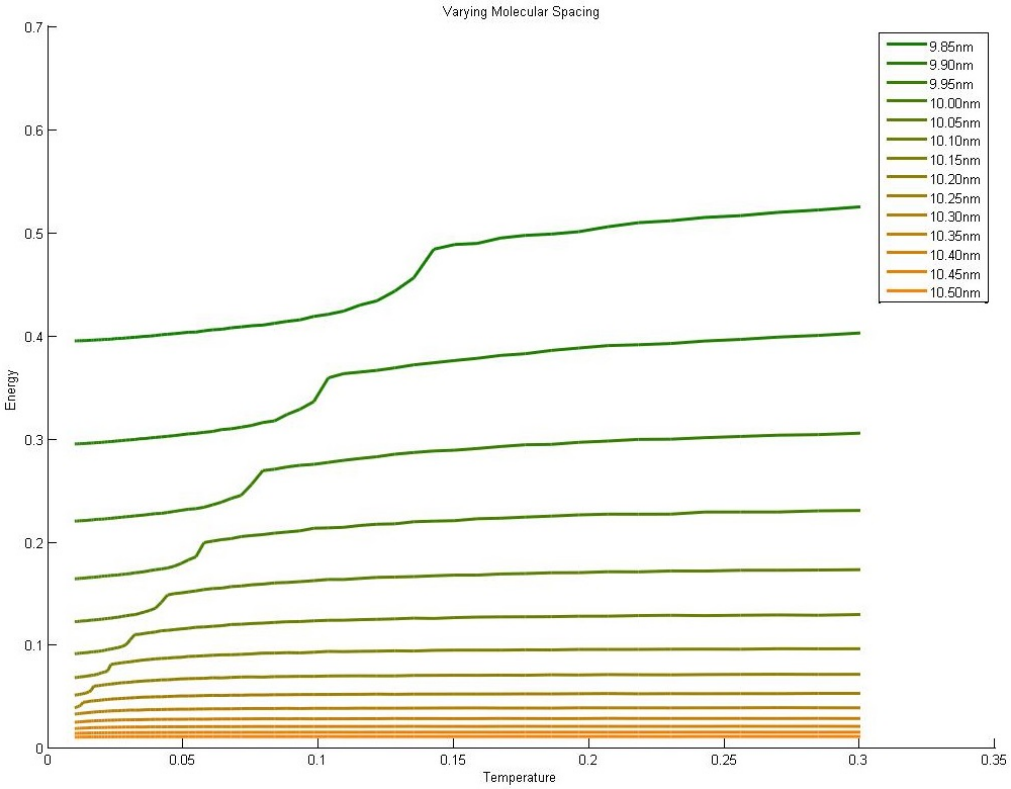

Figure 5.11: The bulk energy from sweeping the temperature, for a number of intermolecular separations.

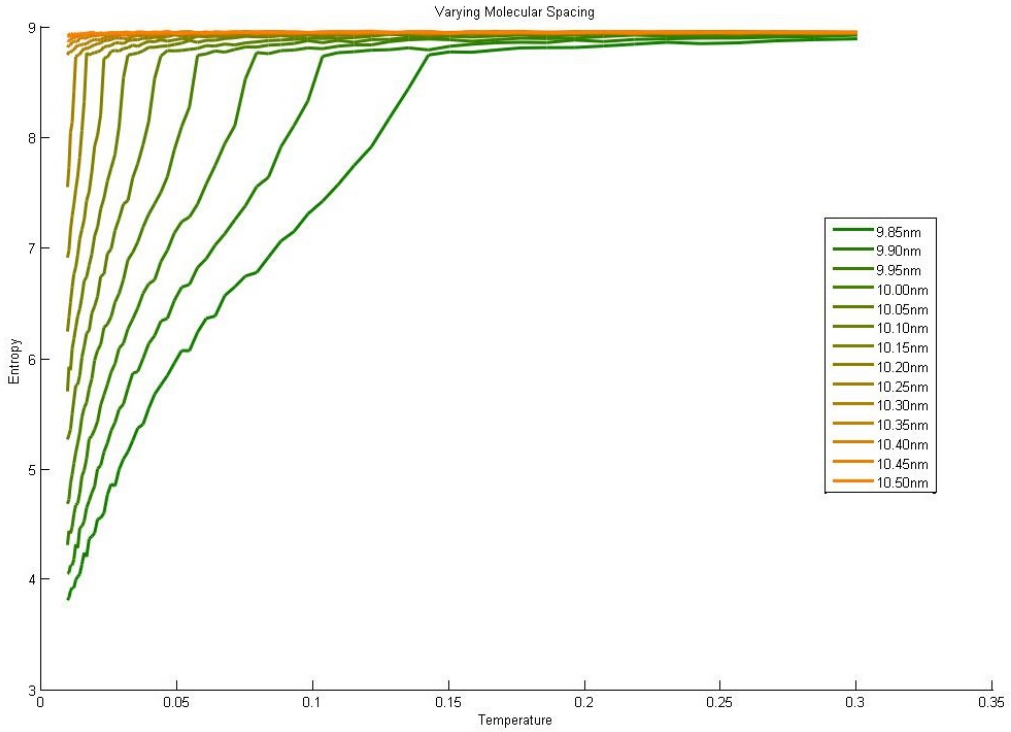

Figure 5.12: The bulk entropy from sweeping the temperature, for a number of intermolecular separations.

this constitutes a large rise in entropy. When observing the energy, these wobbles are still well within the local energy well, and as such, the energy of the island is not significantly changed. As such, while the entropy is interesting to observe, the energy is actually a better measure of the bulk orientational order of the C_{60} assembly. Interestingly, the critical point is still visible in the entropy traces, but unlike the energy, once the critical point has been reached, the entropy is almost at a state of complete disorder. There is still a rise in the entropy after the critical point, but it is much reduced compared to the energy.

Secondly, as the intermolecular spacing is increased, the energy of the simulation is generally reduced. This is to be expected due to the normalisation process used here. Moreover, the critical point temperature is greatly reduced. As the molecules are moved apart, the energy barriers to free molecular rotation are reduced due to the orbital decay. This leads to the earlier onset of disorder.

The second bulk simulation method is where interaction tables for the various intermolecular spacings have been normalised to themselves. Figures 5.13 and 5.14 show the energy and entropy respectively of this simulation.

Under these conditions, a number of unusual features are observed in the simulations. As the intermolecular spacing is increased, the critical temperature for disorder is reduced. This could be explained by the functional form of the π orbitals that make up the C_{60} molecule. As the distance from the molecular framework increases, these become broader and more diffuse. This would lead to shallower energy barriers to molecular rotation and as such, would allow the onset of disorder faster. This shift in critical point is observed in both the energy and entropy.

Secondly, in the energy graph, as the intermolecular separation is increased, the energy for that given temperature is also increased by a con-

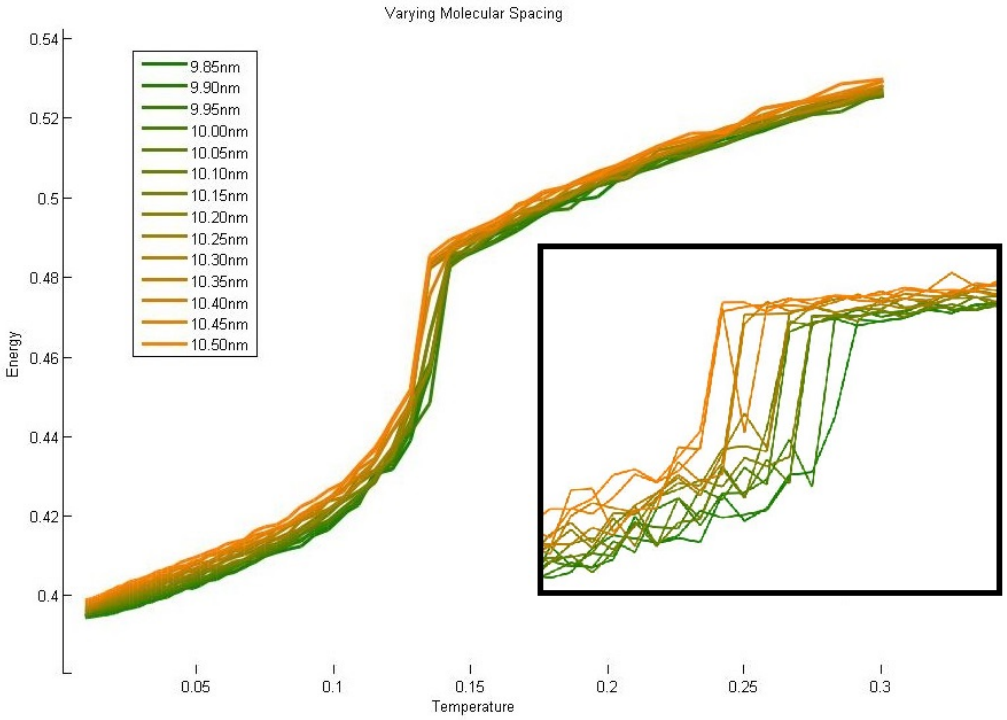

Figure 5.13: The bulk energy of the C_{60} assembly as a function of temperature, for a number of intermolecular separations. The insert is a separate simulation run with a finer resolution between the temperatures. In the large-scale run the critical point was spread across a single temperature point. Even in the inset though, there is still some aliasing but the trend of the critical point is clearer.

sistent offset. The higher intermolecular separations are shifted to higher energies. This implies that at higher molecular separations, the energy wells that the molecules sit in are not as deep, such that they are kept at a higher energy across the whole range in temperatures. This however contrasts with the entropy graph, where there is no such offset. Instead, at low temperatures, the higher intermolecular separations have significantly lower entropy. At higher temperatures, this difference quickly disappears. This is confusing as it indicates that even though the energy well is shallower for higher separations, and as such the critical disorder temperature is reduced, the entropy is still lower at reduced temperatures. It is possible that due to the smaller intermolecular separations, additional, small scale corrugation in the intermolecular potential could be generated due to σ orbitals included by extended Hückel theory. If the energies of these wells are equivalent, this could lead to higher disorder whilst not altering the

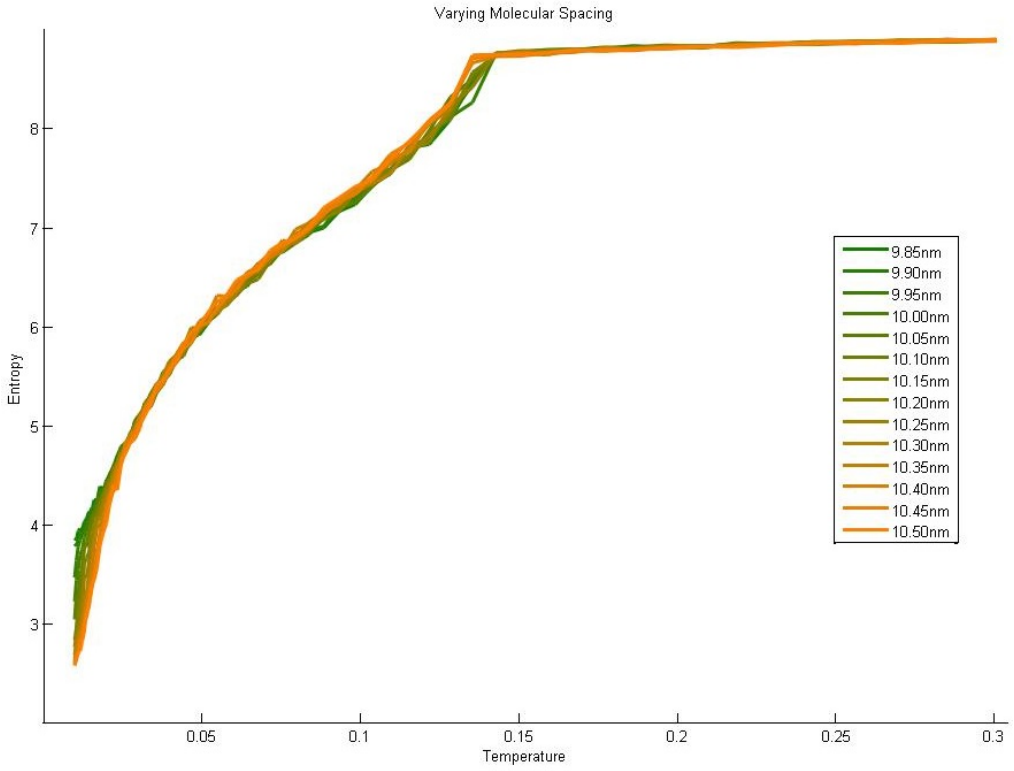

Figure 5.14: The bulk entropy from sweeping the temperature, for a number of intermolecular separations.

total simulation energy. At higher energies these small corrugations in the potential would quickly lose influence.

5.6 Vacancies in Monolayer, Multilayer, and Bulk C_{60}

The inclusion of vacancies allows for new investigations into C_{60} molecular ordering. In monolayers and multilayers, large numbers of vacancies were included to create shaped islands with non-periodic boundary conditions. For the bulk crystal, vacancies were included in order to study their role as potential nucleation points for order or disorder in the 2×2 reconstruction.

5.6.1 Vacancies in Monolayer C_{60} Islands

Vacancies were selectively added to a monolayer to create a bounded molecular island, as seen in Figure 5.15. A number of differences as compared to the vacancy-free assemblies quickly become apparent. It was noted that the edges of the island became 'seeding' sites for molecular order. By using a low surface-interaction, a simulation with periodic boundary conditions would only produce rare and isolated hexagon-prone molecules. By contrast, and using the same low surface-interaction, the shaped island would produce significant numbers of hexagon-prone molecules along the island edge. These would then 'seed' a spread of hexagon prone molecules over the entire island. This process is shown in figure 5.15. This is consistent across various temperatures.

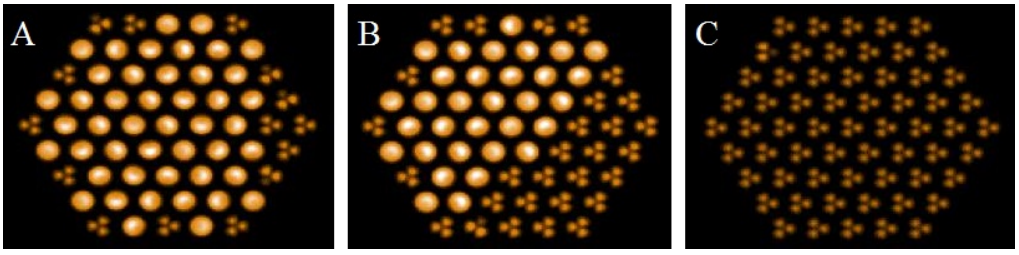

Figure 5.15: A) The initial stages of a simulated C_{60} island, with a low surface-interaction included. Note the hexagon molecules are spread in the beginnings of what could be a 2×2 reconstruction. B) As the simulation progresses, a phase of hexagon-prone molecules spreads from the edges of the island. C) Finally, the entire island is hexagon prone.

At slightly higher temperatures, significant disorder is present in the rotational phase of the C_{60} hexagon-prone molecules in a similar fashion to Figure 5.4d. Figure 5.16 shows a mosaic of the two phases across the simulated island. This kind of orientational instability was only observed in defect-free monolayers, with periodic boundary conditions, at much higher temperatures. This leads to the hypothesis that rotational instability induced by island boundaries led to the increased level of disorder. This effect is significant enough to propagate from the edges across the island. Notably, the experimental islands imaged by Paßens and Karthäuser[36]

were part of a larger monolayer, consisting of an unbroken layer of C_{60} molecules. As such, as well as the substrate temperature, surface structures such as step edges and defects could have contributed to the overall molecular disorder. This additionally could mean that smaller islands of molecules have increased levels of rotational instability at higher temperatures. Future work could investigate the size of island as a function of rotational instability.

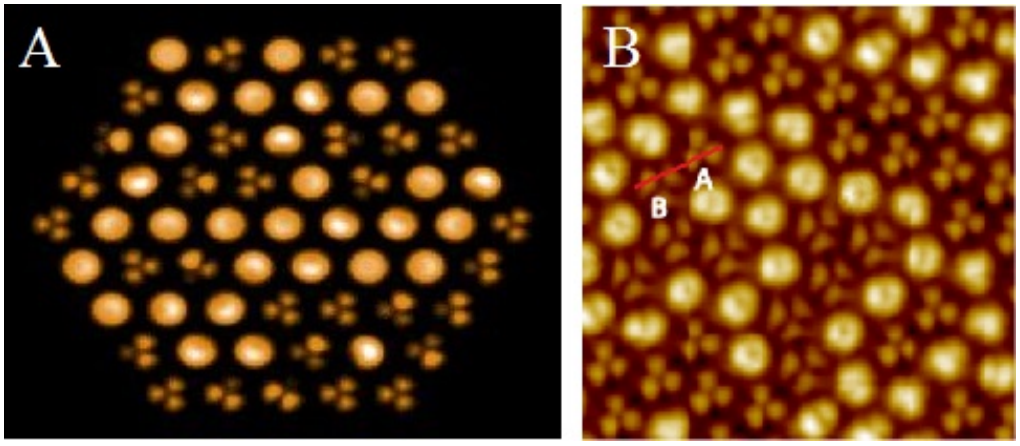

Figure 5.16: A) simulated C_{60} molecular island, at a high temperature. B) STM image of C_{60} molecules on Au(111), reproduced from [36].

5.6.2 Vacancies in C_{60} Multilayers and Bulk Crystals

Vacancies were created in a C_{60} bilayer to shape a two layered island. These vacancies were located across both layers. This did not produce any observed differences between an island with periodic boundary conditions. It is possible this is because edge-molecules have a larger number of neighbours compared to the monolayer case, due to the layer above, thus reducing their possible instability.

Vacancies were additionally inserted into bulk C_{60} simulations. Initially, a single vacancy was generated in an $8 \times 8 \times 8$ bulk simulation. This was run 500 times and the resultant order examined. It was hypothesised that from the 2×2 ordering, one molecule might become preferentially assigned to the vacancy. During the simulation, no such preference was observed.

The vacancy also did not act as a nucleation site for the 2×2 molecular ordering.

5.7 Conclusions

Our simulation strategy has successfully reproduced observed structures in mono- and multilayered C_{60} islands, as well as bulk C_{60}. These simulations have been facilitated by an extremely fast computation time. Cu(111)/monolayer C_{60} simulations show good agreement with experiment, including defects, clusters of pentagon-down molecules, and temperature dependent order. In multilayers, (2×2) structures have been reproduced similar to ones observed in a C_{60} bilayer on NaCl [29]. Additionally, with a surface interaction present, (2×2) structures have been observed developing in upper layers of a simulated island. These were facilitated by a boundary layer of molecules.

Bulk C_{60} was then simulated, to investigate the dependence on temperature and ordering. A critical temperature to disorder was observed as a function of intermolecular separation. Finally, vacancies were added to monolayers, multilayers and bulk simulations. In monolayers, at low temperatures, island edges were seen as nucleation points for hexagon-prone molecules, which could act as nucleation points for a total conversion of all molecules to a hexagon-prone orientation. At higher temperatures, orientational instability was observed that developed at the simulated island edges, and propagated to affect the whole island.

The previous chapter, and a number of results sections from this chapter have been published in [52]. Sections not published to date include all bulk simulations and vacancy simulations, as well as results shown in Figure 5.4.

Chapter 6

Probing the Electronic and Geometric Properties of K-Doped C_{60} Using Combined STM-AFM

6.0.1 Chapter Overview

In this chapter, results of an AFM and STM study on potassium doped C_{60}, on Cu(111) and Au(111) are presented. Single molecule doping was completed on the Cu(111) substrate, whereas K doped C_{60} monolayers were studied on the Au(111) substrate.

6.1 Introduction and Background

Doping is the process by which impurities are added to materials to modify their electronic properties. These impurities either add or remove electrons from the material, which modifies its electronic structure. This process is of significant interest in the scientific domain, and central to the semiconductor industry, due to the ability to tune the electronic properties of materials and devices.

The C_{60} molecule can experience significant modification of its electronic structure via the addition of alkali metal dopants. Additions of electrons from dopants can cause it to adopt a wide range of electronic properties. Upon K doping, electrons from the K 4s orbitals are transferred to the C_{60} LUMO [53], leading to a shift of the orbitals with respect to the Fermi level. Progressive doping fills up the LUMO. Each K dopant donates a particular amount of charge, depending on the local adsorption characteristics of the C_{60}.

Early experimental results [54] showed that potassium doping could radically alter the electronic properties of bulk C_{60} films. With progressive potassium doping, the molecular film was seen to transition from a semiconductor to a superconductor at low temperatures. This system subsequently received significant attention with a range of studies into different alkali metal dopants, with further investigations into structural and electronic changes. [55, 56, 57, 58, 53]. With progressive potassium doping,

multilayer K_nC_{60} structually transitions between body centred cubic (bcc) packing for $n < 4$, to body centred tetragonal (bct) for $n = 4$, to face centred cubic (fcc) for $n = 6$ [53].

Later alkali metal doping studies focused on C_{60} monolayer systems. The malleability of the C_{60} electronic structure, with the inclusion of dopants and a surface interaction, presented a complex and multi-faceted system to study [59, 60, 61]. STM provided particularly important insights due

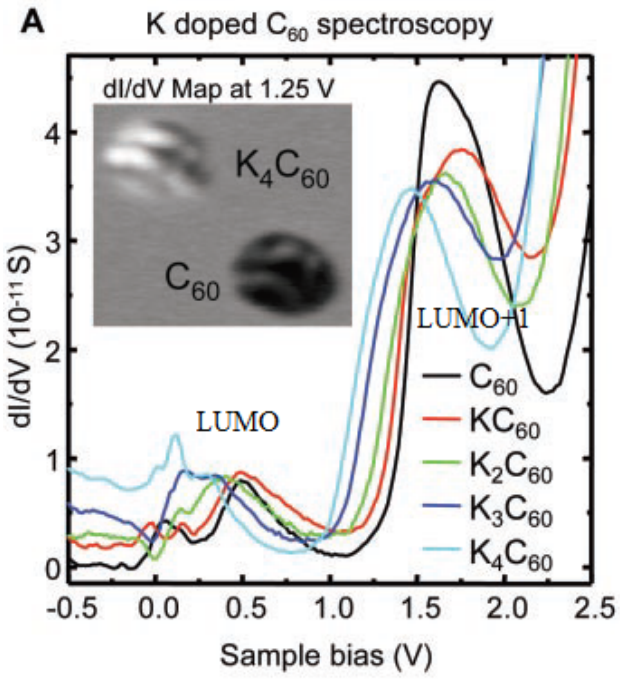

Figure 6.1: Reproduced from [4]. dI/dV measurements as a C_{60} molecule is progressively doped from K0 to K_4. Inset is a spatial map of the differential conductance at 1.25V.

to its combination of high spatial resolution and sensetivity to the local density of states. STM studies were conducted on potassium doped C_{60} [4, 62, 63, 64]. A particularly elegant study was carried out by Yamachika et. al. [4] by progressively doping an isolated C_{60} molecule. This by sequentially dragging it with an STM tip over multiple K atoms deposited nearby. Progressive modification of the C_{60} band structure was observed via differential conductance (dI/dV) measurements, as seen in Figure 6.1. Key features to note are the modification of the shape of the LUMO, and a

shifting of the LUMO+1 towards the Fermi level. Here it was determined that each K dopant contributed approximately 0.6 electrons to the LUMO, leading to the downward shift. Changes seen in the shape of the LUMO were not fully understood. K doped C_{60} monolayers and multilayers have

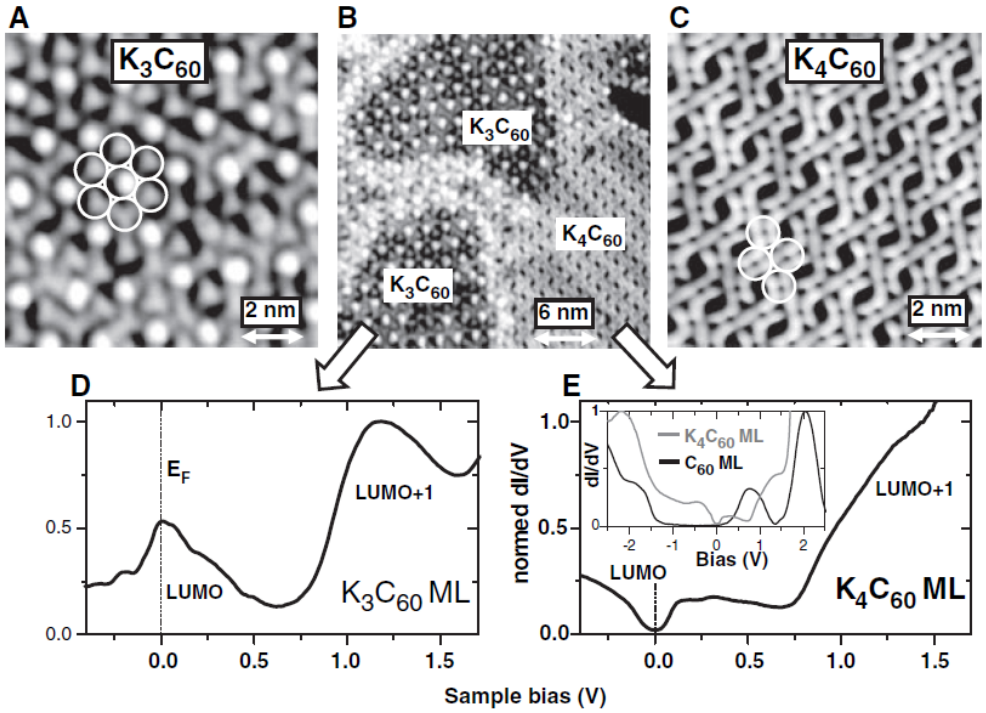

Figure 6.2: Reproduced from [62], potassium-doped C_{60} monolayers on Au(111), imaged and analysed using STM. A) shows the K_3C_{60} surface, B) shows a mixed phase between K_3C_{60} and K_4C_{60}, C) shows the K_4C_{60} surface. D-E show dI/dV measurements of these surfaces.

additionally been studied via STM. Here interesting surface reconstructions are observed for the n = 3 and 4 dopant levels. These are shown in Figure 6.2. The two striking points to note are that radical changes in surface geometry and band structure between K_3C_{60} and K_4C_{60}. At n = 3, the surface is metallic, with a large peak at the Fermi energy, at n = 4, the surface has transitioned to become a semiconductor, with a small band gap straddling the Fermi level. These geometric variations are thought to be due to Jahn-Teller distortions induced in the molecule as a result of the K doping. The electronic structure of the doped monolayer is substantially different from the single molecule. This is thought to be due to the different spatial

positions of the dopants. In the K_4C_{60}/Au(111) system, the C_{60} molecules are thought to sit double-bond upwards, with a long-range 2×2 order. In the K_3C_{60}/Au(111) system, both orientationally ordered and disordered islands are often observed via STM. Orientationally ordered configurations typically show a 2×2 configuration, with one bright molecule, and three dim molecules per unit cell. It is thought that the bright molecule might be as a result of a K induced surface reconstruction, rather than simply an effect of the molecular orientation.

This chapter is in two sections. Firstly, experimental results are examined where a single C_{60} molecule on Cu(111) is doped by dragging it over a series of potassium atoms adsorbed around it. This molecule is then studied via differential conductance and AFM measurements.

Secondly, experimental results are examined of K doped C_{60} monolayers on Au(111), in particular, AFM measurements of K_3C_{60}/Au(111) and K_4C_{60}/Au(111).

6.2 AFM Study of a Single K-Doped C_{60} Molecule on Cu(111)

6.2.1 Experimental Procedure

A pristine Cu(111) surface was prepared via repeated cycles of sputter/annealing. A fraction of a C_{60} monolayer was deposited onto the substrate, initially cooled to 5K, to achieve isolated molecules. This was completed via a two stage deposition process, whereby C_{60} is initially deposited from a quartz crucible wound by a tungsten heating element, onto a silicon wafer. This wafer is then advanced into the scan head and heated to desorb any C_{60} adsorbed on it. Successive depositions were completed until a sufficient coverage of C_{60} was present. A sub-monolayer of K was deposited directly

onto the sample cooled to 5K inside the scan head. This was completed via a calibrated potassium source, manufactured by SAES getters. The potassium coverage was checked via STM, and progressive depositions of K were completed until a sufficient coverage was achieved. STM images of the final prepared surface are shown in Figure 6.3.

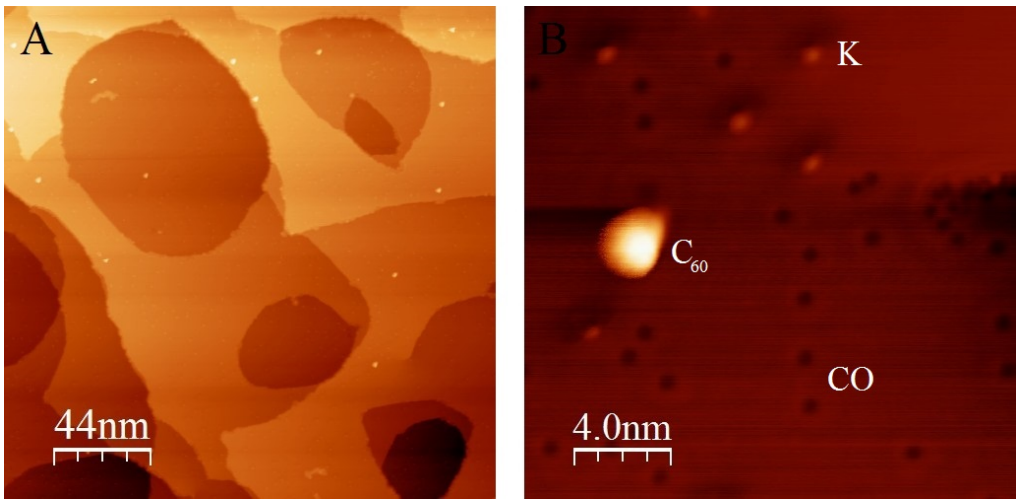

Figure 6.3: A. Large terraces of clean copper are scattered with occasional C_{60} molecules, seen as bright and isolated blobs. In this image, contrast on the potassium atoms is weak making them difficult to see. B. A zoomed in view of the surface. A songle bright C_{60} molecule is surrounded by five K atoms, seen as dim blobs. Additional contaminants, thought to be CO, are seen as dark depressions in the copper surface. Submolecular contrast on the C_{60} molecule is not available here due to the SPM feedback gains being set high so as to scan over the molecule without disturbing it.

6.2.2 Results and Discussions

Significant difficulties were encountered manipulating C_{60} molecules across the Cu(111) surface. Often, instead of moving a molecule, the tip would experience a significant change in apex geometry, or disintegrate. Additionally, when manipulations were achieved, it was frequently seen that K atoms would remain bound in place and not follow the molecule. This was thought to be due to the surface Cu(111) being more reactive as compared to an Ag(001) substrate as used by Crommie in [4]. Nevertheless, a single molecular manipulation was achieved that successfully and sequentially

collected four K dopants. The molecular manipulation process is shown in Figure 6.4. It is not clear why this procedure successfully collected K atoms, considering the failure of previous attempts.

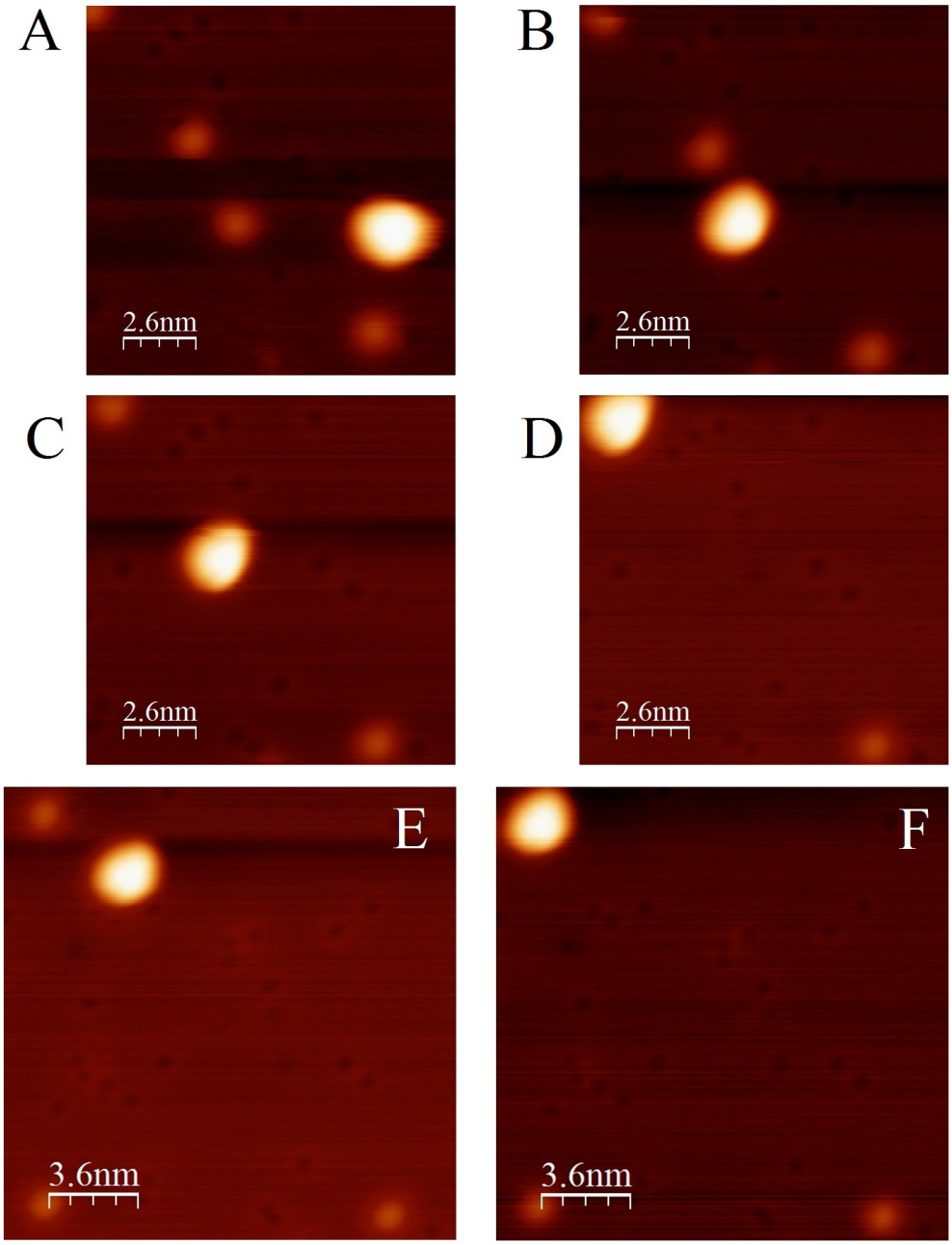

Figure 6.4: STM images in current feedback mode, 1.0V bias voltage. A. Initial image of clean C_{60} and surrounding K atoms. B-D. The C_{60} molecule is sequentially manipulated over three K dopants, which picks them up. E. is a larger image to find a fourth K atom. F shows the C_{60} having been manipulated over that K atom, and so doped to K_4C_{60}.

Dramatic changes were observed in the resultant molecular orbital struc-

ture, as observed via differential conductance measurements. These are displayed in Figures 6.5 and 6.6. Differential conductance results were obtained by differentiating measured I/V spectra. As a result of the differentiation, measurement noise is amplified and so Gaussian filtering was applied.

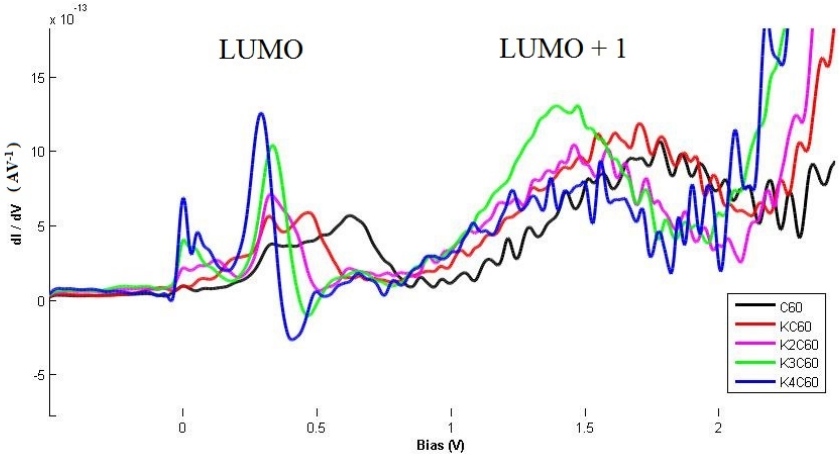

Figure 6.5: . dI/dV measurements of K_nC_{60} of the LUMO and LUMO+1, for $n = 0$ to $n = 4$. A 25 point Gaussian average is performed to reduce noise in the LUMO+1, as such, there is some distortion to the sharpness of some features in the LUMO. Figure 6.6 shows the LUMO with reduced filtering. Each line is an average of between 2 and 4 repeat measurements, where each measurement is additionally an average of a forwards and backwards sweep.

A number of similar features are noticed between dI/dV spectra in Yamachika et. al. [4] (Figure 6.1) of K doped C_{60} on Ag(111), and our measurements on Cu(111). In both undoped systems, the LUMO and LUMO+1 are at 0.5eV and 1.6eV respectively, though on Cu(111) our LUMO exhibited significant splitting. Our results then show the LUMO+1 is progressively shifted towards the Fermi level by approximately 100mV per potassium atom. As in [4], this is thought to be due to the filling of the LUMO shifting the molecular orbitals towards the Fermi level.

Additionally, two important features are apparent that are not obviously present in [4]. Firstly, the LUMO shifts towards the Fermi level, whilst changing shape - a reduction in splitting. The shifting is due to it being filled by donor electrons from the dopants. The change from a split to

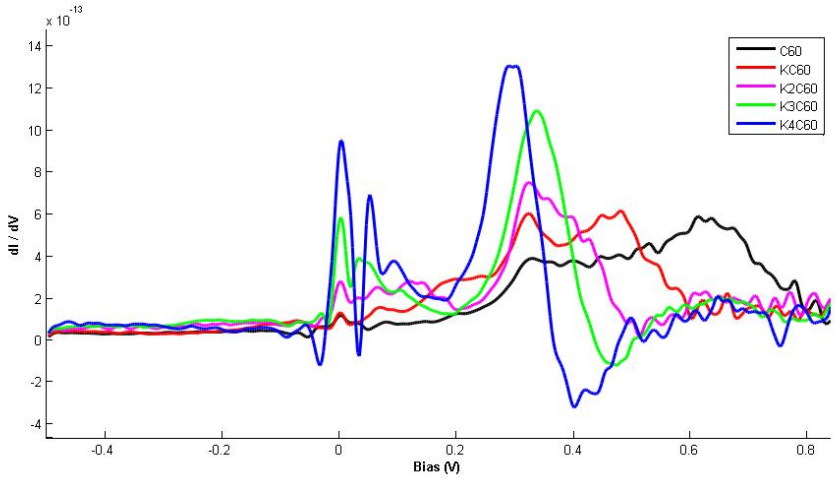

Figure 6.6: . dI/dV measurements of K_nC_{60} of the Fermi level and LUMO, for $n = 0$ to $n = 4$. A 12 point Gaussian average is applied.

single peak could be as a result of a reduction in coupling to the Cu(111) substrate. Strong molecule-surface coupling initially causes a large splitting in the LUMO [65]. As K atoms are added, they sit at the interface between the molecule and the substrate, which could reduce the surface interaction and so any associated splitting. Other presently undetermined features, particularly between the Fermi level and the LUMO, could come from other competing phenomena such as Jahn-Teller distortions as suggested in [4]. Secondly, a new state appears at the Fermi level, and increases in intensity with increased doping. This is likely a result of the increased molecular conductivity due to the doping. Interestingly, the first K dopant does not seem to change this peak, this could be due to additional charge already being present on the molecule due to its strong bonding to the substrate. The first K dopant already significantly reduces splitting in the LUMO, and as such might contribute to a reduction in the surface-molecule interaction to reduce the charge transfer from the surface. Finally, with increased doping, negative differential conductance is observed to appear beyond the LUMO. This could be as a result of resonances between a state on the tip and sample increasing due to the increased sharpness (reduced splitting) of the LUMO. Though it is thought that the tip is metallic, this tip state

could be as a result of a molecule on or near the tip.

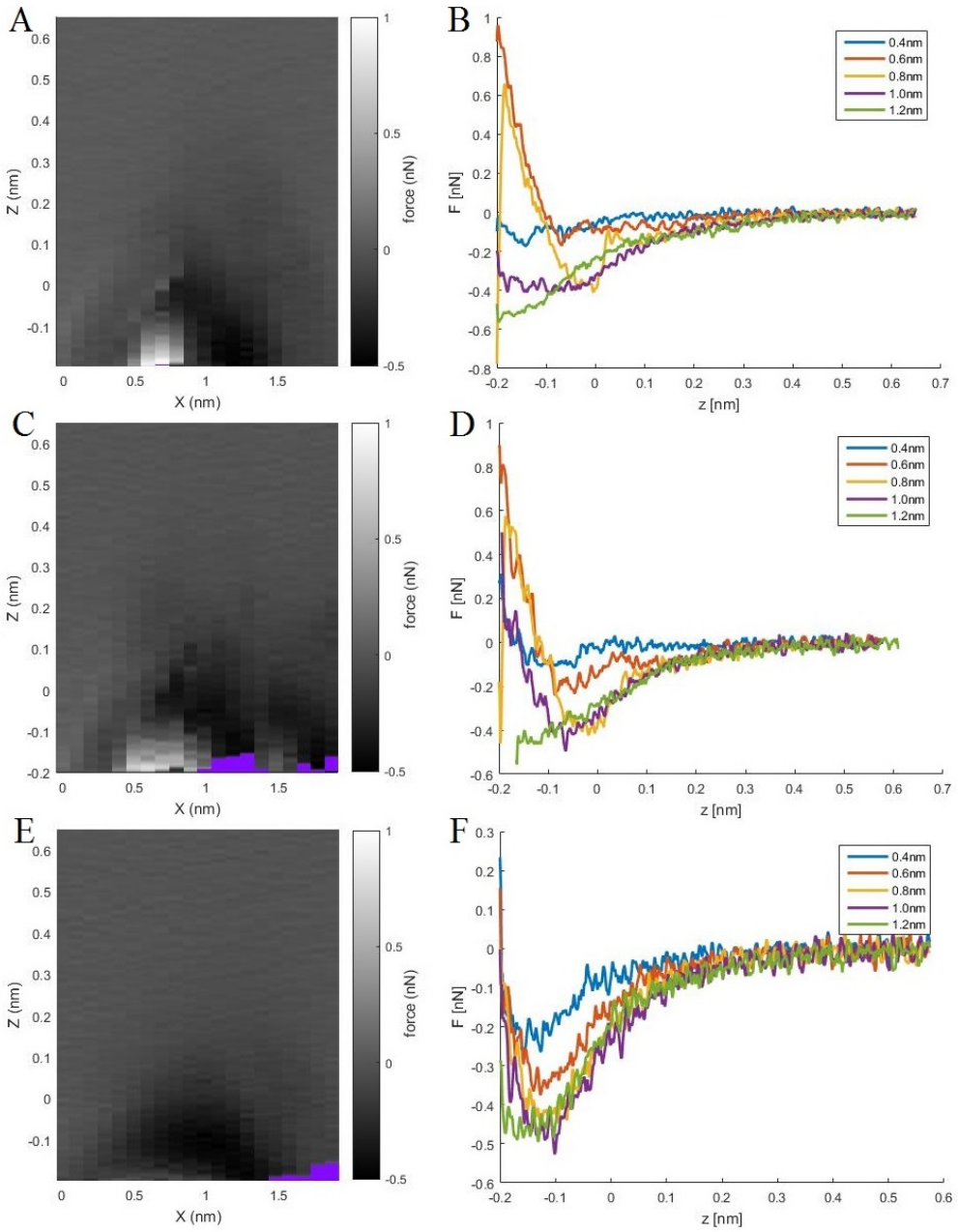

Figure 6.7: . A line of force spectroscopy measurements, across doped and undoped molecules. Graphs are plots of selected spectra. Purple regions are missing data due to background subtraction offsets. Note Z axis alignment is not consistent between B, D and F. **A-B.** Force spectra across a K_4C_{60} molecule. Note very small attractive well on the left hand side of the molecule, of just -0.05nN, compared to -0.4nN on the right. Features in the spectra at $x = 0.8$nm indicate a possible flexible tip interacting with an asymmetric potential. **C-D** A second line of force spectra is collected of the doped molecule, after a small tip change. In C-D, at $x = 1.35$nm, the molecule is manipulated to the right. Force spectra appear similar despite slightly different tip. **E-F.** Force spectra across an undoped C_{60} molecule, with the same tip that collected C-D. Note slight asymmetry in repulsive potential. This however is much smaller than that seen in the K doped molecule.

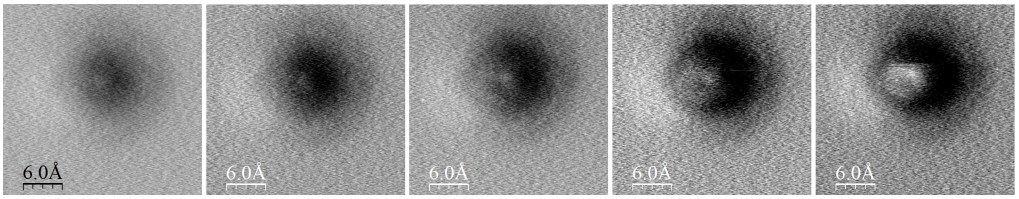

Figure 6.8: Five consecutive AFM images, approaching in Z. Tip change in final image corresponds to the change in tip between Figure 6.7A-B and C-D.

AFM measurements were then conducted over the K_4C_{60} molecule, to examine its force characteristics. These were directly compared to a nearby undoped C_{60}. An important parameter tracked was the 'turnaround' force. As stated in Section 2.3.4, a lower turnaround force implies an increase in the relative attractive component. Additional coulombic interactions with the tip, from the charged molecule, could impact this value. A line of force spectroscopy measurements were taken across each molecule. This helps reduce any uncertainty in the center-of-mass location of the molecule. The results of this are shown in Figure 6.7. The lowest measured turnaround forces, for both the doped and undoped molecule, were approximately -0.45nN. On the doped molecule, a large repulsive term overwhelmed the attractive short-ranged component over the left half the molecule. This could be due to charging on the molecule interacting with an asymmetric distribution of charged K atoms on the tip. The other half of the molecule looked very similar to the clean C_{60} molecule. The slight asymmetry on the undoped C_{60} molecule could be due to an asymmetrically charged tip interacting with normal charge transfer into the molecule from bonding to the Cu(111) substrate.

AFM images in Figure 6.8 confirm the repulsive asymmetry as not a artefact in the force spectroscopy background subtraction process. Additionally, a long-range repulsion to the left of the molecule is visible, further indicating a strong long-range coulombic repulsion.

6.3 Monolayer K_3C_{60}/Au(111) and K_4C_{60}/Au(111)

6.3.1 Experimental Procedure

As before, a pristine Au(111) surface was prepared via repeated cycles of sputter/annealing. A C_{60} sub-monolayer was generated by depositing directly onto the room temperature sample. K was then deposited onto the substrate, and subsequently annealed to assist in the K intercalating into the C_{60} lattice. Further depositions and anneals were completed until a K_3C_{60} or K_4C_{60} substrate was observed. The final surfaces are shown in Figure 6.9.

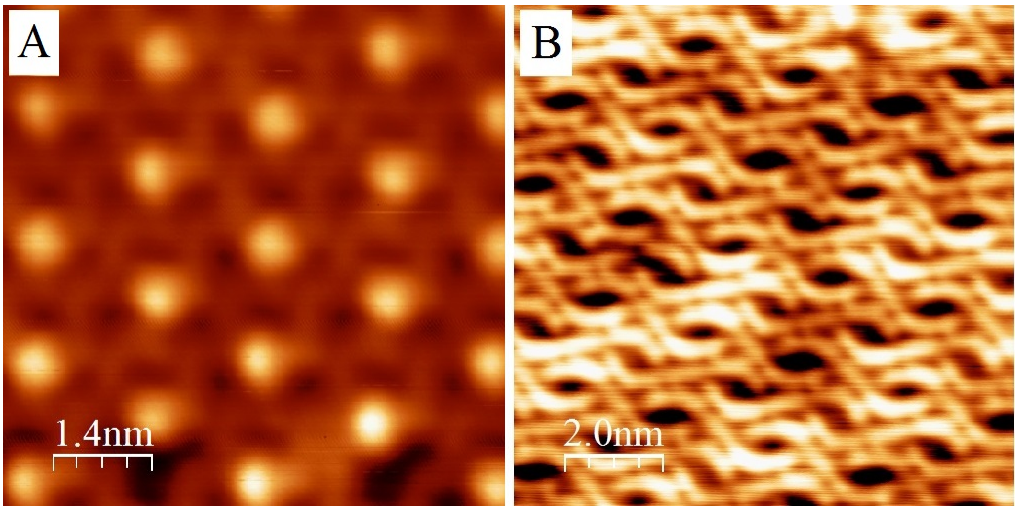

Figure 6.9: A) K_3C_{60}/Au(111), imaged at 1.3V. B) K_4C_{60}/Au(111), imaged at 100mV.

6.3.2 Results and Discussion

K_4C_{60} Monolayer

K_4C_{60} surfaces were observed via STM, and were comparable to those reported in literature[62]. Similar dI/dV curves were measured, confirming the presence of K_4C_{60}. One of these is plotted in Figure 6.10. AFM images were then taken of the surface, and are shown in Figure 6.11. Here submolecular detail is visible and as such, orientational information can be

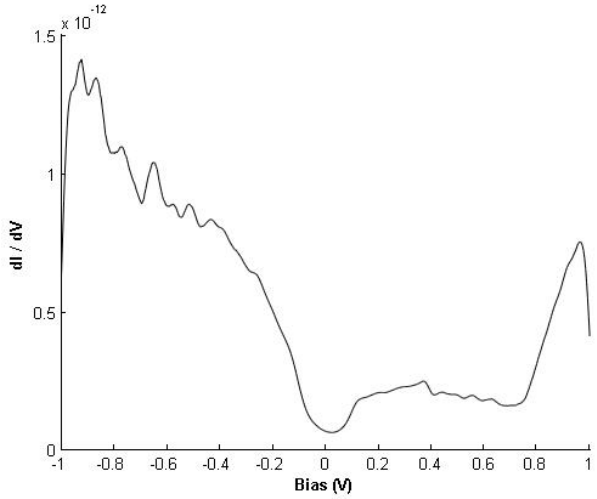

Figure 6.10: A dI/dV plot of a K_4C_{60} island. Showing gap in the density of states at the Fermi level (0V). This closely mirrors the literature[62], as in Figure 6.2E.

deduced. Figure 6.11 indicates that assertions in [62], that the molecules sit double-bond upwards, are correct. Each molecule exhibits a bright repul-

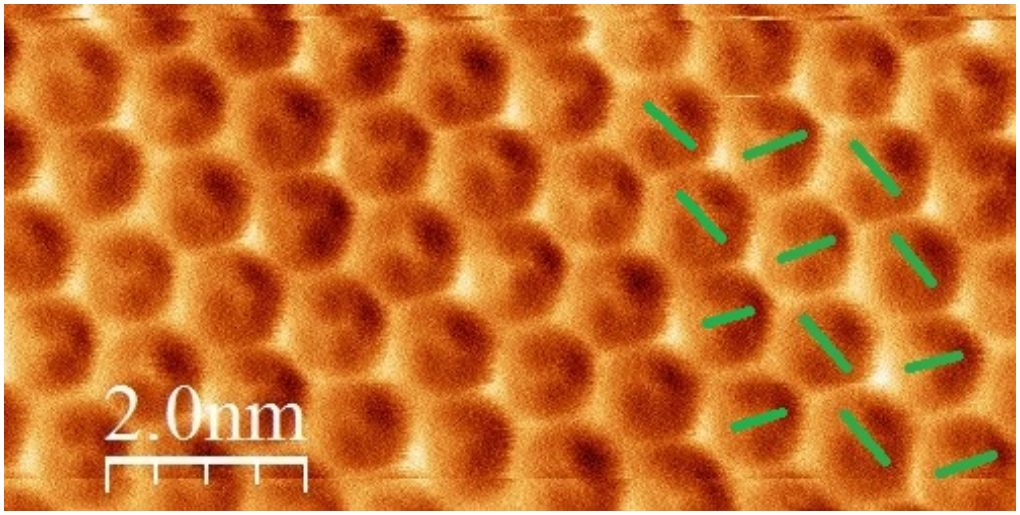

Figure 6.11: . Constant height AFM image of a K_4C_{60} island. Green lines mark the approximate position of observed double bonds.

sive line in the direction of the double bond, flanked on either side by two attractive regions which represent the hexagon on either side of the double bond. Additionally, this image shows a long-range 2×2 order across the molecule, as can be determined by the relative orientations of the K_4C_{60} molecules. No obvious indications of charging were observed via AFM. This could be due to the uniform distribution of the potassium under the

monolayer generating a uniform forcefield on the AFM tip.

K_3C_{60} Monolayer

K_3C_{60} surfaces were imaged using STM and AFM. In addition, differential conductance measurements were conducted, along with a grid of force spectroscopy measurements. STM images of the doped monolayer (Figure 6.9A) showed a clear reconstruction that indicated a K_3C_{60} monolayer, similar to Figure 6.2. Different tips produced different contrasts on molecular and submolecular features. These and their associated AFM images and dI/dV spectra, are shown in Figure 6.12. The tip that imaged Figure 6.12D attained submolecular STM resolution on the monolayer. This enabled an interpretation of the molecular orientations. Bright molecules were seen as double bond up, whilst surrounding dimmer molecules were clearly hexagon-up. Here, the shape of the molecular orbitals do not appear significantly different to undoped monolayers. AFM images showed a number of interesting features. Firstly, an elevated repulsive term was observed over the double bond-up molecules, this indicating that they are indeed raised compared to their neighbours. This is indicated in Figure 6.13. Secondly, additional contaminants thought to be additional K dopants were observed on top of the monolayer. These were imaged sitting in the hollow sites between three molecules. Normal AFM scanning would periodically manipulate these across hollow sites within the island. One such manipulation is shown in Figure 6.14.

The modification between the measured dI/dV spectra in Figure 6.12C and F, is due to a change in the tip electronic structure. The addition of a C_{60} terminating the tip means collected dI/dV spectra in Figure 6.12F are a convolution of the MOs on the tip and surface. Due to the C_{60} band gap, a molecule on the tip could induce a splitting of the peak at the Fermi level in Figure 6.12C. Two peaks are observed to develop in Figure 6.12F, at

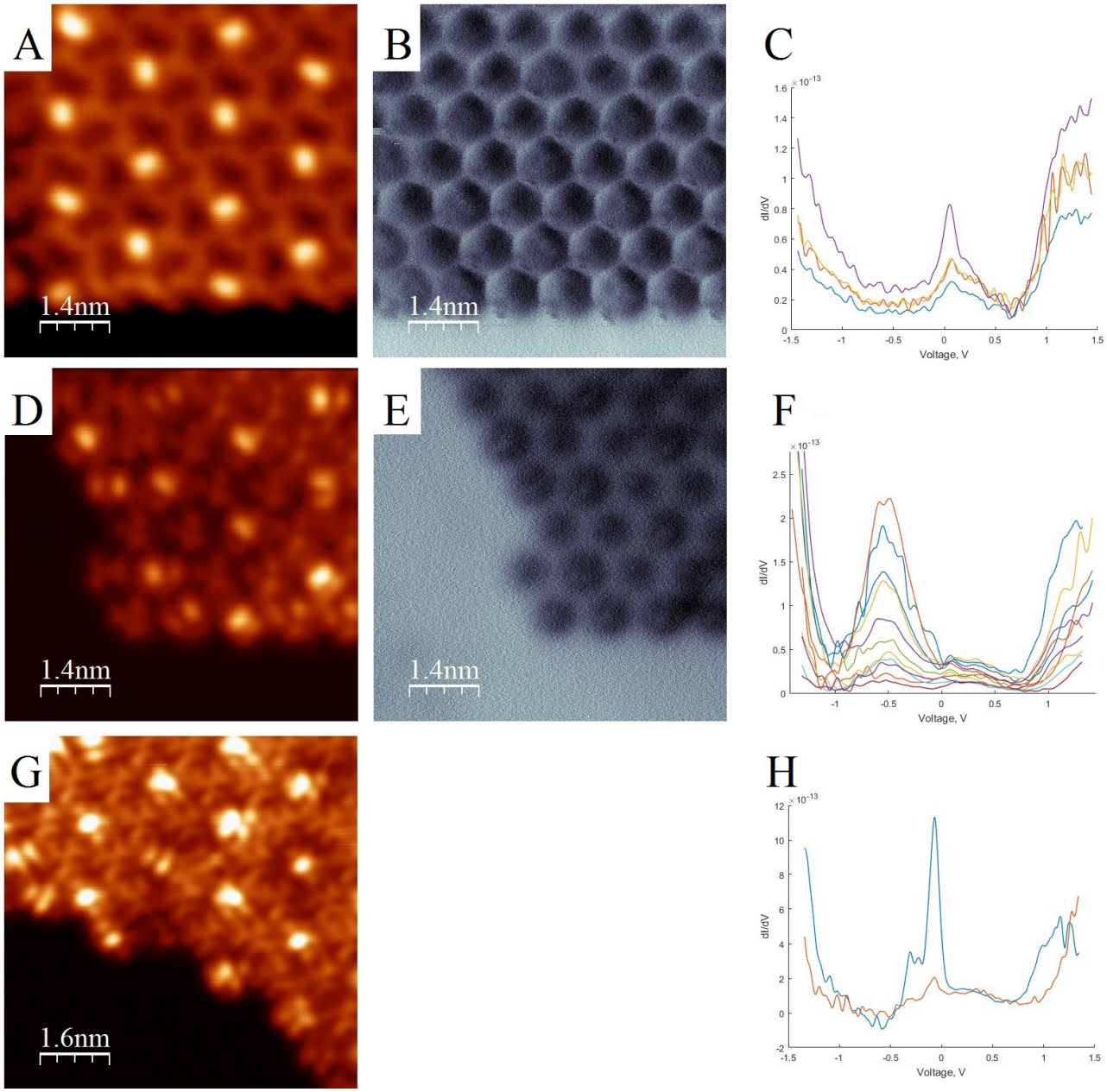

Figure 6.12: . STM and AFM images of the same K_3C_{60} island, with different tip geometries. STM data acquired at 1.3V. **A-C.** STM contrast similar to other images in literature[62]. The associated AFM contrast, however, exhibits unusual boundaries between molecules. Tip termination is unknown, but possibly metallic. K dopants in hollow sites are not visible. dI/dV spectra show clear K_3C_{60} features, with a large peak at the Fermi level. AFM scanning disturbed the island and picked up a C_{60} to the tip, leading to the subsequent tip configuration in D-F. **D-F** Tip produces good submolecular resolution, with C_{60} tip. AFM image shows expected contrast and shows extra repulsion over double-bond up molecules. K dopants in hollow sites are visible as attractive wells. dI/dV spectra taken across the island are substantially different, with no peak at the Fermi level, and a large peak developed at -0.5V. **G-H.** STM shows submolecular resolution on molecules, however orbitals seem to be distorted as compared to D. AFM imaging was unstable with this tip. dI/dV spectra again resembles K_3C_{60}.

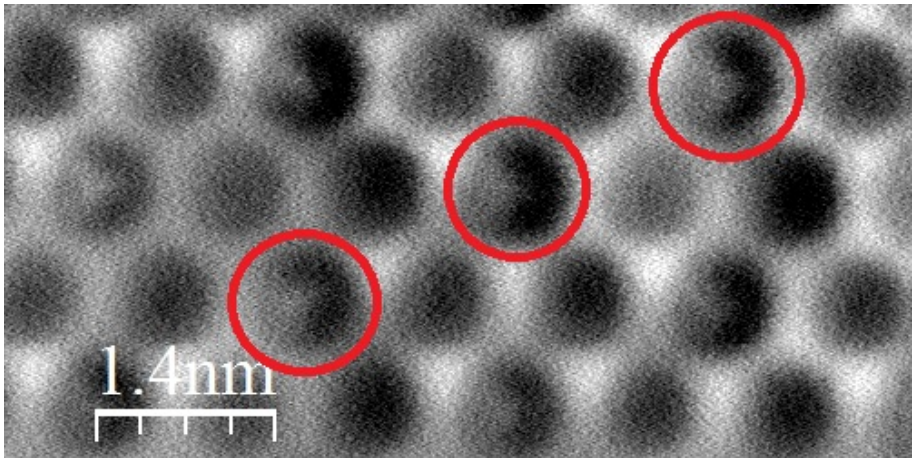

Figure 6.13: . Constant height AFM image of a K_3C_{60} island, taken over same location as STM image in Figure 6.9 A. Red circles mark three buckled C_{60} molecules from periodic reconstruction.

-0.5V and at 0.3V. Surface K atom manipulations were seen to alter the

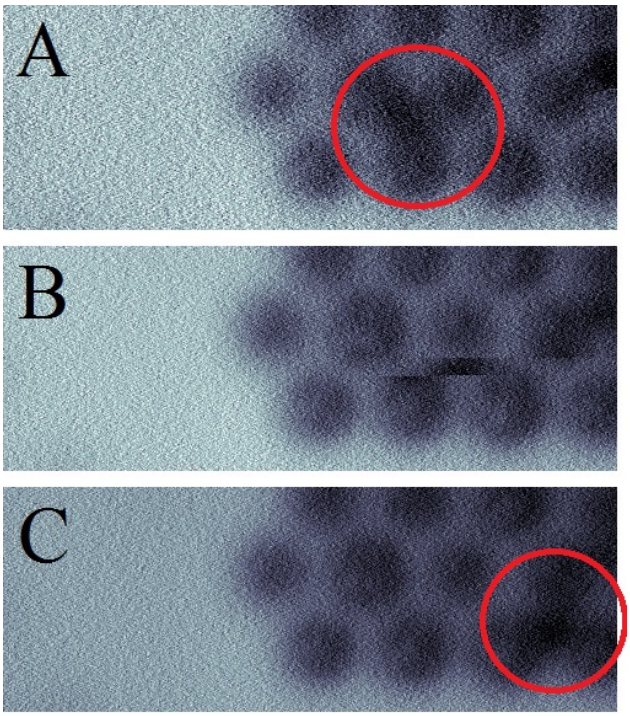

Figure 6.14: . AFM images of a K_3C_{60} island. A-C. We propose the dark feature is a K atom, as seen circled in red. Here it is manipulated between hollow sites by AFM scanning (scanning up).

electronic structure of the monolayer. Of the dI/dV spectra collected, a number of them could accurately have their dopant level determined. This by counting dopants adjacent to these molecules in AFM scans. These are shown in Figure 6.15. With the presence of additional dopants, the state

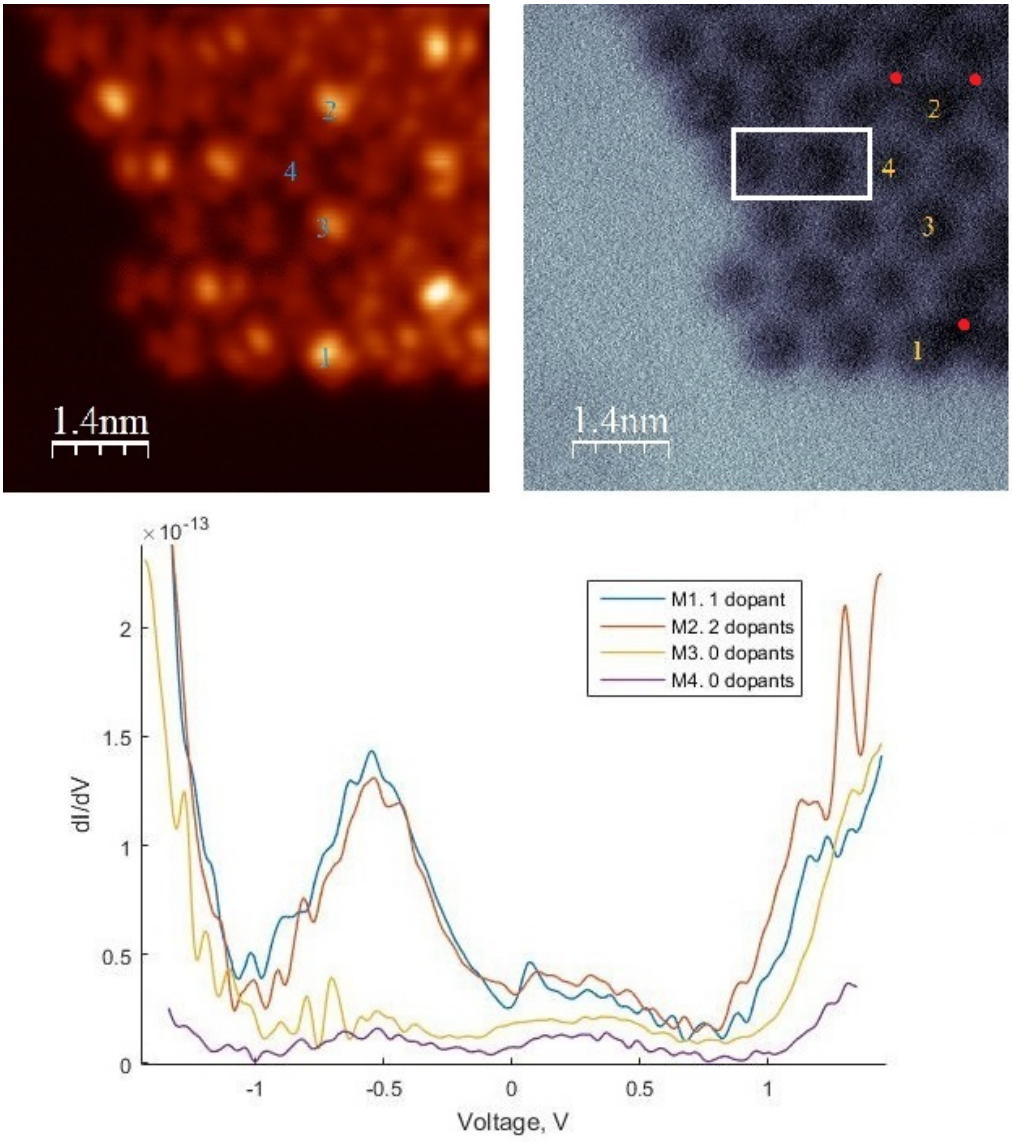

Figure 6.15: . dI/dV plot of monolayer K_3C_{60}, with additional surface dopants. Locations of molecules indicated on associated STM and AFM images. All spectra taken with the same tip. Locations of K dopants adjacent to the molecules of interest are indicated with red marks. White box indicates location of grid spectroscopy measurement, in Figure 6.16.

below the Fermi level, at -0.5V, has grown significantly. With a negative a sample bias, tunnelling is from filled states in the surface to empty states in the tip. This indicates more available filled states in the sample, leading to the conclusion that the surface dopants are contributing electrons to the LUMO band of the monolayer. The magnitude of the increase in the state at -0.5V, could be due to the location of the mobile K dopant. They are above the monolayer, rather than below it. This could mean changes in

the orbital structure are more apparent due to the reduction in screening effects. Here, in Figure 6.15, the two doped molecules exhibit very similar dI/dV spectra, even though they have different levels of doping. This could be due to each dopant having three molecular neighbours. As such, it is not guaranteed that the dopant will contribute an equal amount of charge to each of its neighbours.

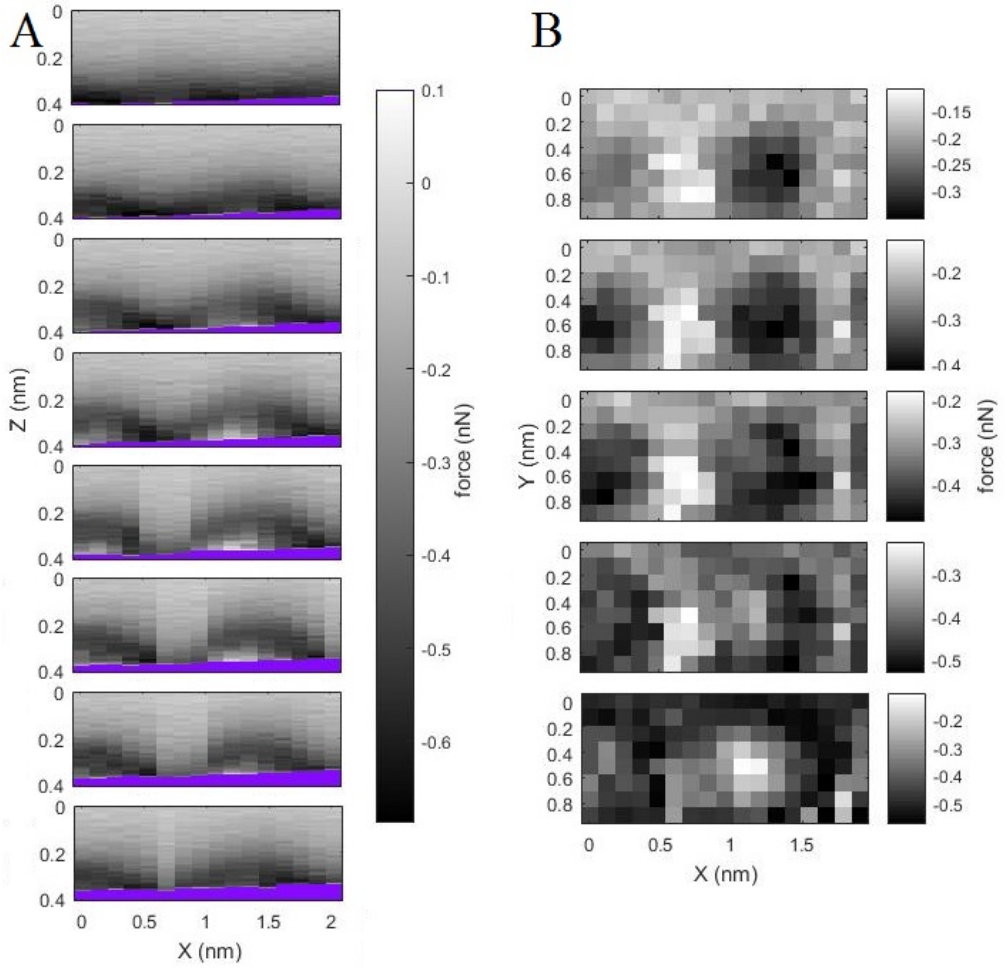

Figure 6.16: . Grid spectroscopy measurements of two molecules on a K_3C_{60} monolayer. The location of the grid is indicated by a white box in Figure 6.15. A. Slices down the grid, showing the force response in Z. The Z spacing between slices is 0.112nm. Note the bottom of the slices are tilted. This is due to residual slope in the background correction. Note as well the drift upwards after successive scans. This is due to thermal drift in the system over the course of the grid. Both of these factors, however, are effectively removed due to our background subtraction strategy. B. Slices across the grid. Each slice has a ΔZ spacing of 0.04nm. The lowest slice is at Z=0.35nm.

A force grid spectroscopy measurement was taken across two molecules in Figure 6.16. The aim of this is to explore force contributions from K

dopants at the surface-monolayer interface, and in particular to explore whether the surface reconstruction impacts molecular charging. The left hand molecule is double bond up. The right hand molecule appears raised according to the K_3C_{60} orientational long range order, and is oriented atom up. Neither molecule has K dopants in adjacent hollow sites. This was due to the possibility of a mobile K dopant being picked up during the grid measurement. As seen in Figure 6.16, molecules apply a similar force profile to the tip, with turn-around forces of approximately 0.4nN. The right hand molecule comes into repulsion faster due to its height difference. This difference is measured at 0.02nm. Though higher, this is not enough to indicate a surface reconstruction. Purely considering the geometry of the molecule, the height difference considering the corrugation of the molecule when rotated is of a similar length scale. The height difference between an atom-up orientation compared to a double-bond-up molecule is 0.015nm. As such, it is likely that the relative brightness of the right hand molecule in STM is purely due to its orientation, and not a surface reconstruction. In general, neither molecule appeared significantly different, indicating similar charging levels across both molecules. One unusual feature is that for the right hand molecule, the centre of repulsion does not align with the centre of attraction, as can be observed between the first and last slice across the grid. It has shifted -0.23nm in x (to the left). This cannot be explained by the molecule's orientation, as the highest atom of the molecule is to the top right of the molecule, not the left, so any shifts as a result of molecular orientation would be expected in the opposite direction. As such, this could be due to asymmetries in charging under the molecule. dI/dV measurements are unfortunately not available in this case.

6.4 Conclusion

K-doped C_{60} has been investigated via STM and AFM in a number of different surface and molecular configurations. Doping an isolated C_{60} on Cu(111), by successively manipulating it over surface dopants, showed that potassium doping led to a charging of the LUMO. A reduction in LUMO splitting was observed, possibly due to reduced surface interactions, as well as shift of the LUMO towards the Fermi level. An additional state developed at the Fermi level due to increased molecular conductivity. Negative differential conductance was observed to develop above the LUMO with increasing doping. This was thought to be as a result of the reduction in LUMO splitting and so increased resonance with a state on the tip. The LUMO+1 was additionally seen to shift towards the Fermi level, as seen in [4]. Line force spectroscopy measurements across the doped K_4C_{60}, and an undoped molecule, showed significant differences. The doped molecules exhibited an asymmetric repulsive component. This indicated a long-range, repulsive electrostatic interaction, and a possible asymmetric charging on the molecule or tip.

In K_4 doped monolayers, AFM investigations confirmed the molecular orientation of the island, by observing the orientation of imaged double bonds. In K_3 doped monolayers, molecular orientations were determined via STM, and semi-mobile dopants atop the doped layers were observed via AFM. These dopants were observed to have a significant impact on differential conductance measurements. A large state was seen to develop below the Fermi level as a result of this doping. A grid force spectroscopy measurement over two molecules, one of which is appeared brighter in STM, was taken. Differences observed in the height of the two molecules are not significant enough to say that a surface reconstruction is occurring. Additionally, a similar charging levels between the two molecules was indicated as they appeared similar.

Chapter 7

Maxwell's Demon Using an STM probe - A Monte Carlo Simulation of a Molecular Pump

7.1 Introduction

Advancing the field of SPM is both an engineering and scientific challenge. The needs of experimentalists drive the 'in house' and commercial development of further enhanced systems. Thus, as scanning probe techniques are refined, ever more challenging scientific endeavours may be attempted.

An application of advanced SPM techniques might be to execute the 'Maxwell's demon' thought experiment on a surface, as mediated by an STM tip. This chapter is a feasibility study of that experiment, via a Monte Carlo simulation of molecular diffusion in a confined geometry. We investigate the effect of tip position, temperature, and chamber geometry on molecular diffusion, to optimise the chances of conducting a successful experiment.

7.1.1 Maxwell's Demon

In 1871, physicist James C. Maxwell presented the now famous thought experiment known as Maxwell's demon[66]. This thought experiment relates to the thermodynamics of gas molecules and was introduced specifically to explore how the second law of thermodynamics could be violated. The second law states that the total entropy of a system will always increase in a closed system. The gedankenexperiment was set up as follows. Two chambers, each filled with a gas exist side by side. A gate between them is guarded by a 'demon'. The demon can control the gate, such that it is open or closed. As time progresses, gas molecules will attempt to pass through the gate. The demon will only allow slow, or low-energy, gas molecules through one direction, and faster, higher energy gas molecules through the other direction. As time progresses this simple process will lead to a violation of the second law of thermodynamics. One chamber now has an increased temperature, while the other is cooled. With no work expended,

entropy has reduced.

7.1.2 Executing Maxwell's Demon via SPM

A number of significant challenges exist before this gedankenexperiment could be realised in the context of a scanning probe experiment. These revolve around three main aspects. Firstly, two chambers must be constructed on an atomic scale, on a surface with an SPM tip. These two-dimensional chambers must be capable of effectively confining a diffusing species within their walls. The gate between them must be sufficiently small such that only a single 'gas' particle may pass at a time. Secondly, a 'gas' of diffusing molecules must be deposited within the walls of these chambers. They must be able to freely diffuse, and not clog the gate. Finally, an SPM tip must monitor the gate between the two chambers. A system must be implemented to allow the SPM to act as a one-way valve, such that it monitors both sides of the gate and determines whether to allow or block diffusing molecules from passing through the gate.

Building Two Connected Chambers on a Surface

Two interconnected chambers could be constructed via the use of bound C_{60} molecules, on a hydrogen passivated silicon (100) surface. This surface is useful as it is highly unreactive in its pristine state. A hydrogen atom can then be locally desorbed from the surface via high current tunneling with an SPM tip. The resultant dangling bond is highly reactive which a diffusing C_{60} molecule will bond strongly to. This is ideal as it allows, via precise desorption of hydrogen in the shape of the chamber walls, the creation of C_{60} 'walls' along these depassivated areas. Meanwhile, an unreactive surface within the chambers is maintained, which is ideal for molecular diffusion. This is shown in Figure 7.1. A challenging aspect of this process is in the preparation of the hydrogen passivated surface, and

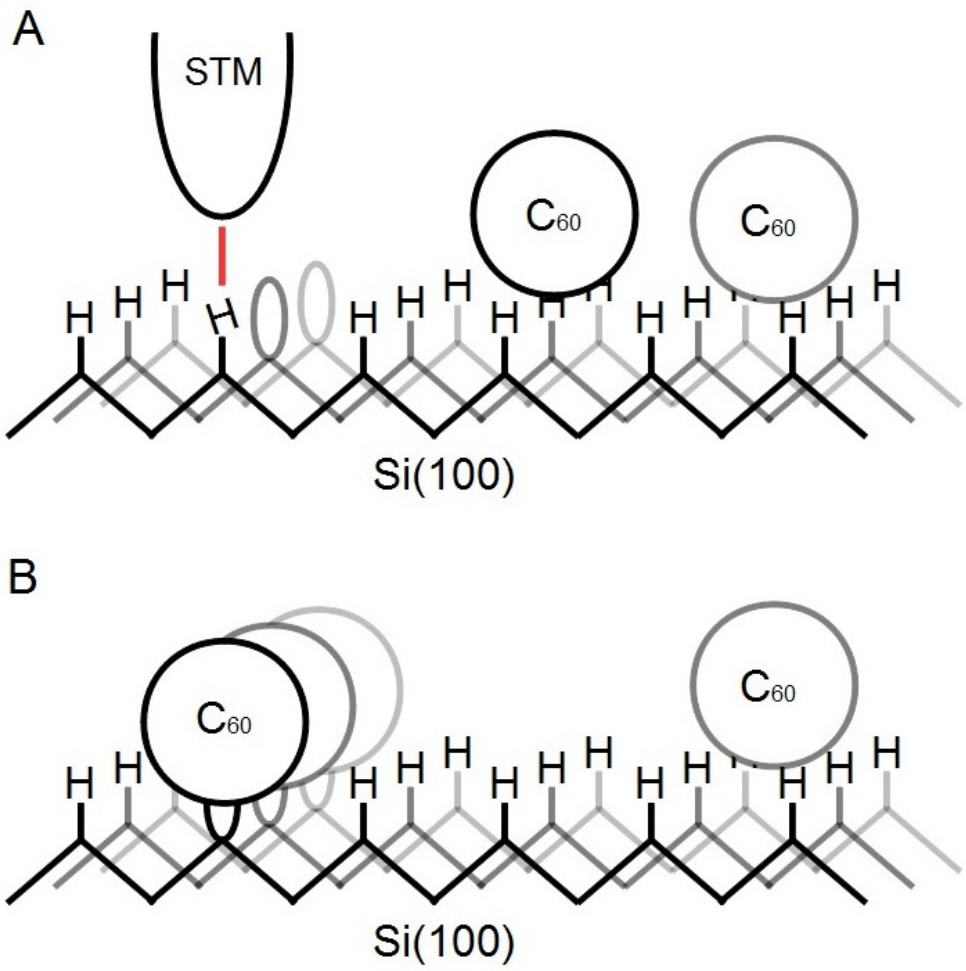

Figure 7.1: A simplified schematic of a hydrogen passivated Si(100) surface is configured for a Maxwell's Demon experiment. A) A row of single H atoms are desorbed from a H-passivated Si(100) substrate, creating a row of reactive dangling bonds. C_{60} molecules are able to diffuse on the passivated surface. B) A number of C_{60} molecules have diffused onto the highly reactive dangling bonds and chemisorbed, forming a fixed barrier. A second C_{60} remains mobile atop the passivated surface.

the atomically precise depassivation of hydrogen bonds. Before the surface is exposed to the hydrogen, it remains extremely reactive. As such, any contaminants in the chamber can affect the quality of the surface. Additionally, depassivation must be extremely precise around the gate to ensure it is the correct width to allow molecules to pass.

A Suitable 'Gas'

Given a chamber fabricated via C_{60} molecules, more C_{60} molecules could then be deposited onto the surface to fill the chambers, or the chambers could be built "around" molecules already on the surface. An important aspect is the temperature of the surface. If the temperature is too low, the diffusion rate over the surface will be very low, and in the time scales of a reasonable experiment, no changes would be observed. Additionally, the molecules could aggregate at the edges of the chamber walls, or worse, clog the gate.

Tracking Molecular Motion With an STM Tip

An STM tip in constant height mode may be brought to the gap between the chambers. It is rapidly dithered at a frequency of 5-10KHz around the gate. As a molecule diffuses under the tip, a rise in tunnel current will be detected. Depending on where the tip is in its motion, it might be possible to determine from which chamber the molecule originated from. Thus the tip could upon detection, do nothing, or advance towards the surface to block the path of the diffusing molecule. It is important that the tip is close enough to the surface to register this change, but not too close to interact strongly with the molecule. The bandwidth of the STM pre-amplifier must be fast enough to register the change in tunnel current, and the dither on the tip must be at a frequency comparable or faster than the rate a molecule could diffuse under the tip. Under these constraints, the temperature of the substrate must be low enough that the molecular motion is slow enough for the tip to track. This means there might be a narrow window of temperatures where a diffusing molecule is moving slowly enough to be detected, whilst having a sufficient energy to diffuse away from the chamber wall and not clog the gate.

Blocking a Molecule's Path

Once a C_{60} molecule has been detected, a decision must be made whether or not to block its motion. The original Maxwell's demon considers the relative speed of molecules, however this is practically difficult for an STM tip. Maxwell also envisaged a 'pressure demon' which is identical to what is described here. Instead of separating faster and slower molecules, it is instead 'pumping' them from one chamber to the next, irrespective of their speed. The tip must block the path of a molecule automatically and consistently, without accidentally picking that molecule up.

7.1.3 Hopping Rate and Monte Carlo Simulations

A Monte Carlo simulation was written to examine the dynamics of a single molecule diffusing across a potential landscape. This landscape as generated by a surface potential, C_{60} molecular walls, and an STM tip, where the tip termination is assumed to be a C_{60} molecule.

7.2 Single Molecule Diffusion Simulation

A single C_{60} molecule was modelled, diffusing through an energy landscape induced by a number of static C_{60} molecules, and on a lattice defined by a hydrogen-passivated Si(100) surface. To properly estimate the potential landscape in the simulation, and so the hopping rates, the interaction energy from each C_{60} must be considered at every Si(100) binding site considered within the simulation. The C_{60} contribution to the potential field is generated via an analytical potential known as the Girifalco Potential [67]. This spherically symmetric potential has been shown to be accurate [25] and is sufficient for the purposes of this simulation. This long-range potential is summed to a periodic and sinusoidal surface potential.

The Girifalco potential is a combination of an attractive and repulsive

component, to consider the van der Waals and Pauli repulsive parts of the C_{60} potential. This potential between two molecules i and j, is given by the following relation:

$$E_g(r_{ij}) = -\alpha\left(\frac{1}{s_{ij}(s_{ij}-1)^3} + \frac{1}{s_{ij}(s_{ij}+1)^3} - \frac{2}{s_{ij}^4}\right) + ... \\ ...\beta\left(\frac{1}{s_{ij}(s_{ij}-1)^9} + \frac{1}{s_{ij}(s_{ij}+1)^9} - \frac{2}{s_{ij}^{10}}\right) \tag{7.1}$$

where

$$s_{ij}(r_{ij}) = \frac{r_{ij}}{2a} \tag{7.2}$$

$$\alpha = \frac{N^2 A}{12(2a)^6} \tag{7.3}$$

$$\beta = \frac{N^2 B}{90(2a)^{12}} \tag{7.4}$$

Here, r_{ij} is the centre to centre intermolecular separation, N is the number of atoms in the molecules - 60, and a, A and B are parameters that calibrate the different energy contributions within the potential.

A plot of the potential, where when r_{ij} is in Angstroms, $a = 3.55$, $A = 20.0$ and $B = 34800$ is shown in Figure 7.2. These values were calculated by Girifalco et. al. in [67] for C_{60} - C_{60} interactions.

The hydrogen-passivated silicon (100) surface has a well-known energetic barrier to diffusion for phisisorbed species similar to C_{60}. We assume that the C_{60} molecule does not chemically interact with the surface. Additionally, for simulation simplicity, a square instead of rectangular lattice was used for the hydrogen passivated Si(100) surface, with a lattice spacing of 0.352nm. This is the closest distance between two adsorped hydrogen atoms on H-passivated Si(100). The periodic energy profile of the surface can be modelled in a number of ways. A periodic square potential will produce accurate results in isolation, however once additional molecular contributions to the potential are added, it quickly loses accuracy. A sinu-

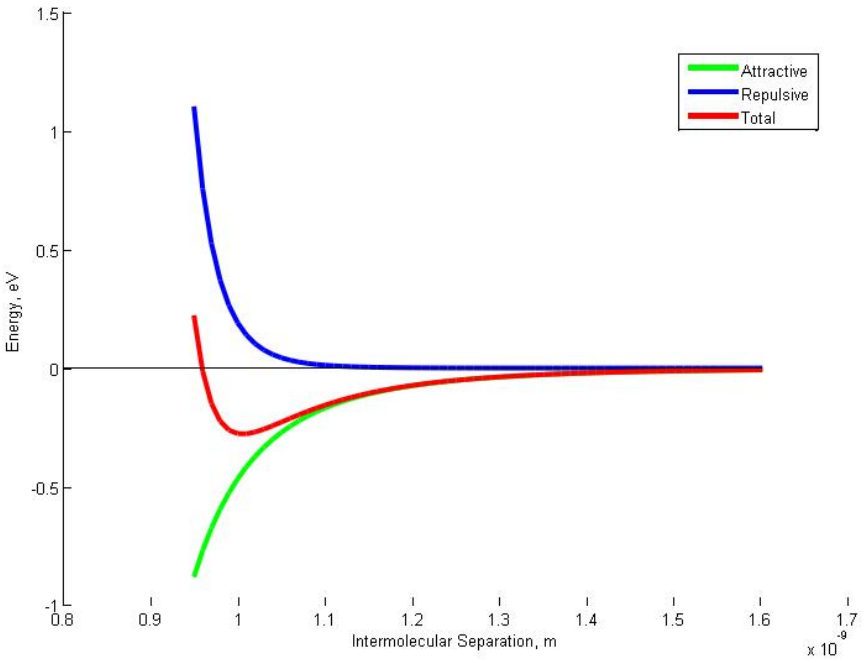

Figure 7.2: The attractive and repulsive components of the Girifalco potential. Note that the potential minima is just greater than 1nm, the approximate van der Waals radius of a C_{60} molecule.

soidal potential is a far superior method for estimating the intermolecular potential and has been widely used to model lattice diffusion potentials [68, 69]. The sinusoidal potential is given by the following equation:

$$V_s(x) = \frac{1}{2} E_b \cos\left(\frac{2\pi x}{a_0}\right) \tag{7.5}$$

where E_b is the diffusion barrier and a_0 is the lattice spacing.

A comparison between a square and sine periodic surface potential is shown in Figure 7.3. Thus the direction specific energy barrier to diffusion can be estimated by considering the sum of a sinusoidal surface potential, and either single or multiple C_{60}–C_{60} interactions mediated via the Girifalco potential. The total potential between two binding sites becomes:

$$V(r, x) = V_s(x) + \sum E_g(r) \tag{7.6}$$

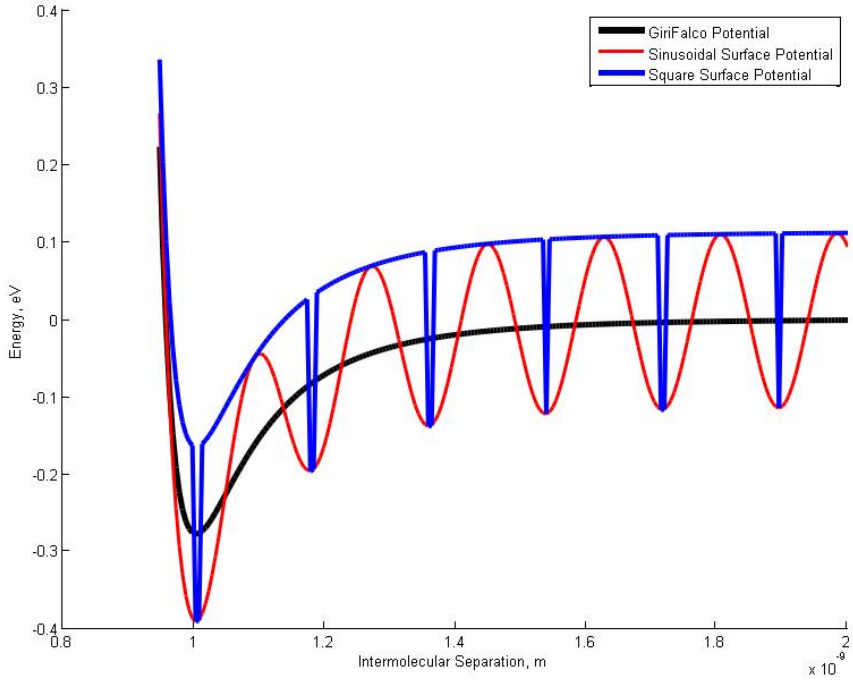

Figure 7.3: A square and sinusoidal potential, modelling a periodic lattice potential is added to a Girifalco potential as generated by a C_{60} molecule. The amplitude of the periodic surface potential is defined by the C_{60}H-Si(100) binding energy. Note that the energy barrier generated by the square wave leads to inflated energy barriers compared to the sinusoidal potential. This primarily in regions where there is a high gradient in the Girifalco potential, both towards and away from the molecule. The peaks of the sinusoidal potentials between the binding sites were observed to be slightly shifted due to changes in the shape and strength of the Girifalco potential.

The diffusion energy barrier is the difference between the binding site energy, and the maximum energy between its adjacent binding site.

7.2.1 Initialising the Simulation

As we only consider the motion of a single molecule, the potential landscape of the simulation will not change. As such, this can be calculated just once at initialisation. The energy profile between binding sites is calculated by considering 75 evenly spaced points between each site, and applying Equation (7.6). The direction-specific diffusion barrier is then calculated, this by finding the energy difference between the binding site and the maximum energy of the inter-site energy profile. The hopping rate is then calculated

via the following equation.

$$\Gamma = \nu_0 \exp\left(\frac{-E_b}{K_b T}\right) \tag{7.7}$$

where E_b is the calculated diffusion barrier. This initialisation process is relatively fast and only takes 16 seconds via a single threaded program running on a 4.2GHz processor core.

The motion of a single molecule is then modelled using a kinetic Monte Carlo algorithm as outlined in Section 3.2.2. Two connected chambers, constructed using fixed C_{60} molecules, were considered in the simulations. A C_{60} molecule was additionally placed vertically over the opening to model a tip-termination. Inter-binding site hopping rates were calculated, and applied to a Monte Carlo simulation.

A heatmap showing the potential landscape as generated by the summed Girifalco potentials is shown in Figure 7.4.

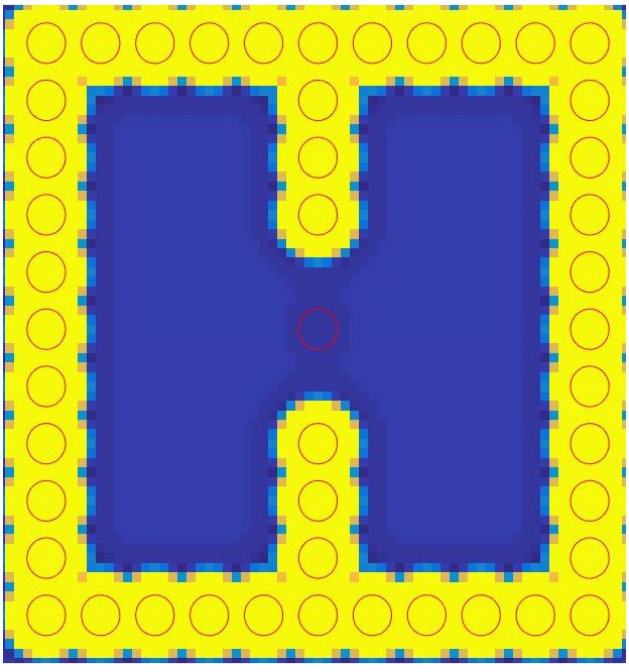

Figure 7.4: A logarithmic heatmap of the GiriFalco potential, as generated by fixed C_{60} molecules. Red circles are present to display the locations of C_{60} molecules. The pixel spacing is equal to half the surface lattice spacing.

7.2.2 Hopping Rate Results

An example map of estimated hopping rates, for a temperature of 150K, is shown in Figure 7.5. Large differences in hopping rate exist between molecules in proximity of other molecules, and molecules in free space. The tip molecule, whose position is indicated by a red dot, has a 1.1nm tip-sample separation. This clearly has an impact on the local molecular hopping rate beneath it.

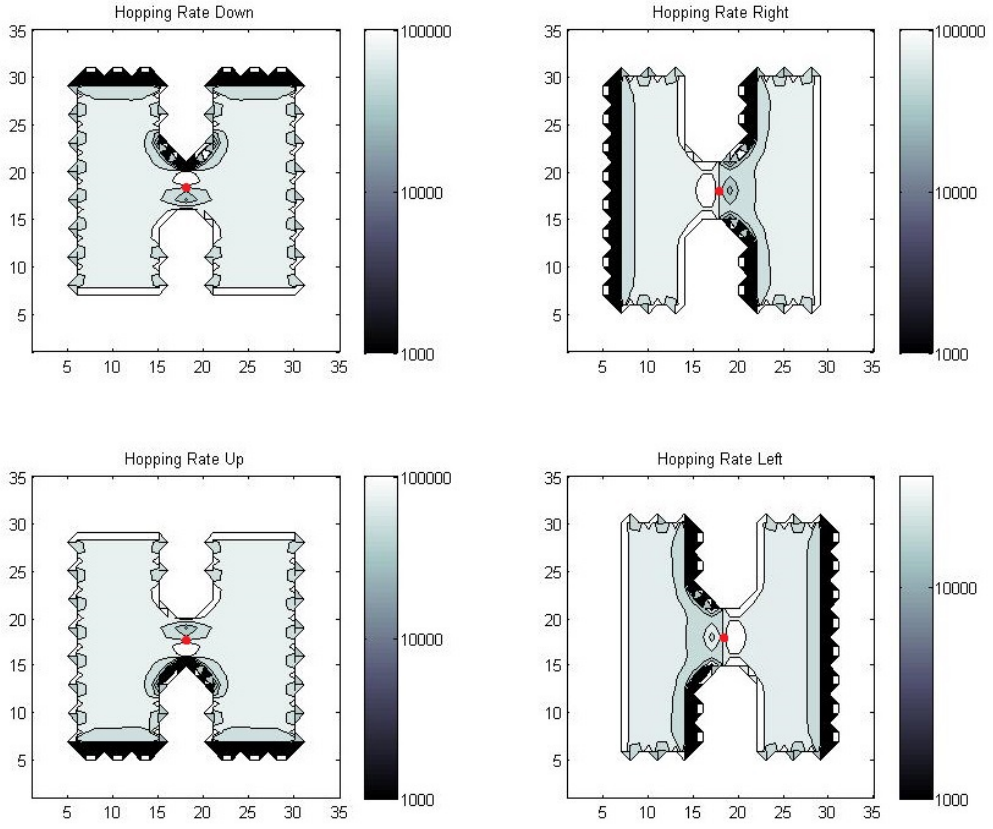

Figure 7.5: The direction specific hopping rate for each binding site, for a surface temperature of 150 Kelvin and a tip height of 1.1nm. The color scale has been set to focus on the hopping rate around the tip and exposed surface. Towards the edges of the molecular walls there are changes in hopping rate that are out of range, even using a logarithmic scale. This figure shows the hopping rate away from C_{60} edges is greatly reduced, as shown by the black bands. This is as expected. Single points very close to the island edges show very high hopping rates away from the molecule. These due to the repulsive component of the GiriFalco potential. The tip molecule, at a 1.1nm height from the surface induced a local two orders of magnitude change in the hopping rate under the tip.

It was observed that the presence of the tip molecule created a potential well beneath the tip. The location specific hopping rate leads to a likelihood

that a molecule could become trapped under the tip. By varying the temperature of the simulation, and the tip-surface separation, it is possible to explore the parameter space of this potential well. This is shown in Figures 7.6 and 7.7. In Figure 7.6, it was noted that the difference in hopping rate for molecules that were separated from the influence of adjacent molecules, and molecules which were very close to bound C_{60} surface molecules, was very large. Five to eight orders of magnitude, depending on the temperature. This indicates that previous assessments that instantaneously, only a single molecule would likely be moving across the free surface was correct.

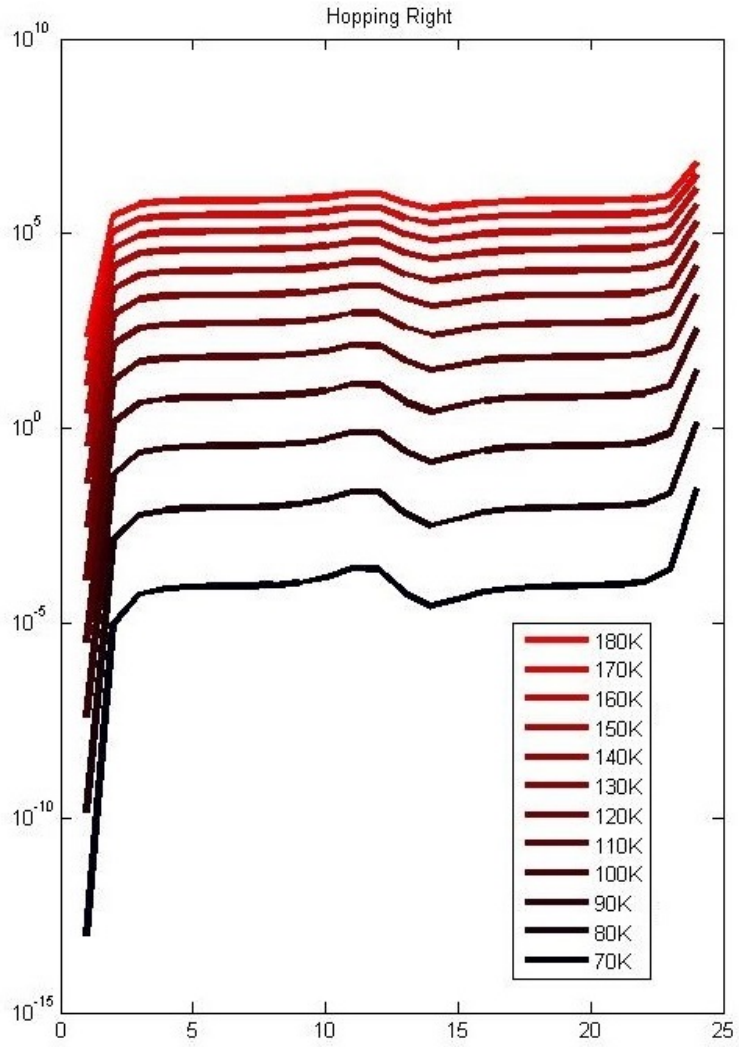

Figure 7.6: Site specific hopping rates. A cross section of Fig. 7.5B, calculated for a range of temperatures. Cross section taken across the middle of the image, such that it intersects with the tip molecule.

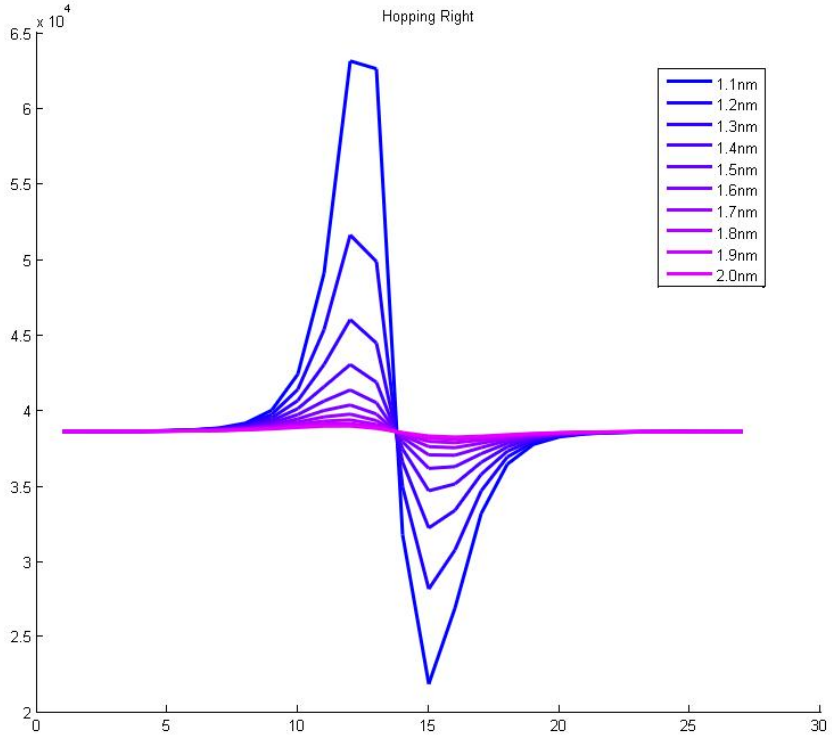

Figure 7.7: The direction specific hopping rate of a C_{60} molecule (to the right) under a tip molecule. The tip molecule height is modified and the resultant changes in hopping rate tracked. Other than the tip molecule, no other molecules are included in this hopping rate calculation.

Further investigation into the effect of the SPM tip molecule on the diffusion rate in Figure 7.7 showed that at very close tip-sample separations, the hopping rate was only modified by a factor of two. Due to the large size of the potential well, this could lead to significant molecular trapping. Further investigation of the time taken for a molecule to traverse the surface of the sample, and the locations where the molecule was most likely to occupy, was investigated via a Monte Carlo simulation.

7.2.3 Monte Carlo Calculations

While significant information about a system can be inferred simply by estimating hopping rates, applying these in a Monte Carlo simulation can assist in the interpretation of this data. In this simulation, two key param-

eters were tracked: the simulation time, and the positional history of the diffusing molecule. The positional history of such a simulation is illustrated in Figure 7.8.

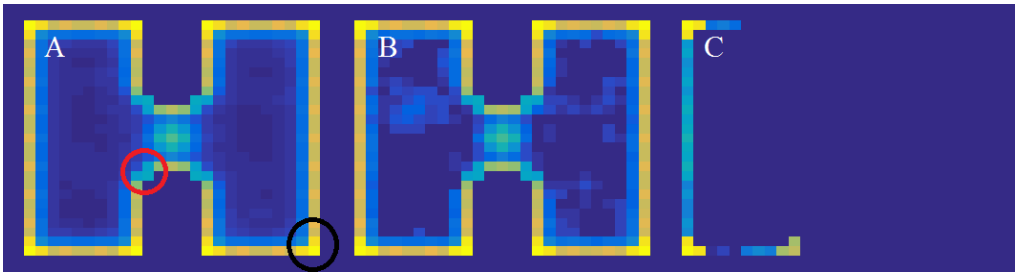

Figure 7.8: Three logarithmic heatmaps of the locations occupied during three Monte Carlo simulations, for three different temperatures. Each heatmap represents 480 million 'hops' of a molecule, where each pixel is a potential binding site. The starting position of the molecule is the left hand edge of the simulation. A) Simulation temperature is 290K. An unfavourable site for surface diffusion, blocking the diffusion path, is highlighted via a red circle. A favourable diffusion site, leading to trapped molecules, is highlighted via a black circle. B) Simulation temperature is 180K. C) Simulation temperature is 70K.

In Fig. 7.8A it is noted that the vast majority of hops are around the eight corner sites; other areas of high occupancy are the molecular edges of the chambers. This is expected due to the larger energy well generated by adjacent molecules. Henceforth, diffusion is predominantly along the edges, as generated by the bound molecular walls. A peak in occupancy under the tip location indicates that the diffusing molecule is becoming trapped under the tip due to the potential well. Finally, it is apparent that in this simulation configuration the presence of the central barrier significantly impedes molecular motion from one side of the simulation to the other. This arises from energetically unfavourable sites at the corners of the barrier molecules, as marked on the Figure 7.8A. Here, molecules diffusing along boundaries move from having two molecular neighbours to only one. This is an energetically unfavourable event, which is clearly apparent by closer examination of local hopping rates surrounding the gate. Across the temperature range in Figure 7.8, it is apparent that lower temperatures lead to a lower probability of the molecule diffusing away from the simulation

edge.

From these results, two alternative models for the surface molecular geometry are suggested, as shown in Figure 7.9. These geometries ensure that a molecule diffusing along the simulation boundaries will encounter fewer obstacles to crossing from one chamber to the next. In the first geometry, Figure 7.9A, while traversing the gate, a diffusing molecule will always have two neighbours. The second geometry, Figure 7.9B, mirrors the first in its gate location, but rounds off the corners of the simulation to reduce the trapping energy well.

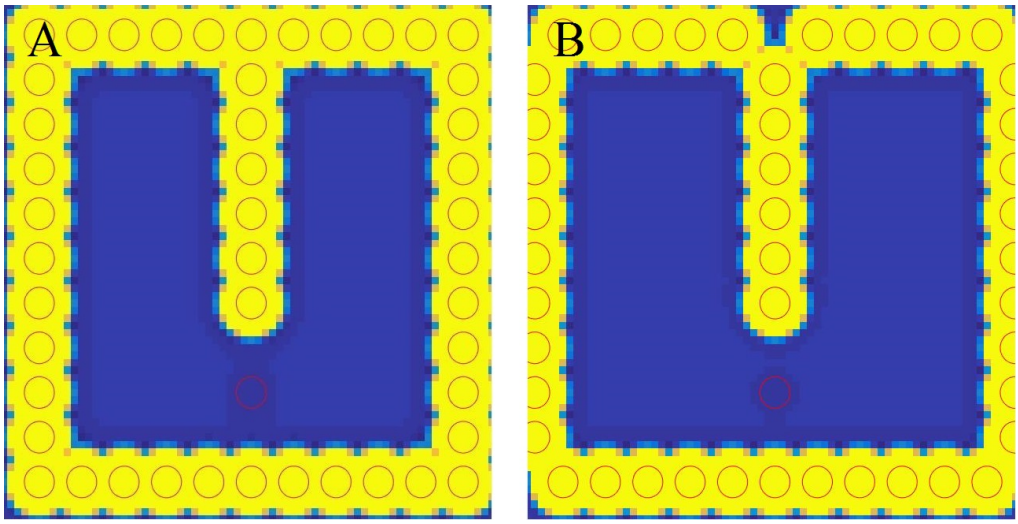

Figure 7.9: Logarithmic heatmaps of the energy landscape, as generated by two alternate surface barrier configurations. A) Gate moved to edge of chamber. B) Corners of chambers rounded by moving walls two binding sites outwards. Additionally, a molecule is removed from where the barrier meets the chamber to reduce the local energy well.

Two quantitative parameters require calculation. Firstly, the time for a molecule to diffuse from one chamber to the other, and secondly, the time for a molecule to diffuse across the gate between the chambers - under the tip. The first of these is important as this event must happen a large number of times within the duration of a physical experiment. It is primarily a function of the simulation temperature, and the number of molecules in the simulation. The second is important as the diffusion time must be low enough that the molecule can be accurately tracked. It is primarily a

function of the temperature and the tip position.

Simulation time was tracked to measure the time taken for a molecule to diffuse from one half of the simulation to the other. This was completed for both simulation geometries previously mentioned. The results in Figure 7.10 show that a diffusing molecule will pass significantly faster across the simulation boundary with an edge-gate chamber configuration, and even faster with the addition of the rounded corners reducing local trapping.

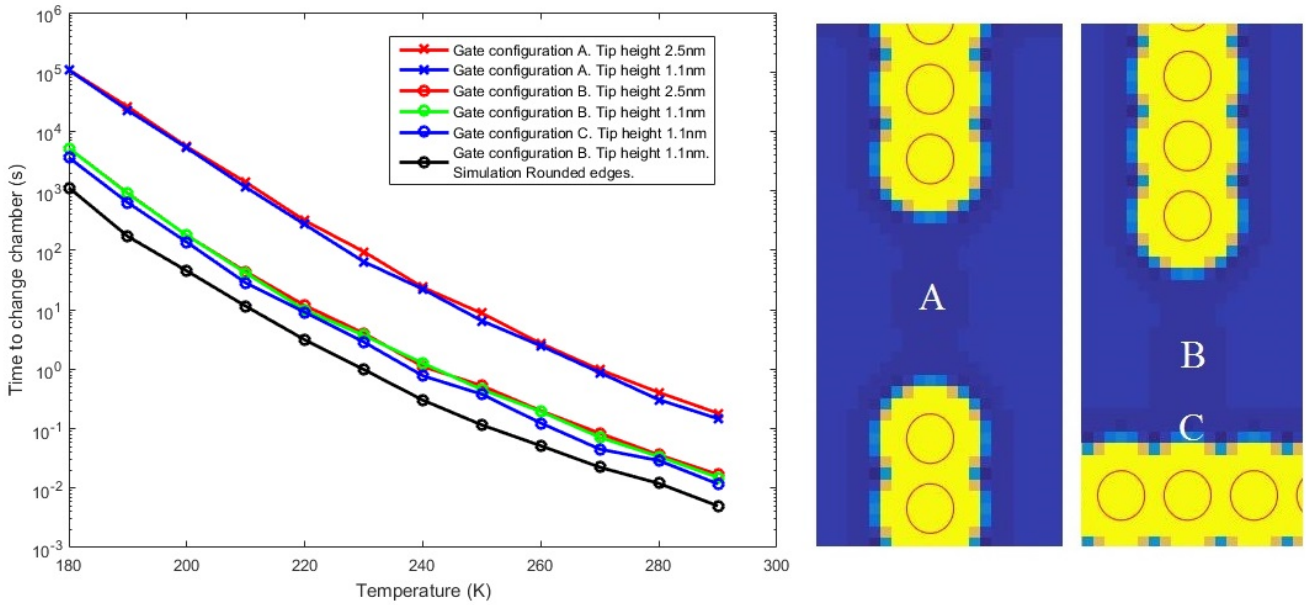

Figure 7.10: The time for a molecule to pass from one chamber to another is measured as a function of temperature, for a number of different simulation configurations. Each data point is calculated by initialising a molecule on the left hand edge of the simulation, and tracking the time taken to pass through the gate, to the opposite side of the simulation. Each data point is an average value of 250 such experiments. The time is calculated via the process described in section 3.2.2. The position of the SPM tip and associated chamber configuration is indicated in the legend and marked on the corresponding graphic of the gate configuration. Tip position A is over a gate positioned centrally between the two chambers. Tip positions B and C are over a gate positioned to the edge of two chambers.

From Figure 7.10 it is very clear that the edge-gate geometry is significantly superior at allowing molecules to pass from one chamber to the next, for all temperatures. The impact of the tip height and positioning also impacted the transfer time, but to a lesser extent. Interestingly, for the centre-gate geometry, it was noted that a tip closer to the surface actually

led to a faster crossing time. These were reduced by an average of 19%. This is despite the fact that a lower tip will induce an energy well that could trap a molecule under the tip. It is thought that as the tip adds a potential well next to the unfavourable region marked in Figure 7.8A, this would ease the journey of the diffusing molecule around the energetically unfavourable border region to the gate. The effect is also seen in the edge-gate geometry, but to a lesser extent (6% rise) due to the relative ease of molecular motion across the gate. From these data, we can estimate a lower bound in the temperature that would allow a Maxwell's demon experiment to take place. For a chamber configuration with an edge-gate, and rounded edges, this is 200K. At this temperature, a molecule should cross the gate at once every 45 seconds, depending on the tip position. With an increased number of diffusing molecules, this rate should be increased as a function of the number of diffusing molecules.

Further calculations were focused on the edge-gate molecular geometry, due to its superior qualities at allowing inter-chamber diffusion. The time for a molecule to diffuse across the gate directly is shown in Figure 7.11, for a number of different tip configurations. It is noted that the lateral, as well as vertical, position of the tip can have a large impact on the time to cross the gate. Here slower crossing times are favourable to ensure the tip can detect the diffusing molecule. For a tip position B, and 1.1nm from the surface, a temperature below 240K leads to a diffusion time within the bandwidth of the SPM monitoring. For tip position A, a corresponding temperature of 190K is necessary. The large difference between these temperatures demonstrates the importance of the positioning of the tip to control the diffusion speed under it. This is also illustrated in Figure 7.12 where the molecular occupancy is tracked for different tip positions.

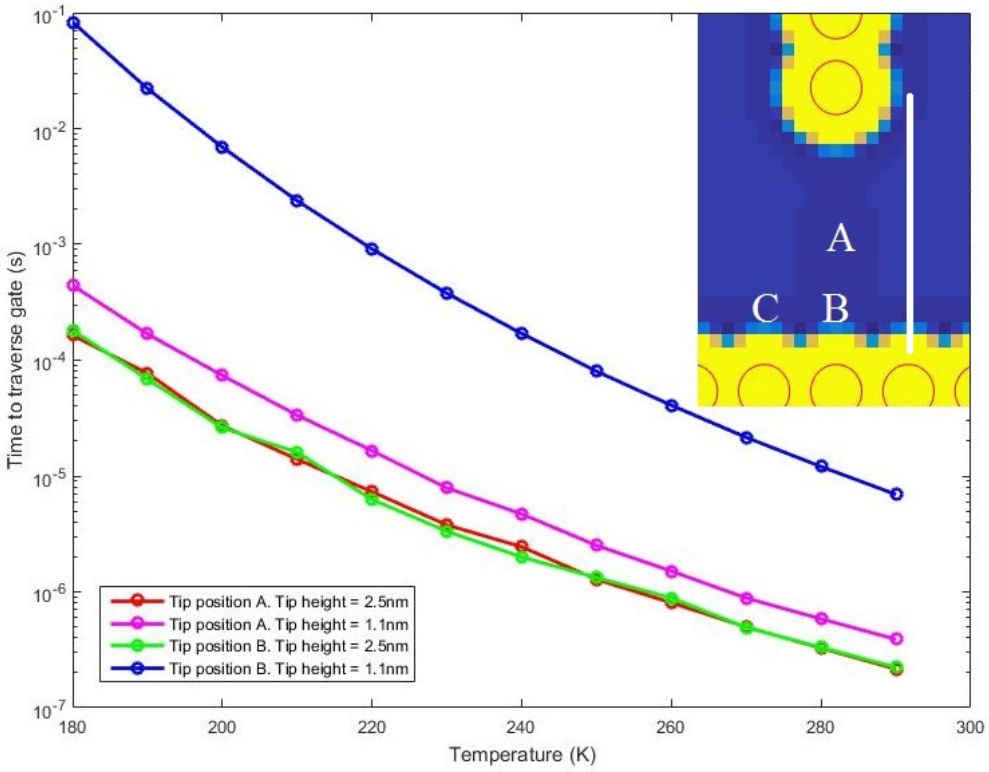

Figure 7.11: The time for a molecule to diffuse across the gate, under the presence of a C_{60}-terminated tip molecule. Here the gate is at the edge of two chambers. A molecule to be simulated is placed adjacent to the gap, at the location marked C, and blocked from diffusing backwards into its current chamber. The time is measured when it crosses into the adjacent chamber by crossing the vertical white line, a lateral distance of six binding sites. Each datapoint is an average of 50,000 such simulations. It is clear that tip position as well as tip height plays a critical role in determining the rate of diffusion across the gate. A tip at position B, and approached close to the surface contributes to a deep potential well which slows the molecular crossing.

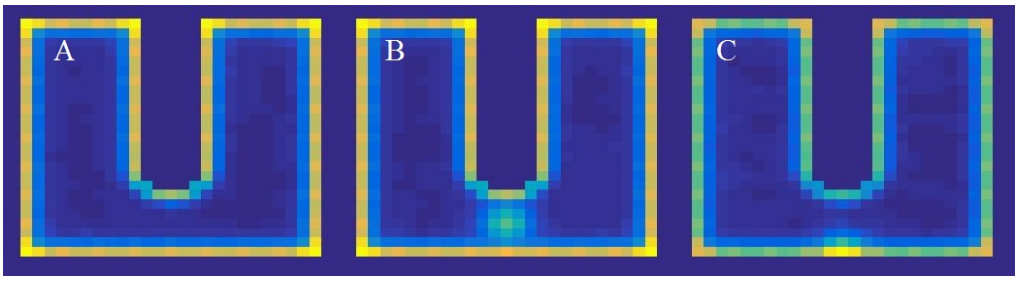

Figure 7.12: A heatmap of molecular occupancy for three different tip positions. Each image is comprised of 480 million molecular diffusion events. A-B Corresponds to tip position A, in Figure 7.11, with a tip-surface separation of 2.5nm and 1.1nm respectively. C corresponds to tip position B in Figure 7.11, with a tip height of 1.1nm.

7.3 Conclusions

A simulation was written to examine the feasibility of a Maxwell's Demon experiment, as mediated via an SPM probe. Chamber geometry was seen to be a critical factor in the time taken for a molecule to diffuse between chambers, and as such, a number of possible chamber geometries were suggested. Tip position within the gate was additionally investigated and found that it could have a measurable affect on the passage time of molecules through the gate.

A temperature range of 200K to 240K, with a chamber geometry similar to that in Figure 7.9 B, should have diffusion events from one chamber to the other every 45 seconds per diffusing molecule, though this will be dependent on tip position. At these temperatures, with a tip in position B in Figure 7.11, a molecule will take 6.9×10^{-3} to 1.7×10^{-4} seconds to cross the barrier. These times lie within the detection bandwidth of the atom tracking system and as such, should be able to be tracked accurately. Future experimental work might consider this temperature range and associated chamber geometry as candidates for a Maxwell's Demon experiment.

Chapter 8

Conclusions

In this thesis, a number of experimental and theoretical endeavours were described, which broadly investigated the physics and kinetics of C_{60} molecules on metal surfaces. This was done via a wide range of methods including experimental techniques such as AFM and STM, as well as theoretical techniques, such as Hückel theory and Monte Carlo simulations.

Two Monte Carlo simulations were written to investigate different aspects of molecular kinetics on surfaces, though they were both radically different in the system they were investigating. The first is a major and novel simulation into the orientational ordering of C_{60} monolayers and multilayers, with the inclusion of a surface interaction. A key feature of this model is that it can simulate assemblies of hundreds, or even thousands, of molecules. This was achieved by pre-calculating repulsive intermolecular interactions using Hückel theory. These could then be quickly applied to many different molecular configuration. Complex monolayer and multilayer long-range rotational configurations, observed via STM on a variety of substrates, were successfully modelled. This not only included steady state order but also fluctuating defects and transient states. Bulk molecular configurations were investigated. Here the relationship between temperature, intermolecular spacing, and the resultant order was investigated. A critical

point where the assembly would transition from order to disorder was seen, similar to XRD data. Finally, the effects of vacancies was probed. Vacancies in monolayers were seen to lead to an early onset of disorder. Further study could examine further the relationship between shaped islands and resultant order.

A second Monte Carlo simulation was written to study the kinetics of a diffusing C_{60} on a hydrogen passivated silicon surface. This was used to estimate the feasibility of a future SPM recreation of the famous Maxwell's Demon thought experiment. A Girifalco potential was applied from a number of static molecules to a sinusoidal surface potential. A Monte Carlo simulation was applied to this surface potential, to fully explore the dynamics of the system. As a result, a number of optimal chamber configurations were suggested from outcomes observed in simulation, as well as a number of possible temperature ranges at which this experiment might be possible. Future simulation work could investigate multiple diffusing molecules to study possible molecular clogging of the gate.

Finally, a series of experimental results were compiled demonstrating the use of AFM and STM to study K doped C_{60}. Two molecular configurations were studied, a single molecule doped progressively by dragging it over successive K atoms, and K doped molecular islands. In the single molecule case, changes in differential conductance measurements were observed indicating molecular charging. These measurements additionally indicated a reduction in LUMO splitting caused by K doping reducing the molecule-surface interaction. AFM measurements indicated a strong charge-charge interaction between the tip and molecule. In K doped monolayers molecular orientation was ascertained by AFM, and mobile surface dopants were seen to influence local changes in differential conductance. Further study could further investigate the impact of mobile surface dopants on charging.

Lock-in techniques could additionally be utilised to further analyse the impact of these dopants on molecular orbitals. These allow imaging while simultaneously collecting differential conductance measurements. As such, local and non-local modification of the electronic structure of the island by dopants could be further analysed.

Bibliography

[1] G. Binnig and H. Rohrer, "Scanning tunneling microscopy," *Surface science*, vol. 126, no. 1-3, pp. 236–244, 1983.

[2] L. Gross, "Recent advances in submolecular resolution with scanning probe microscopy," *Nat. Chem.*, vol. 3, pp. 273–278, 2011.

[3] A. Sweetman, S. Jarvis, H. Sang, I. Lekkas, P. Rahe, Y. Wang, J. Wang, N. Champness, L. Kantorovich, and P. Moriarty, "Mapping the force field of a hydrogen-bonded assembly," *Nature communications*, vol. 5, p. 3931, 2014.

[4] R. Yamachika, M. Grobis, A. Wachowiak, and M. Crommie, "Controlled atomic doping of a single c60 molecule," *Science*, vol. 304, no. 5668, pp. 281–284, 2004.

[5] N. Pavliček and L. Gross, "Generation, manipulation and characterization of molecules by atomic force microscopy," *Nature Reviews Chemistry*, vol. 1, p. 0005, 2017.

[6] K. Capelle, "A bird's-eye view of density-functional theory," *Brazilian Journal of Physics*, vol. 36, no. 4A, pp. 1318–1343, 2006.

[7] K. Binder, "Applications of monte carlo methods to statistical physics," *Reports on Progress in Physics*, vol. 60, no. 5, p. 487, 1997.

[8] M. Karplus and J. A. McCammon, "Molecular dynamics simulations of biomolecules," *Nature Structural & Molecular Biology*, vol. 9, no. 9, pp. 646–652, 2002.

[9] K. Yates, *Hückel molecular orbital theory*. Elsevier, 2012.

[10] H. W. Kroto, J. R. Heath, S. C. O'Brien, R. F. Curl, and R. E. Smalley, "c_{60}: buckminsterfullerene," *Nature*, vol. 318, no. 6042, pp. 162–163, 1985.

[11] M. Koleini and M. Brandbyge, "Strong spin-filtering and spin-valve effects in a molecular v–c_{60}–v contact," *Beil. J. Nanotech.*, vol. 3, no. 1, pp. 589–596, 2012.

[12] S. I. Bozhko, S. A. Krasnikov, O. Lübben, B. E. Murphy, K. Radican, V. N. Semenov, H.-C. Wu, E. A. Levchenko, A. N. Chaika, N. N. Sergeeva, *et al.*, "Correlation between charge-transfer and rotation of c_{60} on wo 2/w (110)," *Nanoscale*, vol. 5, no. 8, pp. 3380–3386, 2013.

[13] P. Moriarty, Y. Ma, M. Upward, and P. Beton, "Translation, rotation and removal of c_{60} on si (100)-2$\times$ 1 using anisotropic molecular manipulation," *Surf. Sci.*, vol. 407, no. 1, pp. 27–35, 1998.

[14] S. Lounis, "Theory of scanning tunneling microscopy," *arXiv preprint arXiv:1404.0961*, 2014.

[15] J. Tersoff and D. Hamann, "Theory of the scanning tunneling microscope," in *Scanning Tunneling Microscopy*, pp. 59–67, Springer, 1993.

[16] H. Ou-Yang, B. Källebring, and R. Marcus, "A theoretical model of scanning tunneling microscopy: Application to the graphite (0001) and au (111) surfaces," *J. Chem. Phys.*, vol. 98, no. 9, pp. 7565–7573, 1993.

[17] A. Verma, O. Uzun, Y. Hu, Y. Hu, H.-S. Han, N. Watson, S. Chen, D. J. Irvine, and F. Stellacci, "Surface-structure-regulated cell-membrane penetration by monolayer-protected nanoparticles," *Nat. Mat.*, vol. 7, no. 7, pp. 588–595, 2008.

[18] F. J. Giessibl, "Advances in atomic force microscopy," *Revs. Mod. Phys.*, vol. 75, no. 3, p. 949, 2003.

[19] F. J. Giessibl, "Forces and frequency shifts in atomic-resolution dynamic-force microscopy," *Physical Review B*, vol. 56, no. 24, p. 16010, 1997.

[20] J. E. Sader and S. P. Jarvis, "Accurate formulas for interaction force and energy in frequency modulation force spectroscopy," *Applied Physics Letters*, vol. 84, no. 10, pp. 1801–1803, 2004.

[21] E. Hückel, "Quantentheoretische beiträge zum benzolproblem," *Zeitschrift für Physik A Hadrons and Nuclei*, vol. 70, no. 3, pp. 204–286, 1931.

[22] E. Clementi and D.-L. Raimondi, "Atomic screening constants from scf functions," *J. Chem. Phys.*, vol. 38, no. 11, pp. 2686–2689, 1963.

[23] I. D. Hands, J. L. Dunn, and C. A. Bates, "Calculation of images of oriented c_{60} molecules using molecular orbital theory," *Phys. Rev. B*, vol. 81, p. 205440, May 2010.

[24] A. J. Lakin, C. Chiutu, A. M. Sweetman, P. Moriarty, and J. L. Dunn, "Recovering molecular orientation from convoluted orbitals," *Phys. Rev. B*, vol. 88, no. 3, p. 035447, 2013.

[25] C. Chiutu, A. Sweetman, A. Lakin, A. Stannard, S. Jarvis, L. Kantorovich, J. Dunn, and P. Moriarty, "Precise orientation of a single c_{60} molecule on the tip of a scanning probe microscope," *Phys. Rev. Lett.*, vol. 108, no. 26, p. 268302, 2012.

[26] R. Hoffmann, "An extended hückel theory. i. hydrocarbons," *The Journal of Chemical Physics*, vol. 39, no. 6, pp. 1397–1412, 1963.

[27] P. Murray, M. Pedersen, E. Lægsgaard, I. Stensgaard, and F. Besenbacher, "Growth of c_{60} on cu (110) and ni (110) surfaces: c_{60}-induced interfacial roughening," *Phys. Rev. B*, vol. 55, no. 15, pp. 9360–9363, 1997.

[28] W. David, R. Ibberson, T. Dennis, J. Hare, and K. Prassides, "Structural phase transitions in the fullerene c_{60}," *Europhys. Lett.*, vol. 18, no. 3, pp. 219–225, 1992.

[29] F. Rossel, M. Pivetta, F. Patthey, E. Ćavar, A. P. Seitsonen, and W.-D. Schneider, "Growth and characterization of fullerene nanocrystals on nacl/au (111)," *Phys. Rev. B*, vol. 84, no. 7, p. 075426, 2011.

[30] G. Schull and R. Berndt, "Orientationally ordered (7× 7) superstructure of c_{60} on au (111)," *Phys. Rev. Lett.*, vol. 99, no. 22, p. 226105, 2007.

[31] C. Liu, Z. Qin, J. Chen, Q. Guo, Y. Yu, and G. Cao, "Molecular orientations and interfacial structure of c_{60} on pt (111)," *J. Chem. Phys.*, vol. 134, no. 4, p. 044707, 2011.

[32] T. Hashizume, K. Motai, X. Wang, H. Shinohara, Y. Saito, Y. Maruyama, K. Ohno, Y. Kawazoe, Y. Nishina, and Pickering, "Intramolecular structures of c_{60} molecules adsorbed on the cu (111)-(1× 1) surface," *Phys. Rev. Lett.*, vol. 71, no. 18, pp. 2959–2962, 1993.

[33] S. Bozhko, V. Taupin, M. Lebyodkin, C. Fressengeas, E. Levchenko, K. Radikan, O. Lübben, V. Semenov, and I. Shvets, "Disclinations in c_{60} molecular layers on wo 2/w (110) surfaces," *Phys. Rev. B*, vol. 90, no. 21, p. 214106, 2014.

[34] M. Paßens, R. Waser, and S. Karthäuser, "Enhanced fullerene–au (111) coupling in $(2\sqrt{3} \times 2\sqrt{3})r30°$ superstructures with intermolecular interactions," *Beilstein J. Nanotechnol.*, vol. 6, no. 1, pp. 1421–1431, 2015.

[35] L.-F. Yuan, J. Yang, H. Wang, C. Zeng, Q. Li, B. Wang, J. Hou, Q. Zhu, and D. Chen, "Low-temperature orientationally ordered structures of two-dimensional c_{60}," *J. Am. Chem. Soc.*, vol. 125, no. 1, pp. 169–172, 2003.

[36] M. Paßens and S. Karthäuser, "Interfacial and intermolecular interactions determining the rotational orientation of c_{60} adsorbed on au (111)," *Surf. Sci.*, vol. 642, pp. 11–15, 2015.

[37] J. Hou, J. Yang, H. Wang, Q. Li, C. Zeng, H. Lin, W. Bing, D. Chen, and Q. Zhu, "Identifying molecular orientation of individual c_{60} on a si (111)-(7× 7) surface," *Phys. Rev. Lett.*, vol. 83, no. 15, pp. 3001–3004, 1999.

[38] H. Wang, C. Zeng, B. Wang, J. Hou, Q. Li, and J. Yang, "Orientational configurations of the c_{60} molecules in the (2× 2) superlattice on a solid c_{60} (111) surface at low temperature," *Phys. Rev. B*, vol. 63, no. 8, p. 085417, 2001.

[39] P. A. Heiney, J. E. Fischer, A. R. McGhie, W. J. Romanow, A. M. Denenstein, J. P. McCauley Jr, A. B. Smith, and D. E. Cox, "Orientational ordering transition in solid c_{60}," *Phys. Rev. Lett.*, vol. 66, no. 22, pp. 2911–2914, 1991.

[40] J. A. Larsson, S. D. Elliott, J. C. Greer, J. Repp, G. Meyer, and R. Allenspach, "Orientation of individual c_{60} molecules adsorbed on cu (111): low-temperature scanning tunneling microscopy and density functional calculations," *Phys. Rev. B*, vol. 77, no. 11, p. 115434, 2008.

[41] M. Casarin, D. Forrer, T. Orzali, M. Petukhov, M. Sambi, E. Tondello, and A. Vittadini, "Strong bonding of single c_{60} molecules to (1× 2)-pt (110): an stm/dft investigation," *J. Phys. Chem. C*, vol. 111, no. 26, pp. 9365–9373, 2007.

[42] S. A. Krasnikov, S. I. Bozhko, K. Radican, O. Lübben, B. E. Murphy, S.-R. Vadapoo, H.-C. Wu, M. Abid, V. N. Semenov, and I. V. Shvets, "Self-assembly and ordering of c_{60} on the wo2/w (110) surface," *Nano. Res.*, vol. 4, no. 2, pp. 194–203, 2011.

[43] L.-L. Wang and H.-P. Cheng, "Density functional study of the adsorption of a c_{60} monolayer on ag (111) and au (111) surfaces," *Phys. Rev. B*, vol. 69, no. 16, p. 165417, 2004.

[44] C. Laforge, D. Passerone, A. Harris, P. Lambin, and E. Tosatti, "Two-stage rotational disordering of a molecular crystal surface: c_{60}," *Phys. Rev. Lett.*, vol. 87, no. 8, p. 085503, 2001.

[45] L. Tang, Y. Xie, and Q. Guo, "Complex orientational ordering of c_{60} molecules on au (111)," *J. Chem. Phys.*, vol. 135, no. 11, p. 114702, 2011.

[46] D. Lamoen and K. Michel, "Crystal field, orientational order, and lattice contraction in solid c_{60}," *J. Chem. Phys.*, vol. 101, no. 2, pp. 1435–1443, 1994.

[47] A. K. Rappé, C. J. Casewit, K. Colwell, W. Goddard Iii, and W. Skiff, "Uff, a full periodic table force field for molecular mechanics and molecular dynamics simulations," *Journal of the American chemical society*, vol. 114, no. 25, pp. 10024–10035, 1992.

[48] M. Cañas-Ventura, W. Xiao, P. Ruffieux, R. Rieger, K. Müllen, H. Brune, and R. Fasel, "Stabilization of bimolecular islands on ul-

trathin nacl films by a vicinal substrate," *Surf. Sci.*, vol. 603, no. 15, pp. 2294–2299, 2009.

[49] O. Pfeiffer, E. Gnecco, L. Zimmerli, S. Maier, E. Meyer, L. Nony, R. Bennewitz, F. Diederich, H. Fang, and D. Bonifazi, "Force microscopy on insulators: imaging of organic molecules," *J. Phys.: Conf. Ser.*, vol. 19, no. 1, pp. 166–174, 2005.

[50] A. Goldoni, C. Cepek, and S. Modesti, "First-order orientational-disordering transition on the (111) surface of c_{60}," *Phys. Rev. B*, vol. 54, pp. 2890–2895, Jul 1996.

[51] E. Katz, D. Faiman, B. Mishori, Y. Shapira, A. Isakina, and M. Strzhemechny, "Disorder/order phase transition in c60 thin films studied by surface photovoltage spectroscopy," *Journal of applied physics*, vol. 94, no. 11, pp. 7173–7177, 2003.

[52] J. Leaf, A. Stannard, S. P. Jarvis, P. Moriarty, and J. L. Dunn, "A combined monte carlo and hu?ckel theory simulation of orientational ordering in c60 assemblies," *The Journal of Physical Chemistry C*, vol. 120, no. 15, pp. 8139–8147, 2016.

[53] A. Maxwell, P. Brühwiler, S. Andersson, N. Mårtensson, and P. Rudolf, "Electronic structure study of kxc60 compounds with x> 6," *Chemical physics letters*, vol. 247, no. 3, pp. 257–263, 1995.

[54] A. Hebard, M. Rosseinky, R. Haddon, D. Murphy, S. Glarum, T. Palstra, A. Ramirez, and A. Karton, "Potassium-doped c60," *Nature*, vol. 350, pp. 600–601, 1991.

[55] J. Winter and H. Kuzmany, "Potassium-doped fullerene kχc60 with x= 0, 1, 2, 3, 4, and 6," *Solid state communications*, vol. 84, no. 10, pp. 935–938, 1992.

[56] T. Palstra, O. Zhou, Y. Iwasa, P. Sulewski, R. Fleming, and B. Zegarski, "Superconductivity at 40k in cesium doped c60," *Solid state communications*, vol. 93, no. 4, pp. 327–330, 1995.

[57] K.-A. Wang, Y. Wang, P. Zhou, J. M. Holden, S.-l. Ren, G. T. Hager, H. F. Ni, P. C. Eklund, G. Dresselhaus, and M. S. Dresselhaus, "Raman scattering in c_{60} and alkali-metal-doped c_{60} films," *Phys. Rev. B*, vol. 45, pp. 1955–1958, Jan 1992.

[58] L. Degiorgi, "The alkali-metal doped c 60 : what can we learn from the optical properties," *Physica Scripta*, vol. 1996, no. T66, p. 272, 1996.

[59] L. Tjeng, R. Hesper, A. Heessels, A. Heeres, H. Jonkman, and G. Sawatzky, "Development of the electronic structure in a k-doped c60 monolayer on a ag (1 1 1) surface," *Solid state communications*, vol. 103, no. 1, pp. 31–35, 1997.

[60] P. Brühwiler, A. Maxwell, A. Nilsson, N. Mårtensson, and O. Gunnarsson, "Auger and photoelectron study of the hubbard u in c 60, k 3 c 60, and k 6 c 60," *Physical Review B*, vol. 48, no. 24, p. 18296, 1993.

[61] W. Yang, V. Brouet, X. Zhou, H. J. Choi, S. G. Louie, M. L. Cohen, S. Kellar, P. Bogdanov, A. Lanzara, A. Goldoni, *et al.*, "Band structure and fermi surface of electron-doped c60 monolayers," *Science*, vol. 300, no. 5617, pp. 303–307, 2003.

[62] A. Wachowiak, R. Yamachika, K. Khoo, Y. Wang, M. Grobis, D.-H. Lee, S. G. Louie, and M. Crommie, "Visualization of the molecular jahn-teller effect in an insulating k4c60 monolayer," *Science*, vol. 310, no. 5747, pp. 468–470, 2005.

[63] Y. Wang, R. Yamachika, A. Wachowiak, M. Grobis, K. Khoo, D.-H. Lee, S. G. Louie, and M. Crommie, "Novel orientational ordering and

reentrant metallicity in kxc60 monolayers for $3 \leq x \leq 5$," *Physical review letters*, vol. 99, no. 8, p. 086402, 2007.

[64] Y. Wang, R. Yamachika, A. Wachowiak, M. Grobis, and M. F. Crommie, "Tuning fulleride electronic structure and molecular ordering via variable layer index," *Nature materials*, vol. 7, no. 3, pp. 194–197, 2008.

[65] M. De Menech, U. Saalmann, and M. E. Garcia, "Energy-resolved stm mapping of c 60 on metal surfaces: A theoretical study," *Physical Review B*, vol. 73, no. 15, p. 155407, 2006.

[66] J. Maxwell, "Theory of heat,(green & co., longmans, london)," 1871.

[67] L. Girifalco, M. Hodak, and R. S. Lee, "Carbon nanotubes, buckyballs, ropes, and a universal graphitic potential," *Physical Review B*, vol. 62, no. 19, p. 13104, 2000.

[68] J. A. Stroscio and D. Eigler, "Atomic and molecular manipulation with the scanning tunneling microscope," *Science*, vol. 254, no. 5036, p. 1319, 1991.

[69] E. Riedo, E. Gnecco, R. Bennewitz, E. Meyer, and H. Brune, "Interaction potential and hopping dynamics governing sliding friction," *Physical review letters*, vol. 91, no. 8, p. 084502, 2003.

'One of the great things about books is sometimes there are some fantastic pictures.'

- George W. Bush

List of Figures